Calibration, Background Study, and Search for New Physics with the GERDA Experiment

Dissertation
zur
Erlangung der naturwissenschaftlichen Doktorwürde
(Dr. sc. nat.)

vorgelegt der
Mathematisch-naturwissenschaftlichen Fakultät
der Universität Zürich

von
Rizalina Mingazheva
aus Russland

Promotionskomission
Prof. Dr. Laura Baudis (Vorsitz)
Prof. Dr. Florencia Canelli
Dr. Roman Hiller

Zürich, 2019

Abstract

The search for the neutrinoless double beta ($0\nu\beta\beta$) decay is a promising channel for revealing the neutrino nature and explaining the matter-antimatter asymmetry in the Universe. This decay has not been observed yet, and the strongest constraints limit the value of its half-life beyond 10^{26} yr. The GERDA experiment searches for this rare decay deploying 36 kg of enriched germanium detectors. The current phase of data collection was launched in December 2015, and the experiment has already surpassed the goal sensitivity of 10^{26} yr and set the strongest limit on the $0\nu\beta\beta$ decay half-life of ^{76}Ge in the field as $T_{1/2} > 0.9 \cdot 10^{26}$ yr (90% C.L.) .

The main focus of this thesis is the energy scale calibration of the germanium detectors, study of the gamma background, and search for keV-scale dark matter with GERDA.

In this work, the calibration of germanium detectors from the first two years of the data-taking was performed. From exposing the detectors to the ^{228}Th gamma sources, the energy scale of each detector was defined, enabling to combine the data from different detectors over extended periods consistently. The energy calibration was additionally used as an effective tool to monitor the energy scale stability of the detectors throughout the data taking and to select the data for the $0\nu\beta\beta$ decay search. From the analysis of the combined calibration data, the energy resolution for the physics data analysis was determined, in particular, for the $0\nu\beta\beta$ decay search.

To understand the background in GERDA and, importantly, to model it for the $0\nu\beta\beta$, a complex global model for the full energy spectrum is constructed, simulating the different background sources. The gamma lines in the spectrum are particularly informative for quantifying and locating the background sources. In this dissertation, the intensities of the gamma background lines were estimated, evaluating the contribution of the primordial, cosmogenic, and anthropogenic sources to the physics data. The results served as the cross-check for the background model predictions.

With its superior energy resolution and background knowledge, GERDA is capable of exploring other exotic physics channels, besides the $0\nu\beta\beta$ decay search. A search for the peaks in the energy spectrum incompatible with the background model was performed. Focusing on a particular energy range, the results of this analysis were used to search for bosonic Super-WIMPs, which are dark matter candidates with masses in the keV-scale. This study was the first in the field to explore the mass range beyond 120 keV.

The thesis is organized as follows. Chapter 1 provides a brief introduction to the $0\nu\beta\beta$ decay, the current status of the field, possible limitations, and requirements for the experimental search. Chapter 2 introduces the GERDA experiment with a detailed description of the detector setup, analysis procedure, and the latest results. Chapter 3 describes the analysis of calibration

data collected in the first two years of data taking and determination of the energy resolution for the $0\nu\beta\beta$ decay. Chapter 4 presents detailed results on the gamma background study and a comparison with the background model. In Chapter 5, a search for unknown peak signals in GERDA is performed and applied to search for bosonic Super-WIMPs. The results of the analyses are summarized in the Conclusion. In the appendix, an additional discussion of the technical details is provided.

Contents

Chapter 1

Neutrinos and Neutrinoless Double Beta Decay

1.1 A Brief History Of Neutrinos

The neutrino history began with the observation which appeared to violate the energy and angular momentum conservation laws in the measurement of the beta decay energy spectrum by Lise Meitner and Otto Hahn in 1911 [1]. To explain this mystery, a new particle was postulated in W. Pauli's famous letter to the "radioactive society" [2]. According to Pauli's proposal, to fit the observations, the new particle should be light, neutral, and weakly interacting to share the released energy of the electron emitted in the decay. W. Pauli later stated, "I have done a terrible thing, I have postulated a particle that cannot be detected."

It took almost 26 years to detect the new mysterious particle. First observations of neutrinos were made in the pioneering reactor antineutrino experiment conducted by Reines and Cowan [3] based on the inverse beta decay process:

$$\bar{\nu}_e + p \longrightarrow n + e^+.$$

The released positron e^+ annihilated with an e^- from the surrounding atoms, emitting two γ rays. After several microsecond of diffusion, the neutron is then was absorbed by the ^{109}Cd added to the water, and the few γ rays were emitted as a result of the following chain reactions:

$$n + {}^{108}\mathrm{Cd} \longrightarrow {}^{109}\mathrm{Cd}_{*} \longrightarrow {}^{109}\mathrm{Cd} + \gamma.$$

From each of the reaction, the γ rays were detected coincidentally by two liquid scintillator layers surrounding the water tank. Thus, the antineutrino interaction was confirmed by the observation of the two prompt coincidences separated by several microseconds. The results of the Cowan and Reines experiment proved the existence of neutrinos [4].

Soon after, in 1962 it was discovered that the neutrino produced in the decay of π-mesons via the reaction:

$$\pi^{\pm} \longrightarrow \mu^{\pm} + \nu_{\mu}(\bar{\nu}_{\mu})$$

was different from that emitted in the beta decay [5]. Neutrinos emitted in the π-meson decay were named muon neutrinos since the decay was accompanied by a muon. In 2000, a third neutrino type, tau neutrino (ν_τ), was discovered by the experiment DONUT [6].

Before the tau neutrino was detected, R. Davis made another important discovery. In 1962, he started an experiment to detect solar neutrinos using ^{37}Cl as a target element following the reaction proposed by Pontecorvo [7]:

$$\nu_e +^{37} Cl \longrightarrow e^- +^{37} Ar.$$

Eleven years after the experiment was launched, the first results started to appear [8]. Twenty years later, the experiment found that the flux of detected solar neutrinos was three times less than predicted. This result shook the neutrino society for the second time, giving rise to what was called the "solar neutrino problem".

Fortunately, the solution to the problem had been already proposed shortly before Davis's experiment began. In 1957 B. Pontecorvo predicted the quantum-mechanical phenomena of neutrino oscillation [9]. The process implies that the neutrino of one lepton flavor (electron, muon, or tau) would change its flavor after some distance travelled. Thus, by the time a relativistic electron neutrino, produced in the core of the Sun, reaches the Earth's surface, it would have another flavor, becoming either a muon or tau neutrino with the following probability [10]:

$$\begin{aligned} P_{\alpha\rightarrow\beta} = {} & \delta_{\alpha\beta} + \\ & -4\sum_{i>j} \Re(U^*_{\alpha i}U_{\beta i}U_{\alpha j}U^*_{\beta j}) sin^2 \left[1,27\Delta m^2_{ij}(L/E)\right] + \\ & +2\sum_{i>j} \Im(U^*_{\alpha i}U_{\beta i}U_{\alpha j}U^*_{\beta j}) sin^2 \left[2,54\Delta m^2_{ij}(L/E)\right], \end{aligned} \tag{1.1}$$

where α and β denote initial and final neutrino's lepton flavor, L is the travelled distance, E is the energy of neutrino, $\Delta m^2_{ij} = m^2_i - m^2_j$ is the squared mass difference of neutrino mass eigenvalues, $\delta_{\alpha\beta}$ is Kronecker delta, defined as:

$$\delta_{\alpha\beta} = \begin{cases} 0, & \text{if } \alpha \neq \beta \\ 1, & \text{if } \alpha = \beta \end{cases} . \tag{1.2}$$

The elements $U_{\alpha(\beta)i(j)}$ are the elements of the Pontecorvo-Maki-Nakagawa-Sakata matrix (PMNS matrix), 3×3 unitary matrix introduced to describe the mixing of the neutrino lepton flavor as:

$$\nu_\alpha = \sum_{i=1}^{3} U_{\alpha i}\nu_i \quad (\alpha = e, \mu, \tau), \tag{1.3}$$

where index i runs over the neutrino mass eigenstates. A more detailed discussion regarding the PMNS matrix and neutrino mass eigenstates follows in Section 1.3.1.

As Eq. (1.1) illustrates, probability of neutrino oscillation takes non-zero value, only if neutrinos have non-zero mass, that was not predicted by the Standard Model (SM). The problem of neutrino oscillation was explored widely by a vast body of experiments studying neutrinos from the Sun, the atmosphere, and produced in nuclear reactors and accelerators, confirming the

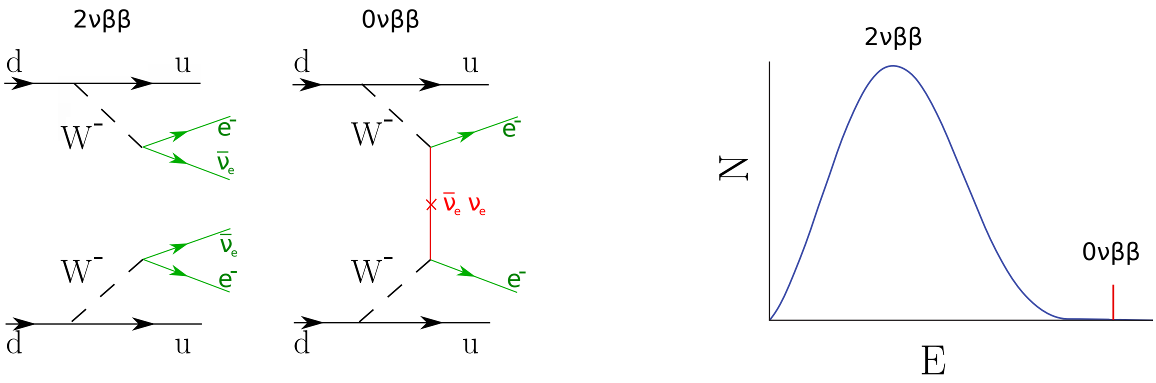

Figure 1.1: Left: Feynman diagrams corresponding to $2\nu\beta\beta$ and $0\nu\beta\beta$ decays. A neutron's d quark emits a W^- that decays into e^- and $\overline{\nu}$. If the neutrino is its own antiparticle, $0\nu\beta\beta$ decay can occur with the annihilation of the two emitted antineutrinos. Right: energy spectrum expected due to $2\nu\beta\beta$ decay (blue curve). The sharp peak at Q-value corresponds to the $0\nu\beta\beta$ decay.

massive nature of the neutrinos. The importance and success of the neutrino oscillation search was reflected in the Nobel prize of 2015 [11].

1.2 Neutrinoless Double Beta Decay

The dominance of matter over antimatter in the Universe is one of the most puzzling questions that modern physics aims to reveal. As the Big Bang should have created an equal amount of matter and antimatter, one of the possible explanation for the matter excess is the baryonic number violation via leptogenesis, generated by the massive right-handed neutrinos [12, 13].

According to SM, neutrinos are massless left-handed particles [14]. However, the enormous number of neutrino oscillation experiments carried out in the last decays have proved the existence of neutrinos' mass eigenstates. Additional indication showing that the SM is not complete, comes from the CPT-theorem, that predicts right-handed neutrinos existence without forbidding their Majorana nature (i.e., neutrinos are their own antiparticles).

A possible confirmation of the Majorana neutrino nature and explanation of the matter dominance in the early Universe can be found in the observation of neutrinoless double beta ($0\nu\beta\beta$) decay. This decay is a hypothetical non-SM process in which two neutrons inside a nucleus undergo simultaneous β decay followed by the annihilation of two emitted $\overline{\nu}_e$. Thus, the process is expected to occur via the reaction $A(Z, N) \longrightarrow A(Z + 2, N) + 2e^-$, where the lepton number conservation is violated. In contrast, ordinary double beta decay ($2\nu\beta\beta$) is a SM process, which occurs via $A(Z, N) \longrightarrow A(Z + 2, N) + 2e^- + 2\overline{\nu}_e$, and has been already observed for several isotopes (see Ref. [15, 16, 17]). Fig. 1.1 shows the Feynman diagram and signature for both processes. Assuming that the energy of the recoiling nucleus is negligible, the signature of the $0\nu\beta\beta$ decay is expected to be a sharp peak at the end $2\nu\beta\beta$ spectrum, at the $Q_{\beta\beta}$ value.

The mechanism responsible for $0\nu\beta\beta$ decay is not yet fully understood and a number of the experiments described in Section 1.7 and beyond aim to reveal it. One of the probable explanations is that the decay is mediated by an exchange of a light Majorana neutrino with the the effective Majorana mass [18].

1.3 Effective Majorana Neutrino Mass

The effective Majorana neutrino mass is a coherent sum of the PMNS matrix elements (U_{ei}) and neutrino mass eigenvalues m_i [18]:

$$\left|m_{\beta\beta}\right| = \left|\sum_{i=1}^{3} U_{ei}^2 m_i\right|, \tag{1.4}$$

where U_{ei} are the elements of the first row of the PMNS mixing matrix. The unitary lepton mixing matrix PMNS describes the mixing of neutrino mass eigenstates and defined as follows:

$$\mathrm{U} = \begin{pmatrix} \mathrm{c}_{12}\mathrm{c}_{13} & \mathrm{s}_{12}\mathrm{c}_{13} & \mathrm{s}_{13}\mathrm{e}^{-\mathrm{i}\delta} \\ -\mathrm{s}_{12}\mathrm{c}_{23} - \mathrm{c}_{12}\mathrm{s}_{23}\mathrm{s}_{13}\mathrm{e}^{\mathrm{i}\delta} & \mathrm{c}_{12}\mathrm{c}_{23} - \mathrm{s}_{12}\mathrm{s}_{23}\mathrm{s}_{13}\mathrm{e}^{\mathrm{i}\delta} & \mathrm{s}_{23}\mathrm{c}_{13} \\ \mathrm{s}_{12}\mathrm{s}_{23} - \mathrm{c}_{12}\mathrm{c}_{23}\mathrm{s}_{13}\mathrm{e}^{\mathrm{i}\delta} & -\mathrm{c}_{12}\mathrm{s}_{23} - \mathrm{s}_{12}\mathrm{c}_{23}\mathrm{s}_{13}\mathrm{e}^{\mathrm{i}\delta} & \mathrm{c}_{23}\mathrm{c}_{13} \end{pmatrix} \times \begin{pmatrix} 1 & 0 & 0 \\ 0 & \mathrm{e}^{i\alpha} & 0 \\ 0 & 0 & e^{i\beta} \end{pmatrix}, \tag{1.5}$$

where the following CP-violating (CPV) phases are introduced: Dirac (δ) and two Majorana (α and β) phases; $\mathrm{s}_{ij}(\mathrm{c}_{ij})$ is the sine(cosine) of the neutrino mixing angle ϑ_{ij} the latest measured values for which can be found, e.g., in Ref.[19]. The measurements of the reactor oscillation experiments yield $\delta \cong 3\pi/2$ [19]. The values of Majorana phases are, however, still unknown and may vary between 0 and 2π.

1.3.1 Neutrino Mass Eigenvalues

The neutrino mass eigenvalues in Eq. (1.4) are still unknown, but some constraints from neutrino oscillation and cosmological experiments exist on $\sum_i m_i$ and on Δm_{ij}^2, being $\Delta m_{ij}^2 \equiv \left(m_i^2 - m_j^2\right)$ $(i \neq j)$ is a parameter of neutrino oscillations (see Eq. (1.1)).

The constraints on $\sum_i m_i$ are widely discussed in the literature for various cosmological scenarios. The strongest limit yields [20]:

$$\sum_i m_i < 0.12\,\mathrm{eV}\,(95\%C.L.). \tag{1.6}$$

While some models extend the limit to [21]:

$$\sum_i m_i < 0.66\,\mathrm{eV}\,(95\%C.L.). \tag{1.7}$$

The value of Δm_{21}^2 was measured in solar ν_e oscillation experiments [22] and in reactor $\overline{\nu}_e$ oscillation by KamLAND [23]. Their results showed that:

$$\Delta m_{12}^2 = m_2^2 - m_1^2 > 0, \tag{1.8}$$

which leads to $m_1 < m_2$. The best fit estimates from the combined results of the experiments yields $\Delta m_{12}^2 = 7.37 \cdot 10^{-5}\,\mathrm{eV}^2$.

The value of Δm_{31}^2, responsible for the atmospheric ν_μ oscillations, is such that $\Delta m_{12}^2 < \Delta m_{31}^2$,

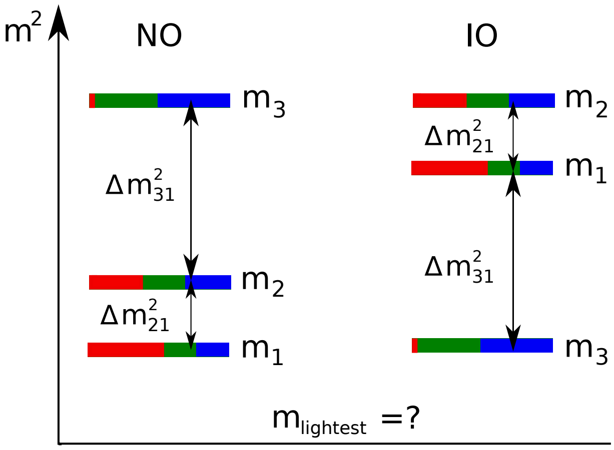

Figure 1.2: Two possible scenarios of the mass ordering: NO and IO. Each neutrino mass eigenstate m_i (i=1,23) is the superposition of the flavor eigenstates m_l (l=e, μ, τ). The proportional contribution is schematically depicted with the lengths of red, green, and blue bands. The still unknown parameters are the absolute mass of the lightest neutrino (m_1 for NO or m_3 for IO), and the sign of Δm^2_{31}.

and one of the latest results reports $2.5{\cdot}10^{-3}\mathrm{eV}^2$ [18]. The sign of Δm^2_{31} is, however, still the research subject of several neutrino experiments. In particular, long-baseline experiments such as T2K [24], Nova [25], and Dune [26], looking for oscillations in the channel $\nu_\mu \to \nu_e$ aim to resolve this question.

Given the present ambiguity of the Δm^2_{31} sign and the smallness of Δm^2_{12}, two possibilities arise for the neutrino mass ordering: $m_1 < m_2 < m_3$, or $m_3 < m_1 < m_2$. The first relationship defines a normal mass ordering (NO), and the second defines an inverted mass ordering (IO). Schematically, both scenarios are illustrated in Fig. 1.2.

The $|\mathrm{m}_{\beta\beta}|$ in Eq. (1.4) is typically expressed through the mass of the lightest neutrino m_l, where $m_l = m_1$ for NO, or $m_l = m_3$ for IO. The allowed parameter space for $|\mathrm{m}_{\beta\beta}|$ depending on m_l is shown in Fig. 1.3 for NO and IO. The solid color bands indicate the $|\mathrm{m}_{\beta\beta}|$ values limited by the unknown Majorana phases, while the shadowed bands around them indicate the uncertainties from the oscillation parameters. For a certain range of the m_l the allowed parameter space for the $|\mathrm{m}_{\beta\beta}|$ coincide for both neutrino mass ordering, i.e., degenerate effective Majorana mass range. As the figure demonstrates, there exist a range of the values for parameters involved in Eq. (1.4), such that $|\mathrm{m}_{\beta\beta}|$ takes a zero value in case of the NO for neutrino mass.

1.4 Double beta emitters

The choice of the $\beta\beta$ emitting isotope is crucial for the experimental search for the $0\nu\beta\beta$ decay. The observation of this rare decay requires a very high suppression of background events, which mostly originated from naturally occurring radioactivity, cosmic rays, and $2\nu\beta\beta$ decay.

The $0\nu\beta\beta$ decay can be potentially observed for 11 even-even nuclei, for which the ordinary β decay is energetically forbidden or suppressed due to a large angular momentum difference between the mother and the daughter nuclide. A configuration of charge and atomic mass allowing the $0\nu\beta\beta$ decay is demonstrated with the Bohr-Wheeler parabolic functions in Fig. 1.4.

Another essential criterion for the choice of the isotope is the Q-value of the decay. Given

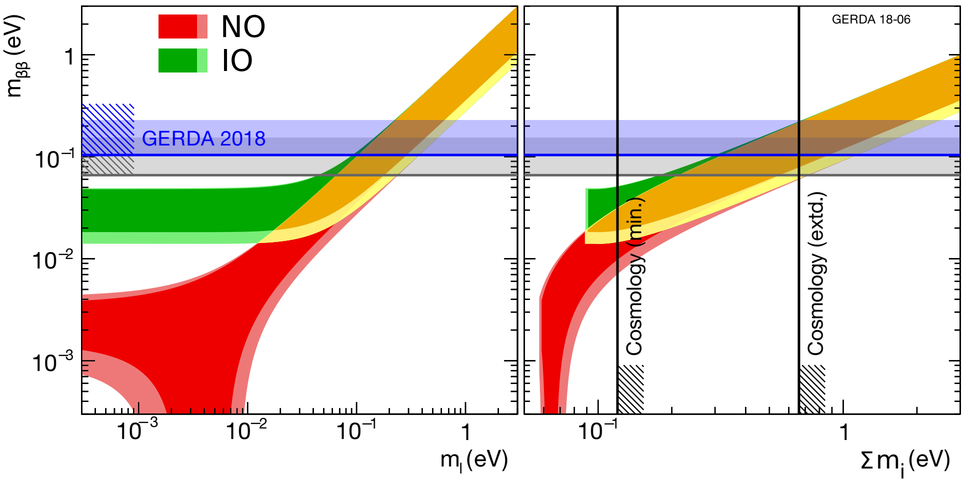

Figure 1.3: Allowed parameter space for the $|m_{\beta\beta}|$ depending on the mass of the lightest neutrino (left) and the sum of the masses (right). The solid bands indicate the values limited by the unknown Majorana phases, while the shadowed bands show the uncertainty on the oscillation parameters involved in the $|m_{\beta\beta}|$. The yellow band indicates the degenerate effective Majorana mass. The blue band indicates the limits established by the Gerda experiment, and the grey band indicates the combined sensitivity of some of the leading $0\nu\beta\beta$ decay search experiments [27, 28, 29, 30, 31]. The vertical black lines limit the values of $|m_{\beta\beta}|$ according to the cosmological observations [20, 21]. The figure is adapted from [32].

the dominant natural radioactivity due to the ^{228}Th decay chain, the Q-value preferably should be above 2.6 MeV. A Q-value above 3.3 MeV could be an additional advantage, allowing to overpass the decay series released in ^{238}U decay chain.

Given the rarity of the $0\nu\beta\beta$ decay, another requirement on the isotope is to have a high isotopic abundance of the element or to have the possibility of enriching the material. Most of the $\beta\beta$ emitting isotopes have a natural abundance <10% except for ^{130}Te (34.5%).

The above criteria result in the most commonly studied isotopes, that are listed in Table 1.1 together with the Q-value and the isotopic abundance. The $0\nu\beta\beta$ decay of ^{76}Ge has the lowest $Q_{\beta\beta}$, however, this is compensated by the superior energy resolution of germanium detectors.

1.5 Half-life of the $0\nu\beta\beta$ Decay

The $0\nu\beta\beta$ decay half-life given the light Majorana neutrino exchange can be expressed as [35]:

$$(T_{1/2}^{0\nu\beta\beta})^{-1} = G^{0\nu}(Q,Z) g_A^4 |M^{0\nu}|^2 |m_{ee}|^2, \tag{1.9}$$

where $G^{0\nu}(Q,Z)$ is a phase space factor (PSF), $M^{0\nu}$ is the nuclear matrix element (NME), and g_A is the axial coupling constant of the nucleon.

The PSF containing the final state density, is proportional to $Q_{\beta\beta}$ and expressed in units of yr^{-1}. Its value is computed numerically by integrating the electron wave functions. The first calculations were performed by Primakoff and Rosen in the 1950s [37]. The latest results are presented in the Ref. [36, 38, 39]. Fig. 1.5 illustrates the changes in the PSF with respect to the earliest calculations. The PSF values for $\beta\beta$ emitters are listed in Table 1.1.

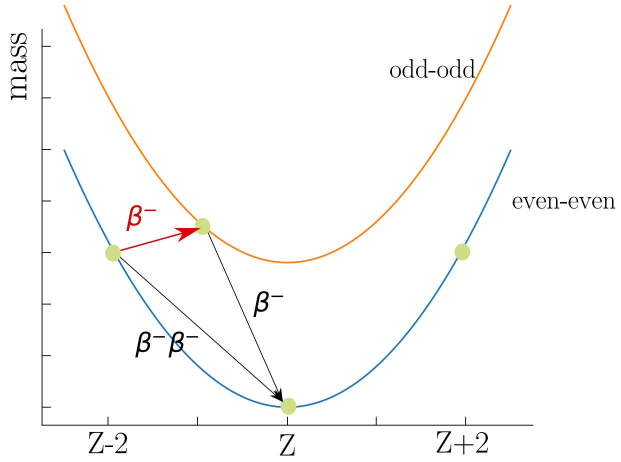

Figure 1.4: Schematic representation of a Bohr-Wheeler isobaric mass parabola [33] for odd-odd (orange) and even-even (blue) nuclei. The observation of the $0\nu\beta\beta$ decay (denoted as $\beta^-\beta^-$) is possible only for even-even nuclei if ordinary β decay is forbidden due to a higher mass of the daughter isotope or suppressed due to a large angular momentum difference between the daughter and the mother isotopes.

The NME is calculated assuming that the decay occurs to the ground or the first excited states of the daughter isotope. The NME computation has to consider the complicated nuclear structure of the open shell nuclei and, therefore, relies on specific theoretical models. The most common models are Interacting Shell Model (ISM) [40, 41], Quasiparticle Random Phase Approximation (QRPA) [42], and Interacting Boson Model (IBM-2) [43]. The models differ within the assumptions made for the nucleon interactions. The comparison of NME estimated by those models is presented in Fig. 1.6. Concerning ^{76}Ge, the values vary between three and five across the models.

One of the significant sources of uncertainties in Eq. (1.9) is the value of g_A. The widely accepted value in the literature [44, 45] is the quenched form of g_A (due to possibly omitted degrees of freedom in the computations):

$$\mathrm{g_{A,q}} = \mathrm{g_A} \cdot \mathrm{A}^{\gamma}, \tag{1.10}$$

where $\mathrm{g_A}$ is the axial coupling for the free neutron (A = 1) varying between 1.25 and 1.27, and γ is the quenching factor varying between -0.12 and -0.18 [44, 45].

1.5.1 Experimental Sensitivity

From the observation of N_s events of $0\nu\beta\beta$ decays, given that the initial number of the $\beta\beta$ emitters ($N_{\beta\beta}$) decreases exponentially with the observation time (T), the half-life can be calculated as follows:

$$t^{1/2}_{0\nu} = \ln 2 \cdot T \cdot \varepsilon \cdot \frac{N_{\beta\beta}}{N_\mathrm{s}}, \tag{1.11}$$

where ε is the detection efficiency. If no signal is observed, one would seek a half-life corresponding to the maximum signal of the process that can be hidden under the background fluctuations at a given statistical confidence level (C.L.). This figure of merit defines the experimental sensitivity for the $0\nu\beta\beta$ decay [47].

Table 1.1: The list of isotopes for which the observation of the $0\nu\beta\beta$ decay is possible. The table summarizes the Q-values of the $0\nu\beta\beta$ decay, the natural abundance of the isotopes, and the PSF. Values are taken from [34].

Isotopes	$Q_{\beta\beta}$ [keV]	Nat. abundance [%]	$G^{0\nu}$ $\left[10^{-14} yr^{-1}\right]$
^{48}Ca	4273.7	0.187	6.35
^{76}Ge	2039.1	7.8	0.623
^{82}Se	2995.5	9.2	2.70
^{96}Zr	3347.7	2.8	5.63
^{100}Mo	3035.0	9.6	4.36
^{110}Pd	2004.0	11.8	1.40
^{116}Cd	2809.1	7.6	4.62
^{124}Sn	2287.7	5.6	2.55
^{130}Te	2530.3	34.5	4.09
^{136}Xe	2461.9	8.9	4.31
^{150}Nd	3367.3	5.6	19.2

Assuming Poisson fluctuations for the number of background events N_B, the number of signal events hidden under the background fluctuations is $\sqrt{N_B}$. In this way, the sensitivity for the $0\nu\beta\beta$ decay half-life, $S^{o\nu}$, would be expressed similarly to Eq. (1.11), as:

$$S^{0\nu} = \ln 2 \cdot T \cdot \varepsilon \cdot \frac{N_{\beta\beta}}{\sqrt{N_B}}. \tag{1.12}$$

The number of the $\beta\beta$ decaying isotopes can be estimated from the atomic mass (A) and the total mass of material (M) as follows:

$$N_{\beta\beta} = \epsilon N_A \cdot \frac{M}{A}, \tag{1.13}$$

where N_A is the Avogadro number and ϵ is the enrichment factor of the $\beta\beta$ isotope in the material. The expected N_B can be evaluated with the expected background rate (BI) and the energy resolution (Δ):

$$N_B = BI \cdot \Delta \cdot T \cdot M. \tag{1.14}$$

Given $N_{\beta\beta}$ and N_B, Eq. (1.12) becomes:

$$S^{0\nu} = \ln 2 \cdot \varepsilon \cdot \epsilon \frac{N_A}{A} \sqrt{\frac{M \cdot T}{BI \cdot \Delta}}. \tag{1.15}$$

Despite its simplicity, the above estimate is the most important parameter for the experimental $0\nu\beta\beta$ decay search. Eq. (1.15) clearly states that the best sensitivity to the signal can be achieved by maximizing the mass of the material and the observation time[1], minimizing the expected background rate, and enhancing the energy resolution.

For $0\nu\beta\beta$ experiments it is of particular interest the case where the background rate is below one count within the energy resolution Δ at $Q_{\beta\beta}$ during the experiment's lifetime, i.e., $N_B \lesssim 1$.

---

[1] The product of mass and observation time is typically referred to as an experimental exposure.

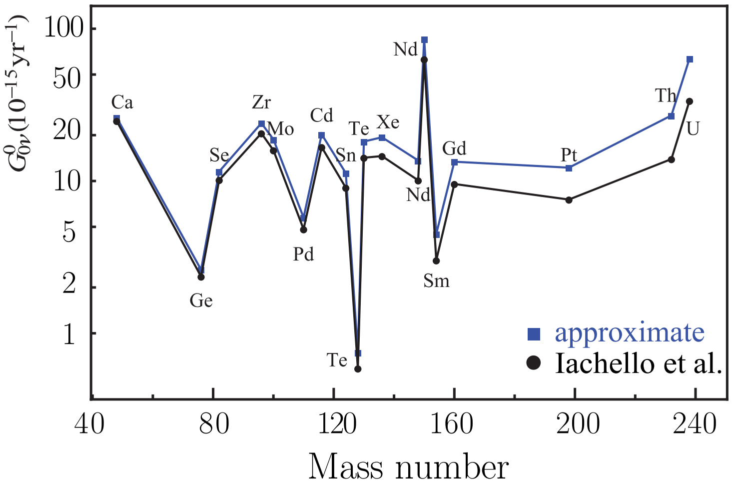

Figure 1.5: PSF for various elements estimated in [36] using exact Dirac wave functions with finite nuclear size and electron screening of a nucleus. The values are compared to earlier calculations obtained by approximating the electron wave functions at the nuclear radius without inclusion of electron screening.

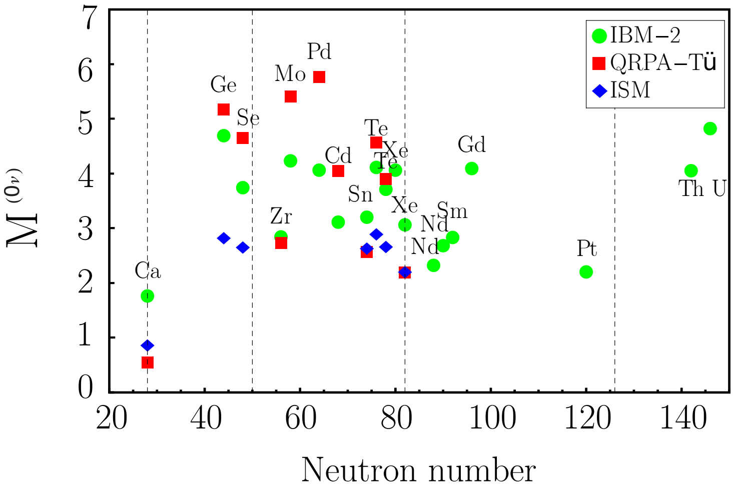

Figure 1.6: NME for different isotopes estimated with ISM, QRPA, and IBM-2 models. The figure is taken from [46].

In such a case, the total number of the expected background events is constant, and the sensitivity in the Eq. (1.15) becomes:

$$S^{0\nu} = \ln 2 \cdot \varepsilon \cdot \epsilon \frac{N_A}{A} \frac{M \cdot T}{N_s}, \tag{1.16}$$

where N_s is the number of events observed in the region of interest. As Eq. (1.16) illustrates, for BI below one count, the experimental sensitivity does not depend on the energy resolution and scales linearly with the collected exposure (M·T).

Nevertheless, the energy resolution is crucial for the observation of the $0\nu\beta\beta$ decay. As shown in [48], the ratio of the observed events from $0\nu\beta\beta$ and $2\nu\beta\beta$ decays can be approximated with the energy resolution as:

$$R_{0\nu/2\nu} \propto \left(\frac{Q_{\beta\beta}}{\Delta}\right)^6 \frac{t^{1/2}_{2\nu}}{t^{1/2}_{0\nu}}, \tag{1.17}$$

Table 1.2: List of the most significant results achieved in the field of the $0\nu\beta\beta$ decay search.

Experiment	Isotope	$T^{0\nu}_{1/2}$[yr]
CUORE [29]	^{130}Te	$> 1.3 \cdot 10^{25}$
GERDA Phase II [49]	^{76}Ge	$> 0.9 \cdot 10^{26}$
Majorana [27]	^{76}Ge	$> 2.7 \cdot 10^{25}$
Nemo-3 [50]	^{96}Zr	$> 9.2 \cdot 10^{21}$
Nemo-3 [51]	^{100}Mo	$> 1.1 \cdot 10^{24}$
Nemo-3 [52]	^{150}Nd	$> 2.0 \cdot 10^{22}$
EXO-200 [30]	^{136}Xe	$> 1.8 \cdot 10^{25}$
KamLAND-Zen [31]	^{136}Xe	$> 1.1 \cdot 10^{26}$

thus, the contribution from the $2\nu\beta\beta$ background scales as a power of six with the energy resolution.

1.6 Experimental Search for the $0\nu\beta\beta$ decay

The rise of the $0\nu\beta\beta$ decay experiments happened in the late 1990s. The experiments can be classified according to their techniques into xenon time projection chamber (TPC) experiments, Te-loaded experiments, germanium and other crystal experiments. The pioneers for each technique were Gotthard TPC [53] (xenon), Heidelberg-Moscow [54] and IGEX [55] (germanium), and Cuoricino [56] experiments (Te). Additionaly, the NEMO-3 experiment investigated the $0\nu\beta\beta$ from a variety of isotopes, namely ^{96}Zr, ^{100}Mo, ^{150}Nd [51, 50, 52], summarized in Table 1.2.

Current experiments involve continually evolving techniques, with the ambitious plans for ton-scale detector masses. The strongest achieved limits for the half-life and the sensitivity for the selected isotopes are summarized in Table 1.2. The GERDA experiment achieved the lowest background in the field, setting the strongest limit on the half-life of ^{76}Ge $0\nu\beta\beta$ decay. This Ph.D. thesis was completed in the context of GERDA and therefore Chapter 2 is devoted to a detailed description of the experiment. Another experiment searching for the $0\nu\beta\beta$ of ^{76}Ge is the MAJORANA Demonstrator [27, 57]. The experiment is located at the Sanford Underground Laboratory in Lead, South Dakota, and utilizes ^{76}Ge detectors with a total mass of 40 kg. MAJORANA Demonstrator operates detectors cooled by liquid nitrogen, which additionally serves as passive shielding against external radioactivity.

The EXO-200 experiment [30] is located at the Waste Isolation Pilot Plant (WIPP) near Carlsbad, New Mexico. This experiment uses a TPC filled with liquid xenon (LXe) enriched to 80.6% in ^{136}Xe. The experiment is planning an upgrade phase to increase the mass of xenon to the ton-scale and reach a half-life sensitivity of 10^{28} yr [58].

The KamLAND-Zen experiment [31] is located at the Kamioka Observatory, an underground neutrino detection facility near Toyama, Japan. The detector consists of 13 tons of Xe-loaded liquid scintillator. The limit established by this experiment is the strongest for the half-life of the $0\nu\beta\beta$ decay in the field (see Table 1.2).

The CUORE experiment [29] is looking for the $0\nu\beta\beta$ decay of ^{130}Te. This experiment is located at Laboratori Nazionali del Gran Sasso (LNGS) in Italy. The Cuore-0 was completed in 2016, and the results from the combined analysis with the first stage of the experiment, Cuoricino, are provided in Table 1.2.

1.7 Future Generation of Experiments

The strongest limits on the $0\nu\beta\beta$ half-life were set by the germanium and xenon experiments (see Table 1.2), covering the degenerate effective Majorana neutrino mass region (see Fig. 1.3). Given the availability for the enrichment and scalability of experiments, those techniques provide a possibility for building ton-scale experiments to reach the sensitivity of 10^{28} yr on the $0\nu\beta\beta$ decay half-life, and to cover the predicted parameter space for effective Majorana mass in the scenario of the inverted neutrino mass hierarchy.

Xenon Experiments

The proposed up-today ton-scale experiments to search for $0\nu\beta\beta$ decay of ^{136}Xe are the nEXO [59] (continuation of EXO-200) and a new experiment DARWIN [60]. The nEXO experiment plans to deploy ~5 t of LXe with the enrichment to 90% of ^{136}Xe. The location of the experiment is planned to be at the underground facility of SNOLAB, Canada. The DARWIN experiment will be located at LNGS laboratory and will deploy 40 t of LXe with a natural abundance of ^{136}Xe (8.9%).

These experiments aim to achieve an energy resolution of $\frac{\sigma_E}{E} \sim 1\%$ at 2458 MeV ($Q_{\beta\beta}$ of ^{136}Xe $0\nu\beta\beta$ decay) and unprecedented levels of background. To improve the energy resolution, the experiments consider an extensive usage of silicon photomultipliers (SiPMs) that offer lower electronic noise in comparison to photomultipliers (PMTs), which are widely deployed in the current generation of the experiments. To lower the background levels, both experiments use radioassay technique to develop the instrumentation with low-radioactivity materials.

Germanium Experiments

Recently, a new collaboration named Legend (Large Enriched Germanium Experiment for Neutrinoless $\beta\beta$ Decay) was formed between the Gerda and the Majorana collaborations [57], plus additional scientific groups. Legend plans its physics program in several stages. The first stage, Legend 200 [61], intends to deploy 200 kg of germanium; it will be located, as Gerda , at LNGS and it will use much of the Gerda experiment's existing infrastructure. New hardware, electronics, and software are already under discussion as part of the development of the new experiment. Additionally, Gerda has developed and currently testing a new type of detector (see Ref. [62]), which can offer to Legend a compromise between the increased mass and the size of the readout electrode, that is crucial to keep the electronic noise in the detector's signal at minimum.

Chapter 2

The GERDA Experiment

The GERDA experiment was designed to search for neutrinoless double beta decay ($0\nu\beta\beta$) of ^{76}Ge. For this search, the experiment deploys High-Purity Germanium (HPGe) detectors with a total mass of 40 kg. Most of the detectors are enriched in ^{76}Ge up to an abundance of 87%. The detectors are operated immersed in liquid argon (LAr), that serve as coolant, and active and passive veto shield against external backgrounds. The experiment is located underground, at Laboratori Nazionali del Gran Sasso (LNGS) of Istituto Nazionale di Fisica Nucleare (INFN), Italy. The experiment's physics program is divided into two phases. Phase I ran from 2011 to 2013; after substantial upgrades, the experiment started its Phase II in 2015. This phase is currently active and collecting data.

This chapter covers the detector configuration as operated until the minor upgrade of the setup in the summer of 2018. The data collected until this update was analyzed and results for the $0\nu\beta\beta$ decay search were presented in Ref. [49]. The chapter is organized as follows. Section 2.1 highlights the primary goals of the GERDA experiment and its current phase of data taking. Section 2.2 details the experimental setup with focus on the germanium detectors. Section 2.5 presents the critical ingredients of the $0\nu\beta\beta$ decay search and the latest results achieved by the GERDA collaboration.

2.1 Goals of the GERDA Phase II

After substantial upgrades to the experimental setup [63], Phase II began in 2015. The primary goal of the GERDA Phase II was to increase the sensitivity for the $0\nu\beta\beta$ decay half-life of ^{76}Ge by about one order of magnitude reaching a value of 10^{26} yr, which had not been previously accomplished in the field. As discussed in Chapter 1, the sensitivity depends on the collected exposure and background index (BI); therefore, the goal of the upgrade was to optimize these two parameters.

To achieve the sensitivity goal with the projected exposure of 100 kg·yr, GERDA required a reduction of the BI to at least 10^{-3} cts/(keV·kg·yr). The background reduction for the Phase II was particularly challenging given the increased number of detectors by a factor of four (40 vs. 11 in Phase I) and, consequently, the increased amount of material surrounding the detector array (cables, crystal holders, and support structure for the detector strings). In addition, to enhance the rejection of the external background, the collaboration designed an active liquid argon (LAr)

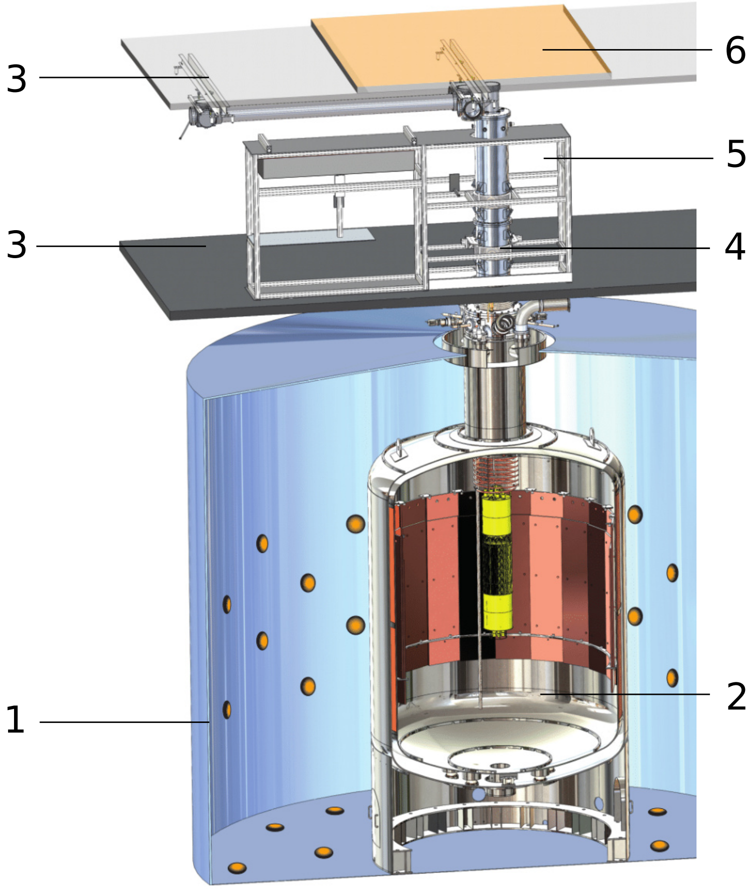

Figure 2.1: Experimental setup of the GERDA experiment with the main parts identified. 1, water tank instrumented with PMTs; 2, LAr cryostat; 3, floor and roof of the clean room; 4, lock of the cryostat; 5, glove box; 6, plastic scintillator muon veto. Figure adapted from [65].

veto instrumented with photosensors for the scintillation light detection, which also contributes to the amount of material around the detectors. Thus, the design of LAr instrumentation was a compromise between the background rejection and the amount of deployed material. Therefore, only high radio-purity materials were selected for the upgrade campaign and design of the active LAr veto.

2.2 Experimental Setup

The GERDA experiment is located in Hall A at LNGS [64]. The surrounding rock of the Gran Sasso mountain massif provides an overburden of 3.5 km in water equivalent, which eliminates the hadronic and electromagnetic components of cosmic ray showers and reduces the μ background flux to ~1 m^{-1} hr^{-1}.

The setup of the experiment, including the main features, is depicted in Fig. 2.1. The muon veto consists of three 12 m^2 plastic scintillator layers located on the top of the clean room, and water tank, which is the outermost part of the experiment. The tank is filled with 590 m^3 of high-purity water and instrumented with 66 8" photomultiplier tubes (PMTs) to detect Cherenkov light created by the passing through muons. Additionally, the layer of water serves as a passive shielding against environmental gamma radiation and neutron backgrounds. This muon veto

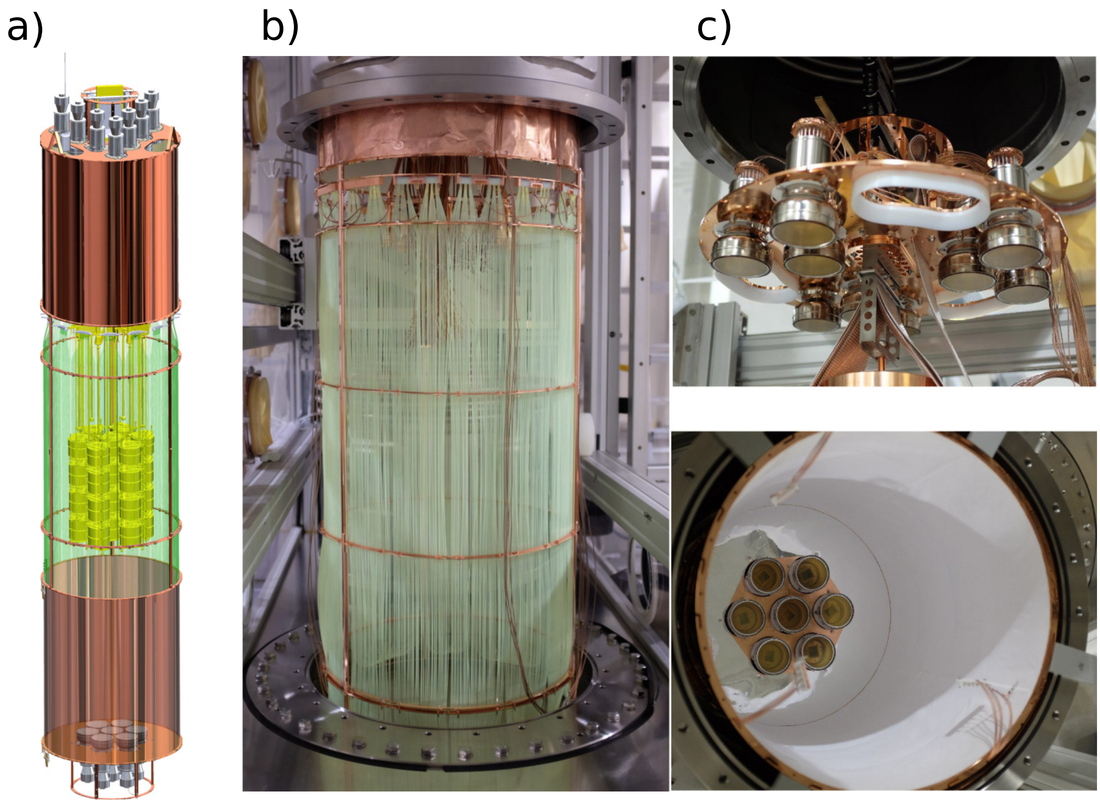

Figure 2.2: LAr veto system: a, technical (CAD) drawing; b, photograph of the fiber shroud; c, top and bottom PMT arrays. The WLS TPB coating is applied to all the reflective surfaces, as explained in the text.

system rejects muons with more than 99.8% efficiency.

Inside the water tank is a stainless steel cryostat with a 6 cm thick oxygen-free radio-pure copper layer on its inner surface for future background reduction due to radioactivity contained in the cryostat walls. The cryostat is filled with 64 m^2 of LAr, which provides passive shielding against external gamma radiation and cooling of germanium detectors down to their operating temperature of $\sim$90 K. To enhance the external background reduction, the cryostat was instrumented with light sensors, forming an active veto, to detect the scintillation light of the LAr, produced by the ionizing particles [63].

The LAr veto is schematically depicted in Fig. 2.2 (a). On the top and bottom, the LAr veto is instrumented with 16 3” PMTs, illustrated in Fig. 2.2 (c), and SiPMs connected to wavelength-shifting (WLS) fibers surrounding the detector array depicted in Fig. 2.2 (b). The purpose of the instrumented WLS fiber curtain was to ensure maximum coverage of the array with the light sensors with minimum surrounding material [63]. The tetraphenyl-butadiene (TPB) coating is applied to the surface of each fiber to shift the light from 128 nm - the wavelength of LAr scintillation light - to the visible blue region (430 nm). The light from the WLS fibers is readout by the SiPMs instrumented on the top of the cryostat. Nine fibers are coupled to one SiPM; the signals from six SiPMs are readout by one flash analog-to-digital converter (FADC) channel with 12.5 MHz sampling frequency into 120 μs traces. The signals from the PMTs are digitized at 100 MHz and 12 μs long traces.

The germanium detectors arranged in the vertical arrays, called strings (see Fig. 2.3), are directly immersed in LAr. The detectors are of two types: semi-coaxial and Broad Energy

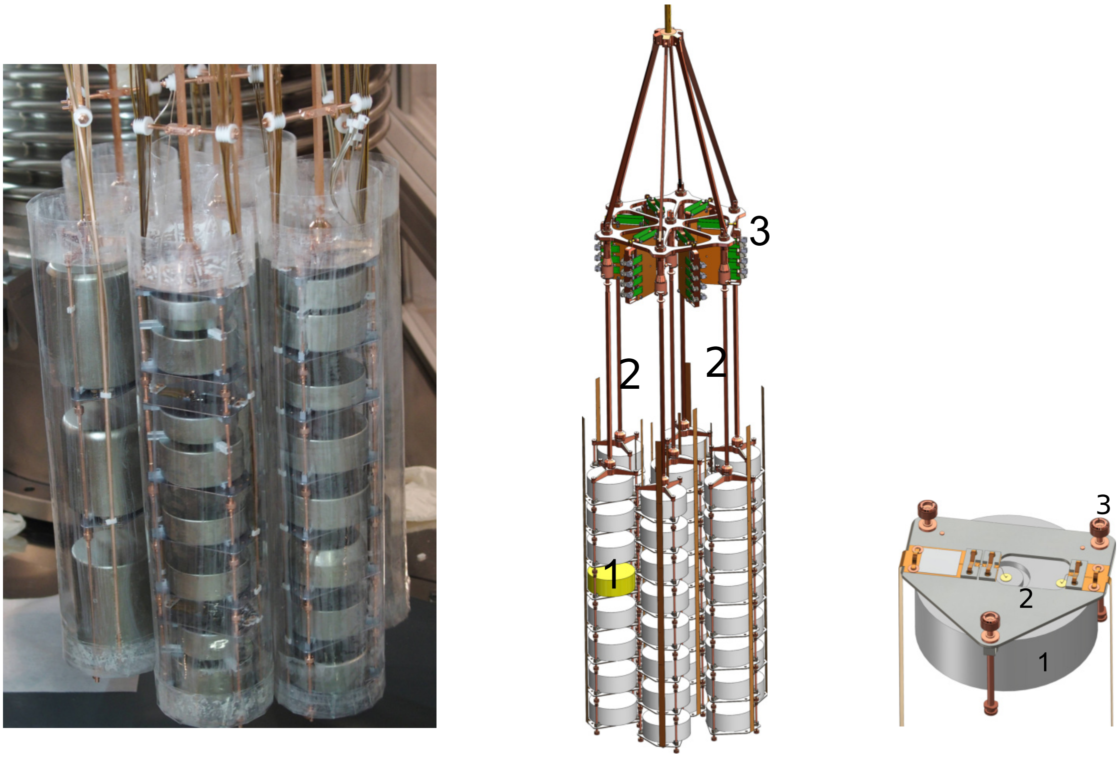

Figure 2.3: Left: a photograph of the detectors strings surrounded by the transparent nylon mini-shrouds; the string of coaxial detectors is visible on the left, and the strings of BEGe detectors at middle and right. Middle: detectors (1) arrangement in the array with the preamplifiers (3) and voltage and readout cables (2). Right: schematic illustration of the detector module (1) and silicon holder (2) with the high-purity copper rods (3).

Germanium (BEGe) [63]. All but three of the detectors are enriched in ^{76}Ge to ≈ 87% [66, 63]. The other three are coaxial-type detectors with a natural abundance of ^{76}Ge of 7.8%. To mitigate the background originating due to ^{42}K decay (arising from ^{42}Ar β decay in LAr), each detector string is enclosed by a nylon cylinder, known as a nylon mini-shroud, as illustrated in Fig. 2.3 (left). The mini-shrouds, similar to the fibers, are coated with the TPB to provide wavelength shifting of the scintillation light. A detector module with its support structure is shown in Fig. 2.3 right. For the Phase II the copper holders used in Phase I were replaced with silicon holders to reduce the observed activities of ^{228}Th and ^{226}Ra. All the materials surrounding the detectors were carefully selected using screening measurements to minimize their background contribution to the $0\nu\beta\beta$ search region [63].

2.3 Germanium Detectors

The following section describes the properties of semiconducting materials that are relevant for understanding the GERDA detectors' performance. The description is adapted from Ref. [67].

Semiconductors

All solid materials can be classified into one of the following categories according to their conductivity properties: insulators, conductors, and semiconductors. A material's conductivity

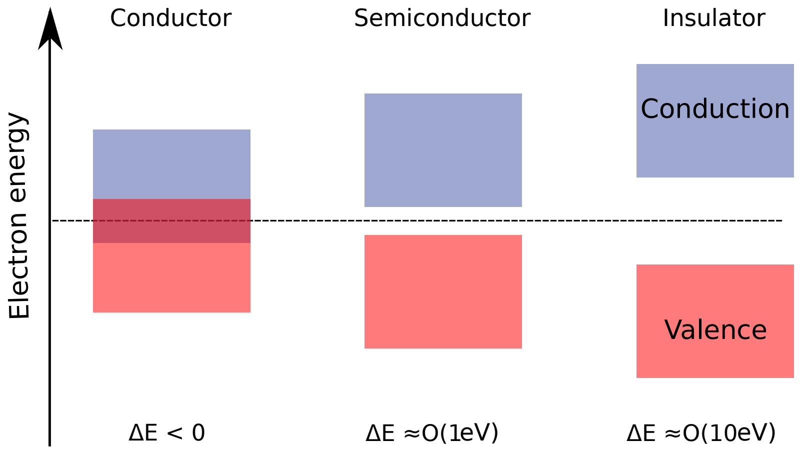

Figure 2.4: Classification of the materials by the energy gaps between the valence and conduction bands. For conducting materials, the conduction and valence band overlap; for insulators and semiconductors, the energy gap between the bands is of O(10 keV) and of O(1 keV), respectively.

properties are typically determined by the occupation of valence and conduction bands and the energy separation between those bands as demonstrated in Fig. 2.4.

In an insulator, charge carriers fully occupy the valence band, and the energy gap between the valence and conduction bands is typically too large (O(10 eV)) for thermally excited electrons to overcome it. A conductor's valence band is partly occupied due to the overlap with the conductivity band; therefore, these materials have the highest conductivity properties. For semiconductors, the material's valence band is fully occupied with the charge carriers, but the distance to the conduction band is small enough (O(1 eV)) that thermally excited electrons can overcome it. In the conduction band, those electrons act as charge carriers and consequently induce the charge current in the material.

By cooling semiconductors to a certain level (for example, using LAr or nitrogen), thermal currents can be minimized. Therefore, most current in semiconductor will be induced by non-thermal processes, such as particles interacting in the material.

In the semiconductor material, the result of the particle interaction is the excited electrons, the number of which is different for each material and characterized by ϵ, the energy needed to excite an electron. For germanium, $\epsilon = 2.96\,\mathrm{eV}$. Each excited electron in the conduction band forms a pair with a vacancy from the valence band, called an electron-hole pair. Electrons and holes are respectively negative and positive charge carriers; the formation of n electron-hole pairs is expected to be a statistical Poisson process with an uncertainty of $\Delta n = \sqrt(n)$. However, in practice, the creation of an electron-hole pair alters the local electron distribution, which makes the production of multiple electron-hole pairs non-independent events. This interdependence is encapsulated in the Fano factor F, which defines the experimentally observed uncertainty value on the number of the produced pairs from the deposited energy E with respect to the uncertainty predicted by the Poisson statistics. The statistical uncertainty on n becomes $\Delta n = \sqrt(F \cdot n)$. Several measurements to determine the Fano factor for germanium were performed in last century by estimating the resolution of known γ in the energy spectra [68, 69]; the most often quoted values are between 0.1 and 0.12.

Donor or acceptor impurities in the semiconductor cause an increased number of electrons

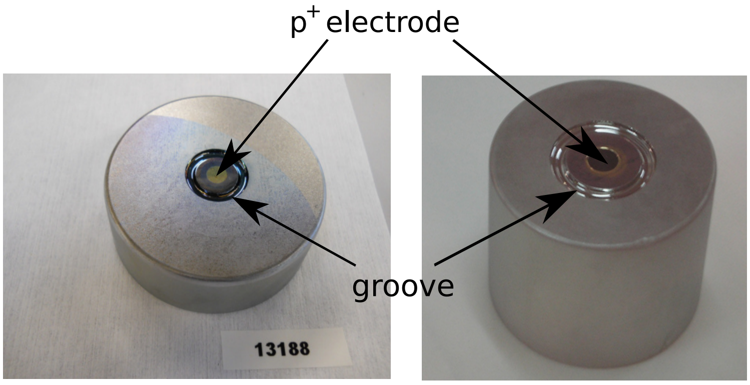

Figure 2.5: Photograph of the BEGe (left) and coaxial (right) detectors with indicated p$^+$ electrode in the middle, and the groove around it (dimensions of the photographs are not to scale).

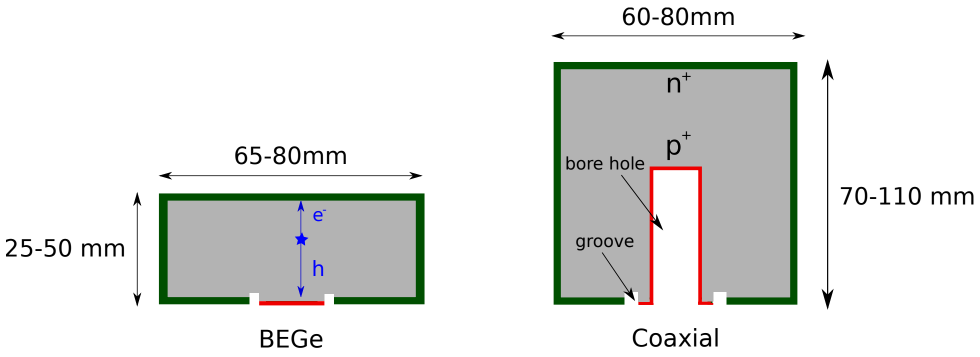

Figure 2.6: Schematic cross-section and indicated dimensions of BEGe (left) and coaxial (right) detectors. The electrons and holes created due to particle's interaction drift to n$^+$ (shown in green) and p$^+$ (shown in red) electrodes, respectively.

or holes, respectively, forming n-type or p-type materials. A specific combination of p-type and n-type semiconductors creates a so-called diode. In a diode, at the junction of n-type and p-type materials, the charge carrier diffuses into materials of the opposite type, leaving this area without charge carriers, i.e., the depletion region. The depletion region forms the detector's active volume. By applying a positive high voltage (HV) to the n-type surface, and negative HV to the p-type surface, the active volume can be increased up to $\sim$90% detector's volume by accumulating electrons and holes on the electrodes [70].

High Purity Germanium (HPGe) Detectors in Gerda

Each detector in Gerda is produced from a single p-type germanium crystal. The p$^+$ electrode - an electrode on the top of p-type material - is created by implantation of boron atoms with an ion beam. The n$^+$ electrode is created by thermal diffusion of lithium atoms. The contacts are separated by a groove around the p$^+$ contact, such that the semiconducting junction is concentrated between them. The high voltage which depletes an active volume is applied to the n$^+$ contact, and the signal is readout from the grounded p$^+$ contact. The n$^+$ electrode with the thickness of about 0.5 mm defines the detector's dead layer, i.e., the shield layer to the detector's active volume from certain types of radiation, such as α particles in particular.

Two different types of Gerda detectors are shown in Fig. 2.5 and their schematic with

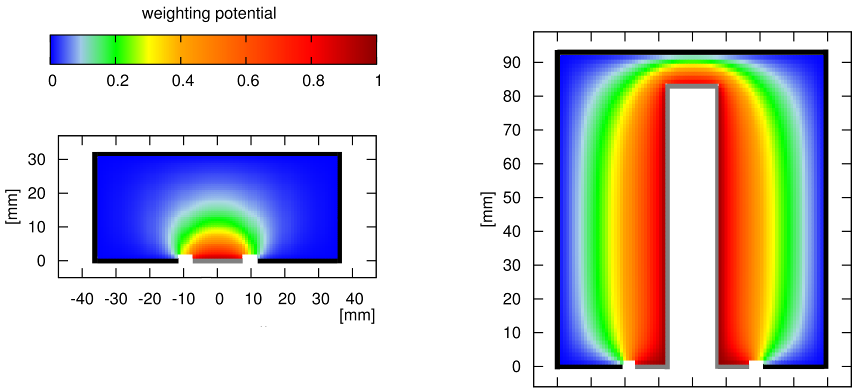

Figure 2.7: Cross-section of a typical BEGe (left) and coaxial (right) detector with the distribution of the weighting potential inside of the detector's volume, normalized to its maximum, that is close to p^+ readout electrode. The figure is from Ref. [73].

corresponding dimensions in Fig. 2.6. The coaxial detectors were inherited from the former Heidelberg-Moscow and IGEX experiments [54, 55, 71]. In total, seven enriched coaxial detectors were deployed in Gerda. The Broad Energy Germanium detectors (BEGe) have been specially produced for the Phase II campaign; the production of BEGe detectors is described in Ref. [72]. These detectors have enhanced energy resolution, background rejection capabilities, and better performance stability compared to the coaxial detectors. Three coaxial detectors with a natural abundance of ^{76}Ge (7.8‰) were deployed in Gerda as well. These detectors were not used for $0\nu\beta\beta$ search due to the low ^{76}Ge abundance but were used to reject background events that occur in coincidence with the enriched detectors.

2.4 Signal Formation and Readout

The result of a particle's interaction within the detector's active volume is the creation of electron-hole pairs, the average number of which is proportional to the energy deposited by the particle, as described in Section 2.3. If no voltage is applied, the pairs drift within the lattice under the thermal diffusion. If a voltage is applied to the detector, the drift velocity is increased. The maximum possible drift velocity does not depend on the applied voltage, called saturated drift velocity, is about 10^7 cm/s. In Gerda , the applied voltage to the n^+ electrode varies between 2 and 5 kV, such that it allows for the full depletion of the active volume of each detector.

The created electrons and holes drift to the electrodes of the opposite sign under the electrical field and due to impurities gradient along the detector's axis. This drift creates the mirror charge on the electrodes (Q), which can be estimated from Shockley-Ramo theorem [74, 75], as:

$$Q = -q \cdot W(x). \tag{2.1}$$

where W(x) is the weighting potential for the charge q at the positions x. The weighting potential determines the coupling of a charge cluster to a given electrode, and it increases gradually between n^+ and p^+.

The computation of the weighting potential for Gerda germanium detectors was performed in Ref. [76]; its distribution for the coaxial and BEGe detectors is shown in Fig. 2.7. If initial

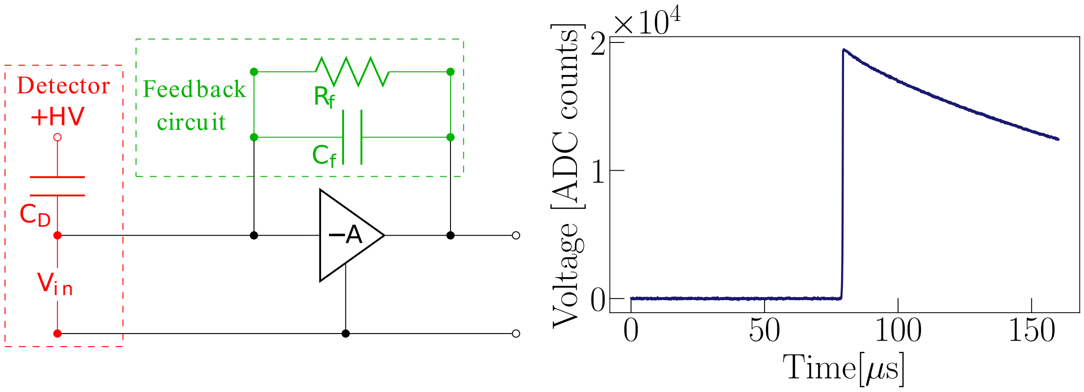

Figure 2.8: Left: the signal readout circuit. The charge pulse from the detector's p^+ electrode is collected by the preamplifier and feedback capacitor (C_f), which then discharges through the feedback resistor (R_f). Right: digitized pulse of the preamplifier output.

electron-hole pairs are produced close to the p^+ contact, where the weighting potential is at maximum, the charge collection occurs within the shortest time (below $1\,\mu$s as seen in Fig. 2.11); these charges are classified as fast pulses. Conversely, if the charge is produced close to the n^+ contact, the charge collection time is longer because the charge first needs to diffuse to the lattice volume through the dead layer, these charges are classified as slow pulses.

The electrical circuit for the signal readout is shown schematically in Fig. 2.8. The charge formed on the p^+ contact is collected by a charge sensitive preamplifier (A) and a feedback capacitor (C_f), which is discharged via a feedback resistor (R_f), connected in parallel. The preamplifiers are located above the array, as shown in Fig. 2.3 left, and connected to the p^+ electrodes via approximately 40 cm long cables. From the preamplifiers, the signal is transmitted outside of the cryostat, where it is digitized with FADCs at 100 MHz into the waveforms sampled with 14 bit.

If a charge from at least one of the detectors exceeds the pre-set trigger threshold, the main trigger is issued, and the signal is recorded from all germanium detector channels. A typical output of this electric circuit is shown in Fig. 2.8, right. It is characterised by $80\,\mu$s of the baseline signal, the fast risetime (0.5-1 μs) and the long decay tail with the time $t = 1/RC$, $t = 150\,\mu$s, $C_f = 0.3$ pF and $R_f = 500$ MOhm.

Independent on the trigger of the germanium detectors, an additional fixed-charge pulse is injected to the input of all preamplifiers about every 20 s. The recorded test pulses are used to monitor the stability of the detectors' gain, noise, and the current induced by thermal excitation of the electrons, called the leakage current.

Energy Resolution of Germanium Detectors

The energy resolution of the detectors, namely the width of the peaks in the energy spectrum, is determined by the variances on the pair production process and electronic signal detection, combined in quadratures as:

$$\omega^2 = \omega_I^2 + \omega_{\mathrm{P}}^2 + \omega_{\mathrm{C}}^2 + \omega_{\mathrm{E}}^2, \tag{2.2}$$

where the following variances are combined:

- ω - overall variance on the measured energy
- ω_I - on the energy of the released γ ray due to the Heisenberg uncertainty on the energy level upon which the γ ray is emitted. This term is negligible in comparison to other sources of uncertainty, and is typically omitted from the calculation of the energy resolutions (for ^{228}Th, $\omega_I \sim 10^{-23}$eV).
- ω_P - on the number of produced electron-hole pairs
- ω_C - on the collected charge
- ω_E -on the electronic noise

The component ω_P, due to the statistical variance in the number of the produced electron-hole pairs (given the Fano factor), is given by [67]:

$$\omega_\mathrm{p} = 2.355 \times \sqrt{(F \times E\epsilon)}, \tag{2.3}$$

where E is the energy of the γ rays in keV, and ϵ energy required to create one electron-hole pair (see Section 2.3). Thus, ω_P is an irreducible component of the detector's energy resolution.

Incomplete charge collection can also contribute to the width of the peaks in the energy spectrum by degrading the estimated energy of the events. The energy dependence of ω_C can be described by [67]: $\omega_C = cE$, derived from the subtraction of charge production uncertainty and electronic noise from the estimated energy resolution. The constant c is a proportionality term, estimated to be between 10^{-5} and 10^{-4} for germanium [67].

The contribution due to electronic noise can be divided into the series, parallel, and flicker components. The parallel noise is associated with the current flowing in the feedback circuit of the preamplifier. This type of noise can be due to the leakage current inside the detectors or thermal noise in the feedback resistor R$_f$. Mathematically parallel noise can be expressed as [67]:

$$\omega_\mathrm{E}^{parall} \propto \left(I_\mathrm{D} + \frac{2kT}{R_\mathrm{f}}\right) \times \tau_\mathrm{S}, \tag{2.4}$$

where I_D is the total current through the detector (induced by signal and leakage current), k is the Boltzmann's constant, T temperature of the feedback resistor, and τ_S is the shaping time of the preamplifier. As Eq. (2.4) illustrates, practically the parallel noise can be reduced by choosing the feedback resistor with higher R$_f$ and operating it in the cold.

The series noise is associated with the current in the series to the detector's signal, and its main contribution is due to capacitance of the detector and the detector-preamplifier connection as [67]:

$$\omega_\mathrm{E}^{series} \propto C^2 \left(\frac{2kT}{g_\mathrm{m} \times \tau_\mathrm{S}}\right), \tag{2.5}$$

where C is total readout circuit capacitance, including the detector, g_m is preamplifier's transconductance (~ 5mA/V in GERDA). To minimize the series noise, the lower detector's capacitance and lower operation temperature of the preamplifier is required. The smaller readout electrode of BEGe results in a lower capacitance with respect to the coaxial detectors (1 pf vs. 30 pf), and thus lower series noise, and a better energy resolution permitting enhanced background rejection based on the charge current distribution (see Section 2.5).

The last contribution to the electronic noise is a flicker noise, also called *1/f* noise, which is associated with variations in the direct current of all active devices. The flicker noise can be minimized by choosing the smallest capacitance for the feedback loop and detector. The total electronic noise is described by the combination of all three types:

$$\omega_{\mathrm{E}}^{2} = \left(\omega_{\mathrm{parallel}}\right)^{2} + \left(\omega_{\mathrm{series}}\right)^{2} + \left(\omega_{\mathrm{flicker}}\right)^{2} \tag{2.6}$$

Eq. (2.4) and Eq. (2.5) illustrate the conflicting dependency parallel and series noise on the shaping filter of the preamplifier. The optimum shaping filter is typically found so that the combination of both noise components is at a minimum.

The energy-dependent resolution of the γ peaks can be described by the combination of all the above variances (neglecting intrinsic one) as:

$$\mathrm{FWHM(E)} = 2.355\sqrt{\omega_{\mathrm{E}}^{2} + \epsilon \mathrm{F} \cdot \mathrm{E} + \mathrm{c}^{2} \cdot \mathrm{E}^{2}}. \tag{2.7}$$

As demonstrated in the above equation, the electronic noise term is an irreducible component of the energy resolution. The possible improvements of the energy resolution can be achieved by careful design of the electronic circuit and development of the dedicated shaping filters to filter out the noise contribution efficiently.

Energy Reconstruction of the Signals

The integral of the recorded signal is proportional to the energy of the initial event that induced the signal. To filter out the electronic noise, and correctly reconstruct the energy of the event, a signal shaping filter is applied to the waveform.

For the energy reconstruction in GERDA, two independent signal shaping filters are used. The most basic and robust is the pseudo-Gaussian filter, which is based on the moving window average (MWA) algorithm, as shown in Fig. 2.9. The pseudo-Gaussian filter is implemented via the following operations performed on the initial signal, as shown in Fig. 2.9. First, a delayed differentiation of the signal trace is performed. Then, a quasi-Gaussian shape signal is obtained from a series of 25 MWA operations. The number of MWA operations is chosen such that the shaped signal does not move out of the time window. The result of the applied Gauss filter is the signal with the removed high-frequency noise with a quasi-Gaussian shape, the height of which is proportional to the energy of the recorded interaction.

The second filter is the Zero Area Cusp (ZAC) filter. In comparison to the pseudo-Gaussian, it reduces low-frequency noise but requires additional optimizations of parameters for each detector after every calibration run. A detailed description of the ZAC filter can be found in Ref. [78], where the efficiency of this filter has been demonstrated. The shape of the filter is shown in Fig. 2.10, left. The filter consists of two sinh-curves on the left and right with a flat top function in between, the length of which is optimized to the charge collection time for each detector. The maximum of the convolution of the filter with the preamplifier signal is the energy estimator (see Fig. 2.10, right).

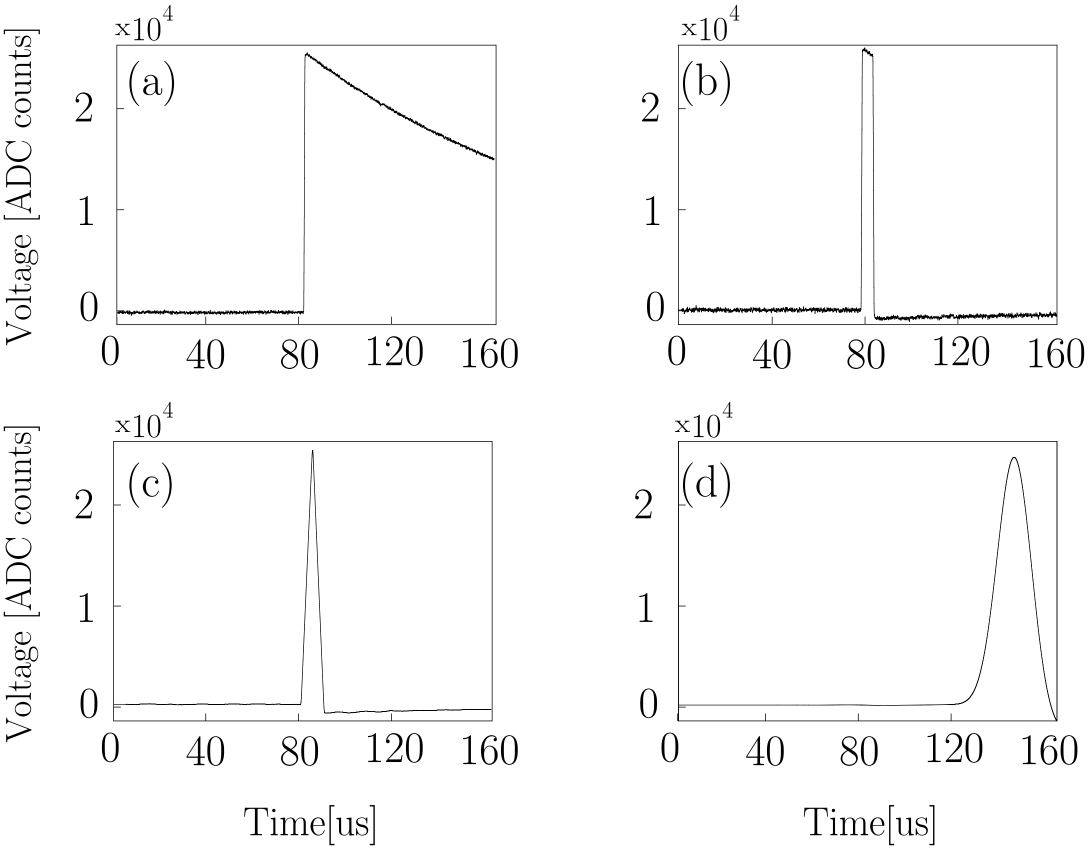

Figure 2.9: Step-by-step illustration of the pseudo-Gaussian filter. a, is the initial waveform; b, waveform differentiated with the time constant of 5μs; c, the waveform after the first moving average operation applied; d, the waveform after 25 operations applied. The figures adapted from Ref. [77].

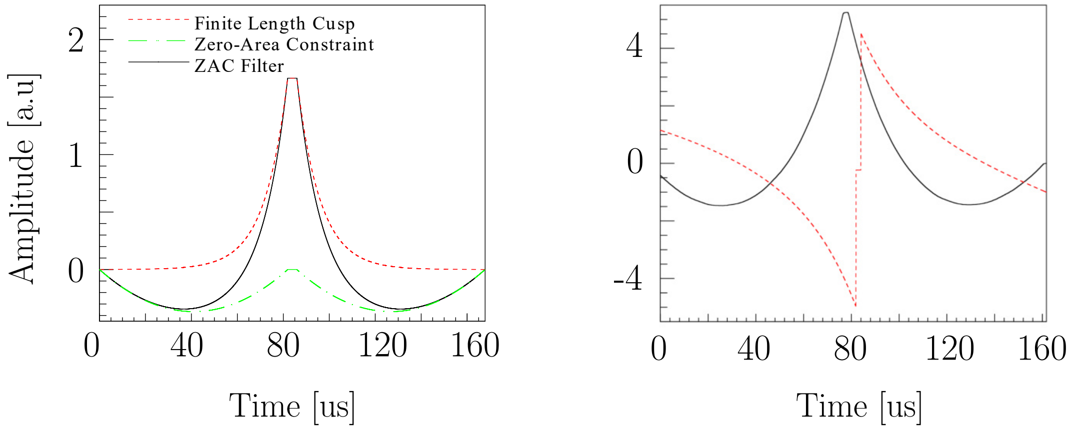

Figure 2.10: Left: The ZAC filter (red) consisting of Zero-Area constant function (green) and finite length cusp (black). Right: Inverse pre-amplifier response function (red) and result of its convolution with the ZAC filter (black solid). The figures are from Ref. [78].

These filters are used to reconstruct the initial energy, though in arbitrary units, depending on the energy filter used. The physical energy value of the event is estimated by applying calibration curves, as described in Chapter 3. The calibration curves define the relation between the energy in arbitrary units (a.u.) and physical value.

2.5 The $0\nu\beta\beta$ Decay Search in GERDA

As discussed in Chapter 1, the $0\nu\beta\beta$ decay is a rare process, and thus, the search for its signature requires maximum control of the background around $Q_{\beta\beta}$ and accurate data selection. The data selection for the $0\nu\beta\beta$ search is based on identifying and excluding background events, as well as excluding periods of data taking associated with instabilities in a particular detector's performance due to known reasons, such as hardware maintenance or seismic activities in the region of the LNGS laboratory. The data selection is based on monitoring the stability of the full energy peak in consecutive calibrations, as described in Chapter 3, as well as the leakage current of individual detectors. The following section presents results on the $0\nu\beta\beta$ search with the data collected between December 2015 and April 2018, and reconstructed with the ZAC estimator. Only the events acquired from the enriched detectors were included in the analysis; the dataset form the enriched coaxial detectors is referred to as Coax.

Events Selection

The energy deposition from the electrons emitted due to the $0\nu\beta\beta$ decay is expected to happen within a restricted volume of the detector fraction ($1\,\mathrm{mm}^3$). This type of event is called a single-site event (SSE). In contrast to SSE, background events are those with energy deposition within multiple locations around and in the detector array. The events with coincidental energy deposition in more than one detector within the time window of 1 ms are attributed to the background from ^{214}Bi and ^{214}Po of the ^{226}Ra decay chain, that is present in the materials surrounding the detectors.

Some of the external background events are tagged and rejected using the experiment's veto systems, described in Section 2.2. The data from the muon veto are consistently recorded every time the signals from at least 5 PMTs are above a threshold corresponding to 0.5 photoelectrons (p.e) peaks, or if signals from all three scintillator layers of the top muon veto are registered simultaneously. A signal from germanium detectors following the muon veto signal within a $10\,\mu$s window is attributed to a background muon event with the efficiency of 99%.

The data acquisition from the LAr veto is controlled by the germanium detectors' main trigger: the signals from the PMTs and SiPMs are recorded once the trigger is issued. The event in the germanium detector is tagged as a background if the signals from the LAr veto photosensors exceed pre-set thresholds. The critical time window and signal height thresholds for each PMT is adjusted according to its geometrical location in the LAr veto structure and its dark current rate – the rate at which events happen due to the thermal excitation of the electrons on its cathode. Typically, the time window between -0.8 and $6\,\mu$s with respect to the germanium detector signal used to tag events in coincidence. The threshold for the signal of the PMTs varies between 0.2 and 0.9 p.e.. The rate of accidental coincidences between the LAr and germanium detectors is cross-checked with the observation of the gamma line at 1461 keV due to ^{40}K decay happening in the LAr volume. Given that ^{40}K disintegrates via electron capture (EC) followed by the γ rays emission, no energy deposition in the LAr veto due to its decay is expected. Thus, all events with the energy of 1461 keV detected simultaneously in both, the LAr veto and germanium detectors, are due to random coincidences.

Another type of background events are those with a non-physical origin, e.g., the events

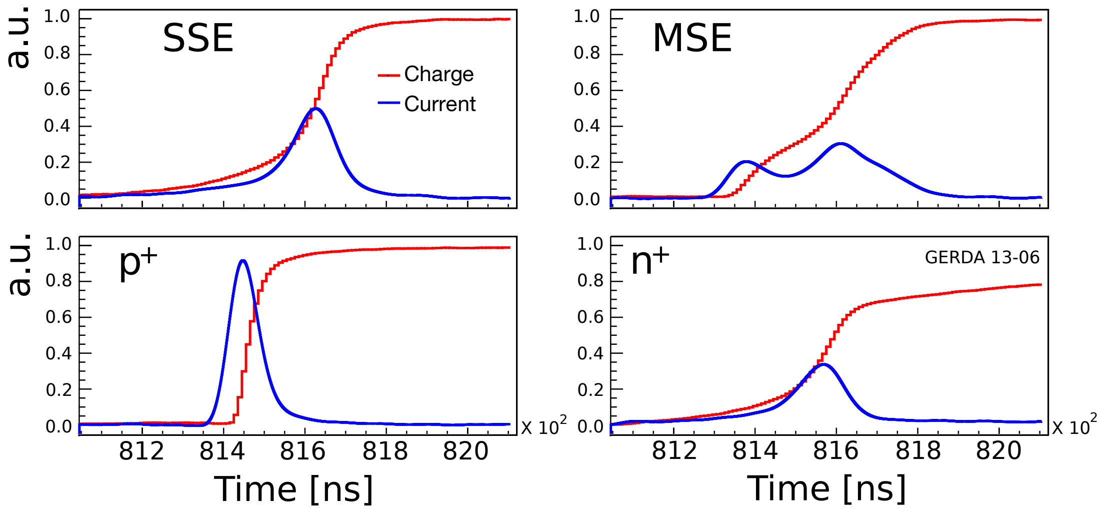

Figure 2.11: Examples of the charge and current distribution for various types of events of the same energy, with the charge, normalized to 1. By the shape of the charge and current pulses, the PSD algorithms identify signal-like events (SSE) from the background consisting of MSE, or events occurring close to the p^+ or n^+ electrodes. The figure is from Ref. [73].

Table 2.1: Efficiencies of the cuts used to select $0\nu\beta\beta$ decay events. The efficiency of the PSD for Coax is estimated as combination of MSE selection and rise-time cut efficiencies.

Technique	Efficiency
Muon veto	> 99.9%
LAr veto	(97.7±0.1)%
Quality cuts	99.9%
PSD BEGe	88%
PSD Coax	71.2%

whose waveforms contain only baseline or test pulse, or overlap with a waveform from another event (so-called "pile-up"). The origin of the pile-up waveforms is the long discharge tail of the feedback circuit (see Section 2.3). A dedicatedly developed set of cuts, called quality cuts, on the waveform's characteristics rejects those non-physical events with ~100% efficiency.

Important information corresponding to the topology of the events inside the detector is encoded in the waveform shape. Signal events, as previously mentioned, are SSE. Some of the backgrounds, such as those due to Compton scattering, occur with energy deposition in multiple locations inside the detectors and are called multi-site events (MSE). These MSE can be identified due to their pulse shape, using so-called pulse shape discrimination (PSD) techniques.

For the BEGe and coaxial detectors two different PSD techniques were developed. For the BEGe detectors, the PSD classifies SSE and MSE according to their maximum current to energy (A/E) ratio, as displayed in Fig. 2.11. Given that the energy of the event is proportional to the maximum of the charge distribution, the A/E ratio is extracted from the charge and current traces of the event.

The PSD for the coaxial detectors is based on training an artificial neural network (ANN) that uses supervised learning to discriminate waveforms due to SSE. To train the neural network,

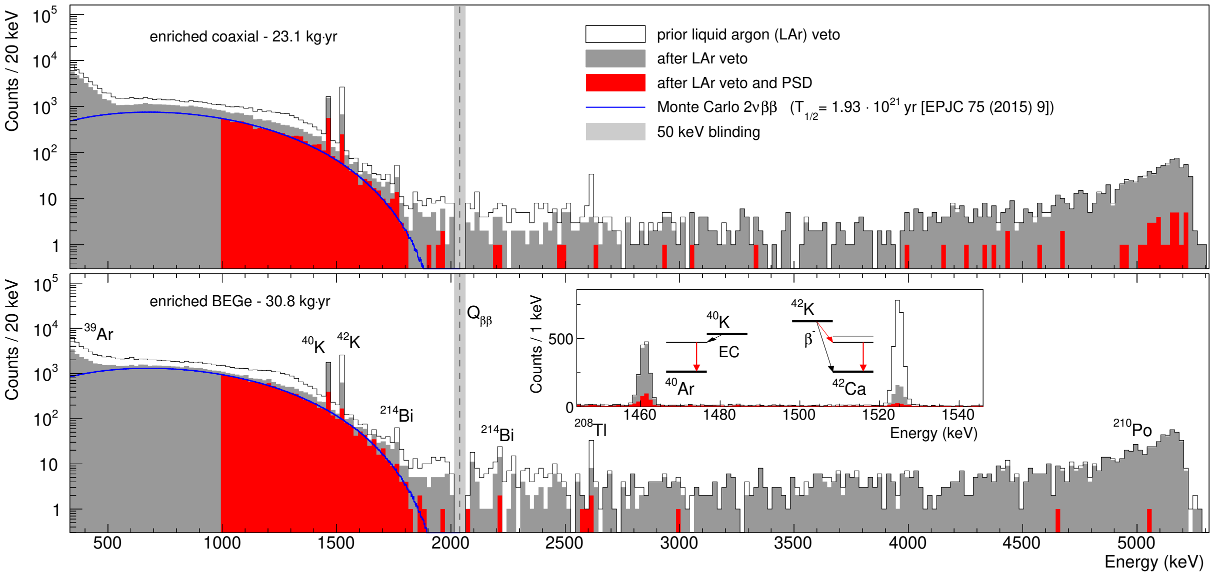

Figure 2.12: Collected spectra for Coax (top) and BEGe (bottom) datasets after applied cuts. The grey vertical bands indicate blinded energy region of $Q_{\beta\beta}\pm$ 25 keV. The blue solid lines indicate simulated $2\nu\beta\beta$ decay spectra for the half-life measured in Ref. [79]. Some background components are marked according to their origin. The insert depicts the energy distribution around the γ lines due to ^{40}K and ^{42}K decays.

known single-site events, such as Compton edge and double escape events from the calibration data are used. To remove the alpha events from the p$^+$ contact or groove of the coaxial detectors, an additional cut based on the signal risetime, i.e., the time the signal takes to rise from 10% to 90% of its maximum, was developed. The threshold for this cut is based on maximizing the acceptance of $2\nu\beta\beta$ events. Due to their smaller p$^+$ contact, the BEGe detectors suffer less from the α events, which are effectively removed by the PSD techniques.

The efficiencies of the individual cuts for the $0\nu\beta\beta$ events selection are summarized in Table 2.1, and the total efficiency in Table 2.2.

Statistical Analysis

The energy spectra from the data collected between December 2015 and April 2018 are shown in Fig. 2.12. To avoid introducing bias, the $0\nu\beta\beta$ decay search is based on a blind analysis (i.e., events with energy in the region of interest ($Q_{\beta\beta}$ ±25 keV) are stored separately during data collection and not available to the analysis). Before the final steps, a partial unblinding of 15 keV from the edges of the blinded window is performed to estimate the expected number of background events (BI) for the $0\nu\beta\beta$ decay.

After the data selection is finalized, the data in $Q_{\beta\beta}$±25 keV window is fully unblinded and further analyzed with two separate approaches: frequentist and Bayesian fits. The fit model includes a Gaussian centred at $Q_{\beta\beta}$ to describe the expected signal and a constant function to describe the background distribution. The fit is performed over the energy range between 1930 keV and 2190 keV, excluding the regions around the expected background lines 2104±5 keV and 2119±5 keV due to ^{208}Tl and ^{214}Bi decays, respectively.

The most recent result on the half-life of the ^{76}Ge $0\nu\beta\beta$ decay was extracted from the

Table 2.2: Summary of the analyzed datasets for the release of the $0\nu\beta\beta$ decay search results in the summer of 2018. The datasets differing by their expected background index (BI) were analyzed separately. The Phase I datasets are described in Ref. [80]. The table presents crucial parameters of the analysis such as exposure, FWHM, total efficiency of the applied cuts, BI, and the number of the observed events (N) in the unblinded region of $Q_{\beta\beta}\pm25$ keV.

Dataset	Exposure (kg·yr)	Energy resolution FWHM (keV)	Efficiency	BI 10^{-3} [cts/(keV·kg·yr)]	N [cts]
PhaseI-Golden	17.9	4.3(1)	0.57(3)	11 ± 2	46
PhaseI-Silver	1.3	4.3(1)	0.57(3)	30 ± 10	10
PhaseI-BEGe	2.4	2.7(2)	0.66(2)	5^{+4}_{-3}	3
PhaseI-Extra	1.9	4.2(2)	0.58(4)	5^{+4}_{-3}	2
PhaseII-Coax1	5.0	3.6(1)	0.52(4)	$3.5^{+2.1}_{-1.5}$	4
PhaseII-Coax2	23.1	3.6(1)	0.48(4)	$0.6^{+0.4}_{-0.3}$	3
PhaseII-BEGe	30.8	3.0(1)	0.60(2)	$0.6^{+0.4}_{-0.3}$	5

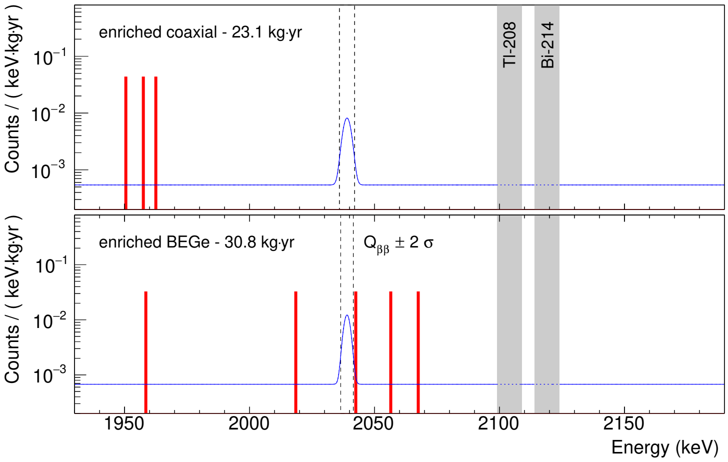

Figure 2.13: Unblinded energy region around the $Q_{\beta\beta}$ after all applied cuts for the Coax (top) and BEGe (bottom) datasets. The blue line shows the function corresponding to the hypothetical $0\nu\beta\beta$ decay signal with the half-life equals to the established 90% C.L. lower limit. Regions around the expected γ lines due to ^{208}Tl and ^{214}Bi are excluded from the analysis (shown with the vertical grey bands).

simultaneous fit of four datasets collected during Phase I and three datasets collected during Phase II. The Phase II data from the coaxial detectors were analyzed as two different datasets collected before and after summer 2017, when the new risetime cut to reject surface alpha events was introduced. Table 2.2 displays various parameters for each dataset, including collected exposure, estimated energy resolution at $Q_{\beta\beta}$, total efficiencies, expected background rate, and the number of the events found in the blinded region. For the latest data released in 2018, the GERDA experiment achieved the lowest background rate in the field, 10^{-4} cts/(kg·yr·keV), and remained an effectively background-free experiment, meaning that the expected number of background events for projected exposure is below one count within the range of one FWHM of the energy resolution at $Q_{\beta\beta}$.

The best fit value for the signal events is consistent between frequentist and Bayesian inferences and was estimated at zero counts. Thus, only a lower limit on the half-life of the $0\nu\beta\beta$ of

^{76}Ge was set, and the value of $T_{1/2} > 0.9 \cdot 10^{26}$ yr (90% C.L.) from the frequentist analysis was quoted. The results are shown in Fig. 2.13. Given the collected data and the expected background rate, the median sensitivity was estimated at $1.1 \cdot 10^{26}$ yr. The limit is slightly weaker than that, due to an observed event $2.4\,\sigma$ away from $Q_{\beta\beta}$ in the BEGe dataset, that is attributed to the background according to the fit results.

2.6 Prospects of GERDA

The end of the GERDA experiment is planned for the beginning of 2020, with the following decommissioning of the experimental setup. Until that, the experiment aims to collect more than 100 kg·yr of the total exposure and surpass the sensitivity of $1.4 \cdot 10^{26}$ yr to the $0\nu\beta\beta$ decay half-life, as demonstrated in Fig. 2.14. After the upgrade of the experimental setup, the collaboration plans to start the LEGEND experiment (see Section 1.7 in Chapter 1) in 2021, which aims to reach the ton-scale of the detector material, and explore the effective Majorana mass corresponding to the inverted ordering of the neutrino masses.

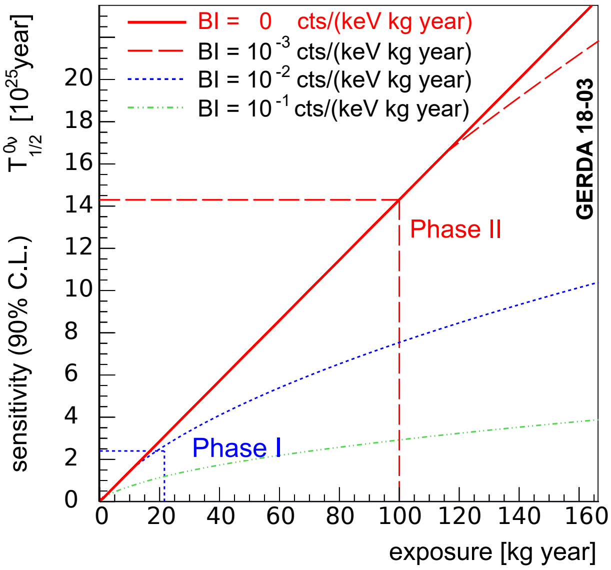

Figure 2.14: The sensitivity of GERDA to the $0\nu\beta\beta$ decay half-life according to the collected exposure and given effectively zero BI. As for the end of the Phase II, GERDA aims to remain effectively background-free experiment, and, collecting more 100 kg·yr of exposure, to overpass the sensitivity of $1.4 \cdot 10^{26}$ yr for the $0\nu\beta\beta$ decay half-life.

Chapter 3

Energy Calibration of GERDA

Due to the peak signature of $0\nu\beta\beta$ decay, the calibration of the energy scale and determination of the energy resolution are crucial for the $0\nu\beta\beta$ decay search. From the analysis of the calibration data, taken weekly with three ^{228}Th sources, the parameters for the energy calibration of the physics data are extracted. Additionally, the calibration is used to monitor the energy scale stability by checking the shifts in the position of the gamma peaks with the highest intensity. Finally, the energy resolution expected for the $0\nu\beta\beta$ decay signal is determined from the analysis of the calibration data for the enriched BEGe and coaxial detectors with the ZAC energy estimator, that is officially used for the $0\nu\beta\beta$ search analysis (see Chapter 2).

This chapter reports the results of the calibration data analysis from the first two years of GERDA Phase II until June 2017 and is organized as follows. Section 5.1 explains how the calibration data is taken, detailing hardware and calibration procedure. In Section 3.1 the implemented algorithms used to extract calibration parameters are summarized. Section 3.2 describes the routine analysis using an example of a typical calibration run taken after one year of the Phase II operation. Section 3.3 presents the data selection for the $0\nu\beta\beta$ analysis of the data collected between December 2015 and April 2017 based on the results extracted from the routine calibration analysis. The last section of the chapter, Section 3.4, presents the combined calibration analysis and the energy resolution estimated at $Q_{\beta\beta}$ for the $0\nu\beta\beta$ analysis.

3.1 Introduction

The calibration is a crucial part of the $0\nu\beta\beta$ analysis chain and has two primary purposes: to determine the energy scale for each detector and to determine the energy resolution. For the calibration process, the detectors are first exposed to ^{228}Th gamma sources. Then, the energy scale and resolution are determined using the well-known positions of the γ peaks in their energy spectra. As a final result, from the analysis of each calibration run, calibration curves, i.e., the functions that are used to express the energy estimator in terms of physical energy, for all detectors are extracted.

For the calibration of the germanium detectors, a source insertion system (SIS) was developed before GERDA Phase I [81]. The SIS is located on the top of the cryostat above the LAr level. The sources are kept on the top of the SIS during the physics data collection and lowered with the stainless steel bands to the detector level during the calibration. The location of the sources

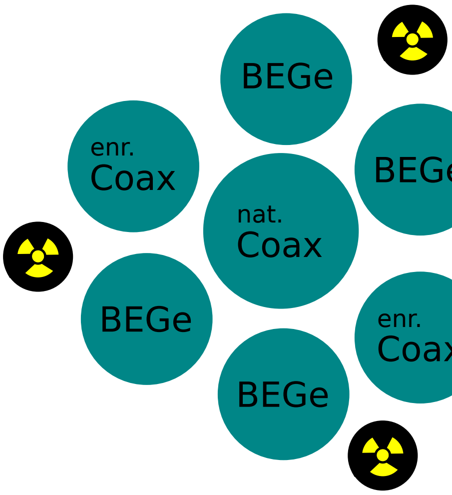

Figure 3.1: Location of the sources (marked with yellow and black) in the horizontal plane of the detector's strings. The detectors are arranged in the strings according to their type (BEGe/Coax, enriched in ^{76}Ge or with the natural abundance). The positions of the sources are chosen such that the most homogeneous exposure of the detectors is achieved.

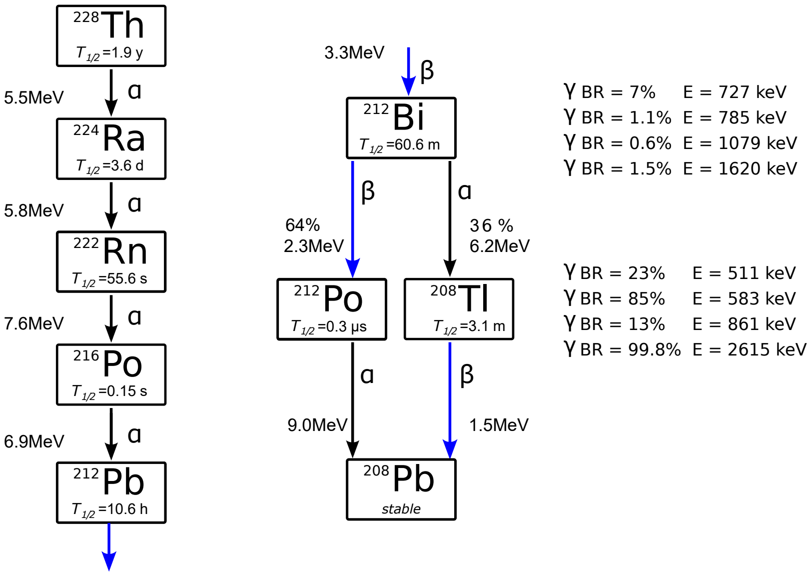

Figure 3.2: The decay series released in the ^{228}Th decay chain. The γ-rays with the highest BRs, that are visible in the calibration spectra, are from the β-decays of ^{212}Bi and ^{208}Tl. The Q-value and the BR (unless it is 100%) are indicated close to the decay mode. The decay scheme is adapted from [83].

relative to the horizontal plane of the detector's array is illustrated in Fig. 3.1.

The ^{228}Th calibration sources were produced before the beginning of the Phase II [82]. The ^{228}Th sources with activity between 20 and 40 kBq are sufficient to record energy spectra with γ peaks with enough intensity to calibrate the energy scale. For a typical calibration run between a few hundred and few thousands of events are acquired. The decay series from the ^{228}Th source is displayed in the Fig. 3.2. In the typical calibration spectrum, the strongest γ lines are due to β decays of ^{212}Bi (Q=2.2 MeV, $T_{1/2}$ =1 h) and ^{208}Tl (Q=5 MeV, $T_{1/2}$ =3 min).

The choice of the ^{228}Th source for the Gerda calibration is motivated by the broad energy

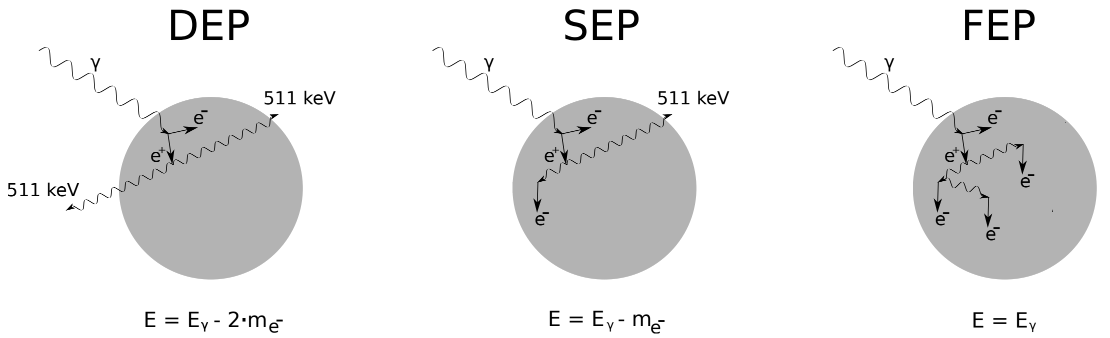

Figure 3.3: Possible interaction topologies for the 2.6 MeV γ within the detector material (shown as a grey area). Left: two created γ rays escape the detector volume, the absorbed energy results in the peak at 1592 keV (DEP). Middle: one γ escapes, carrying away 511 keV energy, resulting in the peak at 2103 keV (SEP). Right: the energy of the initial γ ray is fully absorbed.

range of the emitted gamma lines, that is sufficient to cover energies up to beyond the $Q_{\beta\beta}$ of ^{76}Ge at 2039 keV; the gamma peak with the highest intensity and energy is at 2.6 MeV. This range ensures precise interpolation of the energy resolution at the $Q_{\beta\beta}$ energy value. Importantly, the γ rays with an energy of 2.6 MeV emitted in the ^{208}Tl decay result in three peaks in the energy spectrum, corresponding to the different interaction topology inside the detectors shown in Fig. 3.3. Each of these peaks features properties that can be employed in the various steps of the analysis in GERDA.

The γ rays with the energy of 2.6 MeV undergo a e^+e^- pair production in the nuclear field. The created e^- deposits its energy in the detector's volume, while e^+ annihilates with another e^- from an atom's shell, producing two γ rays with the total energy of $2m_e^-$, where m_e^- is the rest mass of the electron. The γ's undergo Compton scattering, or with the lower probability photoelectric effect. If the energy of the initial γ is fully deposited in the detector volume, it will result in the Full Energy peak (FEP) visible at 2.6 MeV (as for initial γ). However, a γ may escape the detector's volume. If one of the two γ rays escapes, the total deposited energy in the detector would result in the peak at energy 2.6 MeV - m_e^-, which called Single Escape Peak (SEP). In case both γ rays escape, the total energy realized in the interaction corresponds to the peak at the energy of 2.6 MeV - $2{\cdot}\mathrm{m}_e^-$, and forms Double Escape Peak (DEP). Schematically all three cases are shown in Fig. 3.3 and identified in the spectrum shown in Fig. 3.4. Note, that even though the sum of the energies of the produced in the annihilation γ rays is equal to $2{\cdot}\mathrm{m}_e^-$, the energy of each of the γ is more likely to be slightly below or above m_e^- due to the fact that e^+ and e^- are unlikely to be at rest when they annihilate. This inequality of the energies would result in the broadening of the SEP toward the lower energies, i.e., Doppler broadening.

The topology responsible for the formation of DEP is similar to that expected from $0\nu\beta\beta$ decay of ^{76}Ge, i.e., two electrons deposit energy within $\sim$1mm^3 of the detector volume, and, therefore, these events form a class of SSE (see Chapter 2). A high-intensity DEP is an important property of the ^{228}Th source, which is used for training of the PSD algorithms, discussed in Chapter 2 and described in detail in Ref. [73]. The Full Energy Peak (FEP) at 2.6 MeV from the decay of ^{208}Tl has the highest intensity and can be used to monitor changes in the energy scale between the calibrations, which is necessary for data validation, i.e., selection of data with well defined and know energy scale.

Calibration Procedure

The calibration is performed manually by interrupting physics data taking and switching off all the PMTs to protect them from high event rate due to the source in the LAr. During the physics data taking, the sources are kept ~8 m above the array (above the LAr) and are lowered into the LAr cryostat one-by-one by the SIS system for the calibration. Each source is first lowered to the level corresponding to the bottom detectors in the array. After about 15 to 20 minutes, the source is moved to the level of the middle detectors and, finally, to the level of the top detectors. The position of the sources corresponds approximately to 8570, 8405, and 8220 mm below the initial position. The total duration of a calibration run is about 3 hours. The further processing is completed by the software handling the automatic data processing. The energy threshold during the calibration is set to about 400 keV to keep the event rate manageable for the data acquisition system.

Calibration Software

The online data reconstruction is performed as described in Chapter 2 with the Gauss filter. For the further noise rejection, particularly low-frequency noise, the ZAC filter is applied in the later stages of calibration data analysis flow, after parameters of the filter are optimized for each detector and each calibration run individually [78].

The parameters extracted from the waveforms of the calibration events are saved in ROOT [84] format. After the first step, in which the input configuration files with uncalibrated data are read, the quality cuts, detailed in [77] and discussed in Chapter 2, are applied to every event to remove non-physical events. These cuts examine the characteristics of the obtained waveforms and remove those that have more than one trigger or that originated from the test pulse, containing only the baseline counts or a distorted baseline, as well as pile-up waveforms.

A spectrum for each detector is obtained with the survived events. The spectra settings are chosen according to the following considerations. The binning of the spectra is set to roughly 0.3 keV below the resolution of all detectors at any given energy. The range of the spectra in a.u is set to the value corresponding to about 3000 keV, above the 2.6 MeV line. An example spectrum is shown in Fig. 3.4.

After the spectra with the selected events are prepared, an algorithm to search and identify peaks in the uncalibrated energy spectrum is executed. In this step, the peaks are identified according to the literature values [83]. The following instructions are implemented for the peak search and identification algorithms:

- Find all the peaks with heights above a given threshold relative to the highest peak in the spectrum, and the distance between the neighboring peaks at minimum $\sigma \approx 2$ keV. The peaks with heights below 5% of the highest peak are discarded as they are either from the background over-fluctuation, or have a low BR and, therefore, not sufficient for the calibration. This step is performed by utilizing the methods implemented in ROOT's TSpectrum [85] class.

- Among the saved positions of peaks in the spectrum from each detector, find the peak with the highest energy (in uncalibrated units, i.e., a.u.). Accordingly to the available data

Table 3.1: A naive classification of the peaks by their shape expected in the energy spectrum from the ^{228}Th source. The last column summarizes the fit model constructed for each type of the peaks.

Peak type	Energy [keV]	Fit model
Low stat.	785., 893, 1078, 1512, 1620	$g + f_{\text{lin}}$
High stat.	583, 727, 763, 860, 2615	$g + h + f_{\text{step}} + f_{\text{lin}}$
Doppler broadening	1592, 2103	$g + f_{\text{step}} + f_{\text{lin}}$

on the ^{228}Th , the peak with a BR above 90% is the FEP due to ^{208}Tl decay at the energy of 2.6 MeV.

- Perform the approximate calibration using the position of the 2.6 MeV. In this step, the calibration function is estimated in the naive way as $\text{E}_0(\text{E'}) = \text{k}\cdot\text{E'}$, where

$$k = \frac{E'(E = 2.6\,\text{MeV})}{2.6\,\text{MeV}}.$$

  The following steps make the calibration more precise by using the information from the identified γ peaks calibrated with the preliminary calibration function.

- From the preliminarily calibrated spectrum, check the position of each peak in keV units on its correspondence to each of the peaks from the literature values. Given the uncertainties of the rough calibration curve, only rough correspondence to the literature values is expected and for attributing a peak to one of the γ rays expected from the decay of ^{228}Th its energy has to agree within 1%:

$$\left|\frac{\text{E}_{\text{a.u.}}}{\text{E}_{\text{keV}}} - 1\right| < 0.01,$$

  where E(a.u.) is the position of the examined peak from the spectrum in the arbitrary units, E(keV) is the energy value of the corresponding γ line found in the literature values. The peak is then assigned to the literature value if the above condition is met.

To determine the peak position precisely, a model function is fit locally to the peaks. The typical calibration spectrum features three types of peaks, according to the BR of the emitted γ rays and interaction topology in the detector: low and high statistics peaks, and escape peaks. The low and high statistics peaks are those that typically contain below and above 500 events, respectively.

The fit of the peaks is constructed such as to account for artifacts of the energy spectra. Each γ peak is fit at minimum with a Gaussian function, g, to account for the signal shape and a linear function, f_{lin} to fit the linear background distribution, defined as:

$$g(E|\mathcal{N}, \mu, \sigma) = \frac{\mathcal{N}}{\sqrt{2\pi}\sigma} \exp\left(-\frac{(E-\mu)^2}{2\sigma^2}\right) \tag{3.1}$$

$$f_{\text{lin}}(E|a, b, \mu) = a + b \cdot (E - \mu), \tag{3.2}$$

where μ, σ, and $\mathcal{N}$ are position, resolution, and intensity of the fitted peak, a and b are the slope and offset of the linear background distribution.

If the peak is expected to have high statistics or to be affected by Doppler broadening, a step function is added to the fit model to account for the events with the lower energy:

$$f_{\text{step}}(E|\mu, \sigma, d) = \frac{d}{2} \operatorname{erfc}\left(\frac{E-\mu}{\sqrt{2}\sigma}\right), \tag{3.3}$$

where d is the height of the step function. In addition, for the high statistics peaks a low energy tail is added to model the artifacts caused by the charge collection time bigger than the shaping time of the filter, called "ballistic deficit":

$$h(E|\mu, \sigma, c, \beta) = \frac{c}{2\beta} \exp\left(\frac{E-\mu}{\beta} + \frac{\sigma^2}{2\beta^2}\right) \operatorname{erfc}\left(\frac{E-\mu}{\sqrt{2}\sigma} + \frac{\sigma}{\sqrt{2}\beta}\right), \tag{3.4}$$

where c and β are the height and slope of the tail.

The three types of the γ peaks are summarized in Table 3.1. As it can be seen, all the peaks due to ^{208}Tl decay are attributed to the high statistics or Doppler broaded peaks. In addition the peak at 727 keV from ^{212}Bi decay is expected to have high statistics, while other peaks from the ^{212}Bi decay are categorized as a low statistic.

The goodness of the fit for each peak is verified by the following criteria. First, the estimated from the FWHM is required to be above 1.5 keV and below 11 keV. Second, the estimated amplitude of the peak is required to be at least 2.5 times higher than the estimated background height. Moreover, the error of the FWHM must be less than the value of the FWHM itself. If at least one of the conditions failed, the peak is considered as false-identified, and it is erased from the following steps, most importantly from the computation of the calibration curve.

From the fit of each identified peak, the values of the position and resolution as the mean and sigma of the Gaussian component are extracted. The position values of the peaks extracted from the spectrum and the physics energy values attributed to them are fitted with a linear function defined as follows:

$$E_{\text{cal}}\left(E_{\text{a.u.}}\right) = p_0 + p_1 \cdot E_{\text{a.u.}} \tag{3.5}$$

This relation is used to convert the energy estimator into physically meaningful units and the energy spectra this way are used for further analysis. The FWHM of the identified peaks is calculated in keV and plotted versus the identified physical energy values of the peaks to form the resolution graph. Given that the resolution of the SEP and DEP is affected by Doppler broadening, it is excluded from the resolution graph. The fit of the resolution graph is performed by the following function:

$$\text{FWHM(E)} = 2.355\sqrt{\text{a}^2 + \text{b}^2 \cdot \text{E}}, \tag{3.6}$$

describing the uncertainties due to electronic noise and pair production process (see Chapter 2). The parameters of the calibration and resolution curves are estimated with a χ^2 fit of the extracted data. The fits are performed with the Minuit2 algorithm with Minos error estimation [86] implemented in the ROOT framework. Additionally, the estimated position of FEP is compared to the value extracted from the previous calibration run for the energy scale stability monitoring. For the two consequent calibration runs with the numbers i-1 and i the shift S in

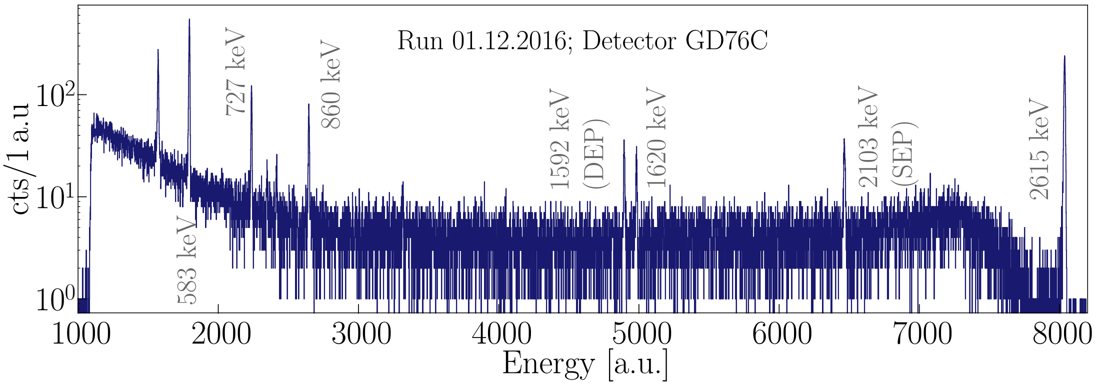

Figure 3.4: Uncalibrated energy spectrum for a BEGe detector GD76C from the third calibration of Phase II, taken on 1st of December 2016. The values in a.u. are reconstructed with the Gauss energy estimator. In the presented spectrum, eight γ peaks were used to extract the calibration curve.

the FEP is estimated as follows:

$$S = (E_i^{a.u} - E_{i-1}^{a.u}) \cdot \frac{2614.5}{E_i^{a.u}}, \tag{3.7}$$

where S is estimated in keV units and indicates the changes in the detectors' gain.

3.2 Analysis of the Weekly Calibration Data

After calibration data is taken, and the dataset with the energy estimator values is produced, the routine calibration analysis is performed. For each calibration, the analysis procedure is typically run twice: once for the Gauss and once for the ZAC energy estimators. As mentioned in Chapter 2, the parameters for the ZAC filter, which efficiently suppresses the effects of low-frequency noise, require additional run-by-run optimization and computation; hence, the ZAC estimator is analyzed in a second iteration. The parameters for the Gauss estimator, however, do not change from run to run, and, therefore, it is used to extract information on the system's stability and energy resolution right after the calibration data is taken. The section below describes the routine calibration analysis on the example of the Gauss energy estimator, which is similar to that was performed for ZAC as well. In total, 47 calibrations runs were taken between December 2015 and April 2017 and analyzed in the framework of this work.

For a typical calibration, about $5{\cdot}10^4$ to $1.5{\cdot}10^5$ events for BEGe and between $1{\cdot}10^5$ and $3{\cdot}10^5$ events for coaxial detectors are acquired. The smaller collected statistics obtained for the BEGe detectors is due to their smaller size relative to coaxial detectors. A typical uncalibrated energy spectrum obtained with the Gauss estimator for one of the BEGe detectors is displayed in Fig. 3.4. The presented calibration was taken on the 1st of December 2016, after one year of the Phase II data-taking, and reflects one of the typical cases. For the example spectrum presented in Fig. 3.4, the fits of the peaks, that passed the selection criteria described in Section 3.1, are presented in Fig. 3.5. For a typical calibration spectrum, 4-8 peaks can be identified and successfully fit.

The calibration and resolution functions extracted from the example spectrum (see Fig. 3.4)

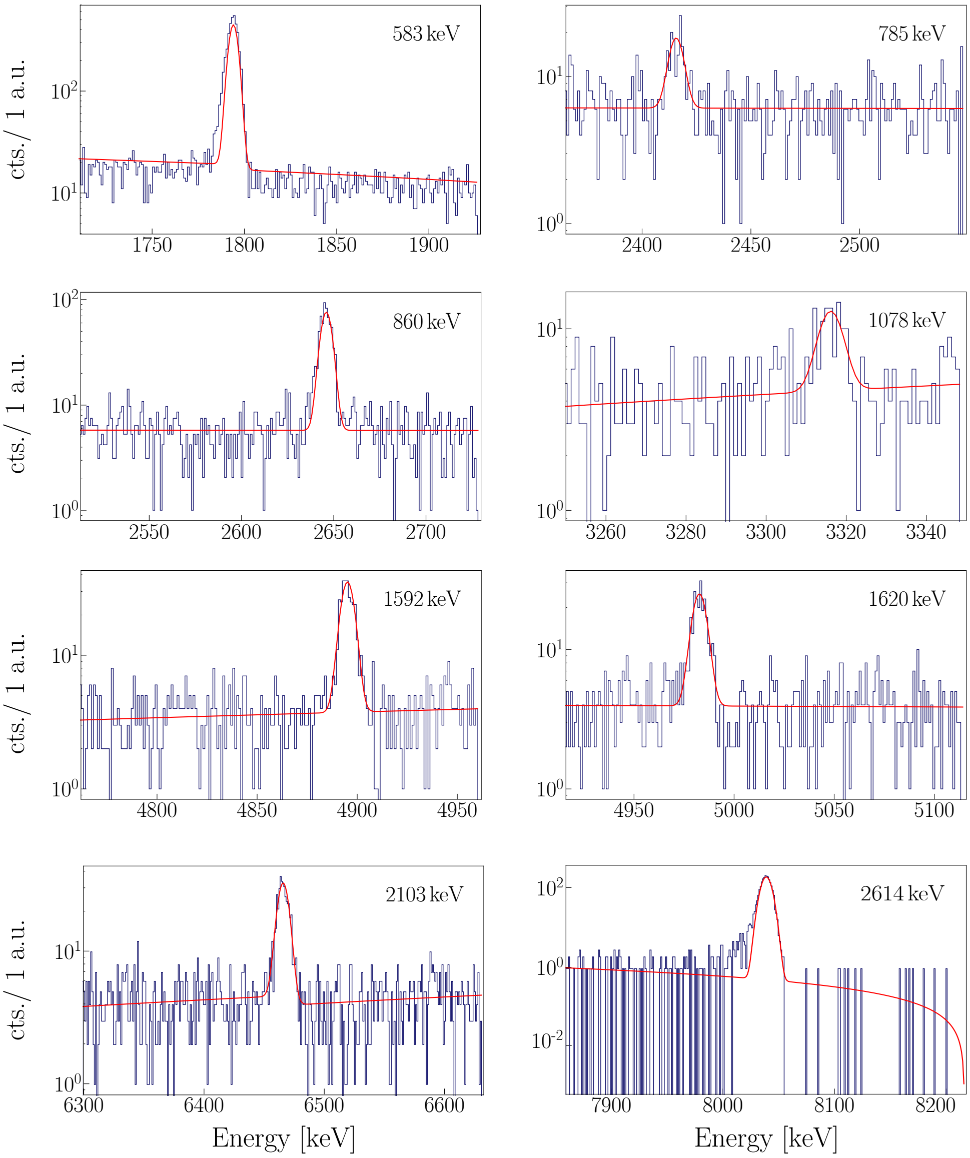

Figure 3.5: Fit of the peaks that have passed all the selection criteria and were used to extract the calibration curve for the example spectrum shown in Fig. 3.4. Each peak was fit with the function corresponding to its type (see Table 3.1). The peaks at energies 785 keV, 1078 keV and 1620 keV were fit a Gaussian function and linear background. For the fit of the peak at energies of 1592 keV and 2103 keV an additional step function was added. For the fit of the peaks at energies of 583 keV, 860 keV, and 2615 keV an additional function to model the incomplete charge collection was added.

are provided in Fig. 3.6. Typically, the extracted calibration curves were applied to all recorded events until the next calibration run. However, if instabilities in the detector's system prior to the analyzed calibration data are observed, the calibration curves were applied retroactively from the moment those instabilities occurred.

Once the γ peaks and calibration function are extracted from the spectrum, the changes in the energy scale, in comparison to the previous calibration, are estimated. The shift of the 2.6 MeV line between every two calibrations is used to monitor the stability of the detector's energy scale. Thus, for each detector, a position of the 2.6 MeV in the a.u. is compared to the previous

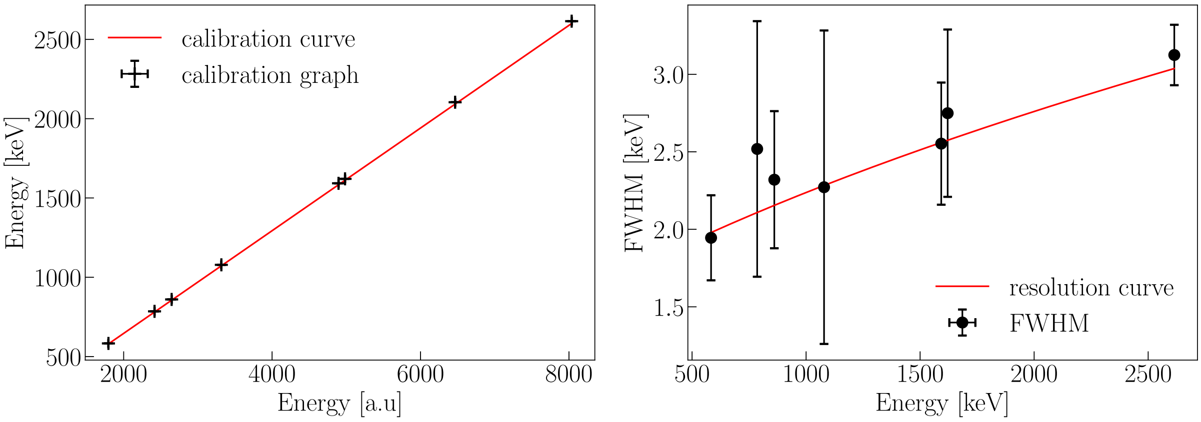

Figure 3.6: The calibration (left) and resolution (right) functions extracted from the analysis of the spectrum presented in Fig. 3.4. The curves are obtained with the χ^2 fit. The calibration curve is fit to the obtained positions of the identified peaks in a.u. and physical energy in keV. The resolution curve is fit to the estimated peak's widths versus energy (in keV).

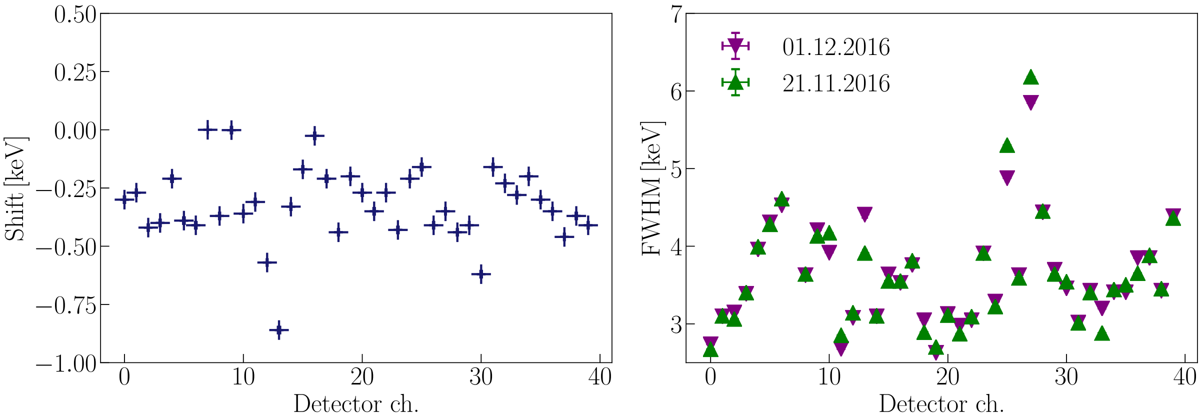

Figure 3.7: Changes in the position (left) and FWHM (right) of the 2.6 MeV line between two calibrations taken on 21st November and 1st of December 2016 for all detectors. The detectors operated in AC mode are excluded from the figures.

calibration run, and the shift is recalculated to the keV values to determine the changes in the detectors' energy scale. If the shift is higher than the value of one resolution in FWHM, a more detailed check is performed. If the shift in the energy scale occurred between two calibrations within a short time, the extracted calibration curves are applied retroactively starting from the moment of the shift. If the detector performance is continuously unstable over time between the calibrations, resulting in the shift of the 2.6 MeV line on the order of its FWHM, the events collected from these detectors are excluded from the physics dataset, and the detector is used only in anti-coincidence (AC) mode, (i.e., to tag the events that coincide with other detectors).

Fig. 3.7 demonstrates the estimated values for shifts and FWHM for the calibrations taken on the 21st of November and the 1st of December 2016. For the presented calibration run, in total, two detectors out of 40 were set to AC-mode.

A complementary way to monitor the system's stability is by monitoring the stability of the test pulses injected into the electronic's front-end board every 20 s through the entire period of the data collection [63].

Table 3.2: Calibration runs (indicated by the date dd.mm.yy) corresponding to the external interruptions of the detector performance.

Date	Hardware interruption
03.02.16	Modifications of the applied HV
18.02.16 and 19.02.16	Changes in the detector's gain caused by source movements
01.03.16	Tests pulser jump
07.03.16	Hardware work on PMTs
04.04.16	Test on the preamplifiers
12.04.16	HV filters exchange
29.04.16	Power failure
17.05.16	Calibration with the low activity source
17.06.16	Problems with the muon veto
06.07.16	Absence of the test pulse
29.09.16	Exchange of the signal cables

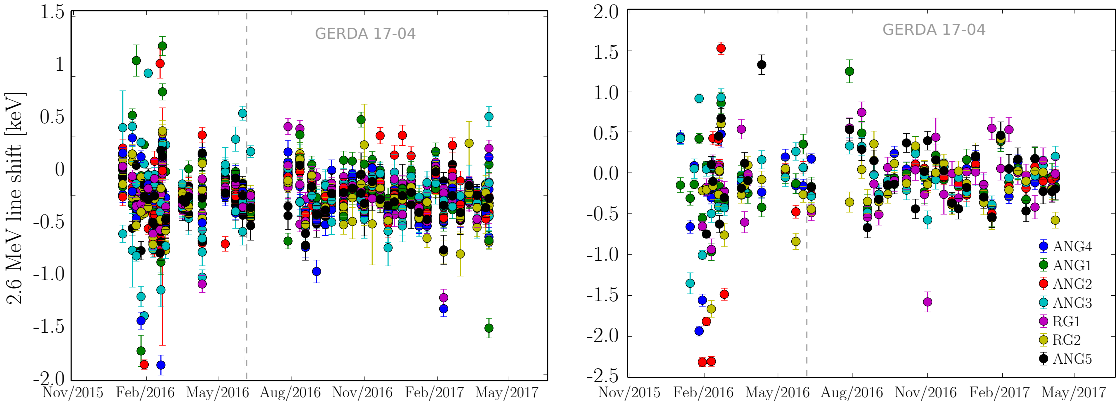

Figure 3.8: Relative shifts of the 2.6 MeV line for detectors from the BEGe (left) and Coax (right) datasets, estimated from the analysis of the calibration runs acquired between December 2015 and April 2017. For clarity, the legend for 30 BEGe detectors is not shown on the plot. The vertical dashed line separates the calibrations included in the first data release, in the summer of 2016 [65].

3.3 Data Selection for the $0\nu\beta\beta$ Analysis

The stability of the 2.6 MeV line across the calibrations taken over long periods is an effective representation of the stability of the detector's performance during the physics data collection. The selection of stable periods of the data collection is a compromise between reduced exposure and preservation of the detectors' excellent energy resolution.

By monitoring the shifts of the 2.6 MeV line in the uncalibrated Gauss energy spectrum between every two calibrations, only stable periods of data collection between December 2015 and April 2017 were selected for the $0\nu\beta\beta$ analysis. If the shift of the 2.6 MeV exceeds its FWHM, the data collected from the detector was excluded from the corresponding collection period, and the detector was operated only in AC mode.

Additionally, one detector was entirely excluded from the $0\nu\beta\beta$ dataset due to uncertainties in its active volume and were used in the AC mode. This detector is GD02D (channel 6). Fig. 3.8

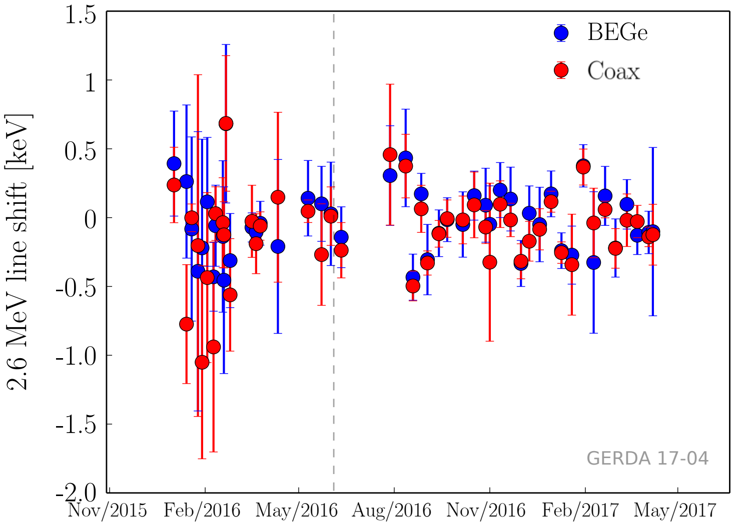

Figure 3.9: The detectors performance in terms of the 2.6 MeV line stability, averaged over each dataset. The data point for each calibration is a mean value over the dataset, while the error bars are for the RMS of the shifts within one calibration. The vertical dashed line indicates the data release in the summer of 2016.

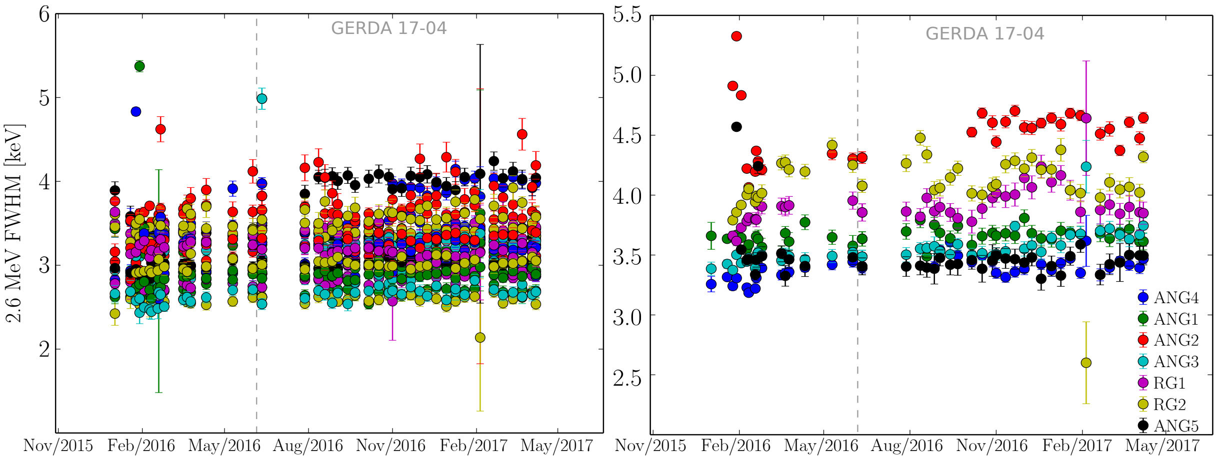

Figure 3.10: As for Fig. 3.8 for stability of the detector's energy resolution (FWHM).

displays the relevant shifts of the 2.6MeV line position between every two successful calibrations. The calibrations that were taken after some hardware interruptions, maintenance work in the clean room or test pulse problems, as listed in Table 3.2, were excluded; detectors operated in the AC mode were excluded as well. As Fig. 3.8 illustrates, the stability of the detector's energy scale improved starting from the summer of 2016. This improvement is a significant achievement in the expertise of the detector's handling and fewer hardware interruptions.

The average performance in terms of the 2.6 MeV lines stability over time for BEGe and Coax datasets, is shown in Fig. 3.9, where the average shift for one calibration is estimated as the mean of all shifts among one dataset (BEGe, Coax) with a standard deviation as an error. The estimated mean (RMS) value is -0.01 keV(0.3 keV) and 0.06 keV(0.2 keV) for BEGe and for Coax, respectively.

Furthermore, the stability of the detectors' resolution was checked for the energy reconstructed with the ZAC estimator. Fig. 3.10 depicts the FWHM of the individual detectors for the

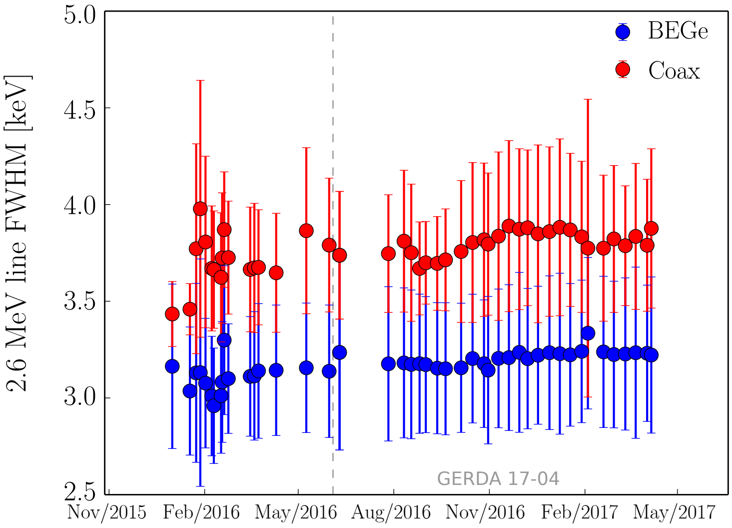

Figure 3.11: Mean FWHM of BEGe (blue) and Coax (red) datasets. The data point for each individual calibration is a mean FWHM of the dataset, while the error bars are for the RMS of the FWHM within one calibration, depicting the spread of the values in one dataset.

BEGe and Coax datasets, while Fig. 3.11 presents the average performance of each dataset. The average FWHM of the 2.6 MeV line for the BEGe and Coax estimated with ZAC filter is (3.17 ± 0.37) keV and (3.76 ± 0.36) keV, respectively; the errors indicate the RMS over the detectors.

As described above, the detectors' stability was monitored, defining the analysis dataset for the $0\nu\beta\beta$ search. In the next step, the combined calibration analysis of the selected calibration data was performed to evaluate the FWHM at $Q_{\beta\beta}$.

3.4 Energy Resolution for the $0\nu\beta\beta$ Search

In the physics analysis for the half-life of the $0\nu\beta\beta$ decay, the energy resolution in the region of interest is a critical parameter (see Chapter 1). This section describes the results and procedure applied to the data collected between December 2015 and April 2017 to evaluate effective energy resolution at $Q_{\beta\beta}$ for the $0\nu\beta\beta$ analysis presented in Ref. [87]. From the combined calibration data of all successful calibrations, the resolution at $Q_{\beta\beta}$ was estimated for enriched BEGe and coaxial detectors. The latter is referred to as Coax dataset to distinguish it from the coaxial detectors with the natural abundance of ^{76}Ge that are not included in the $0\nu\beta\beta$ decay search analysis. The employed procedure is similar to that used for the Phase I [77].

The energy resolution at $Q_{\beta\beta}$ was estimated from the analysis of the combined calibration data from all successful calibrations, excluding those summarized in Table 3.2.

The selection of calibration runs for the combined dataset was completed over a long period with routine monitoring of the detector's performance (see Section 3.3). In total, 35 calibrations were combined for this analysis.

Once the successful calibrations were selected, the combined dataset was constructed from the energy reconstructed with the ZAC estimator, the estimator used for the $0\nu\beta\beta$ analysis (see Chapter 2). Given that the parameters of the ZAC filter are optimized run-by-run, uncalibrated spectra for each detector across different calibrations differ significantly. To obtain the spectrum in which the energy resolution is representative of the full dataset taken over the period

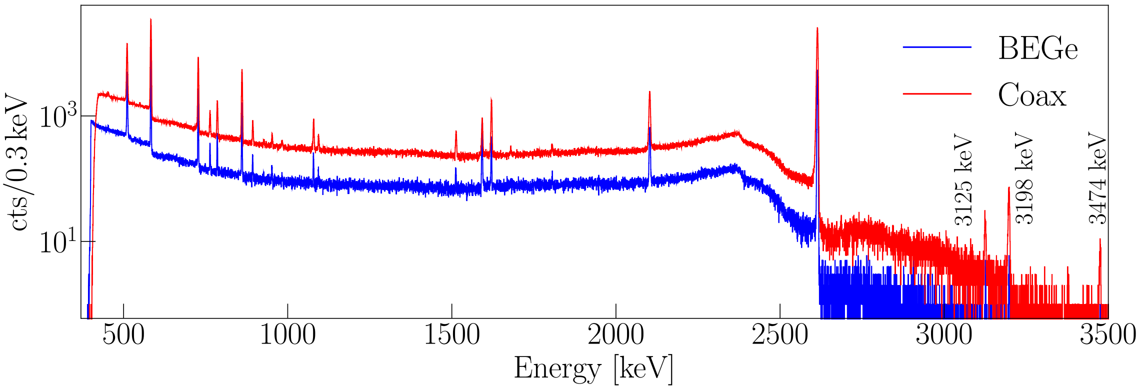

Figure 3.12: Combined calibrated spectra for BEGe (blue) and Coax (red) from the combined calibration dataset. Given the high statistics of the combined dataset, the summation peaks at 3125 keV, 3198 keV, and 3474 keV are visible as well.

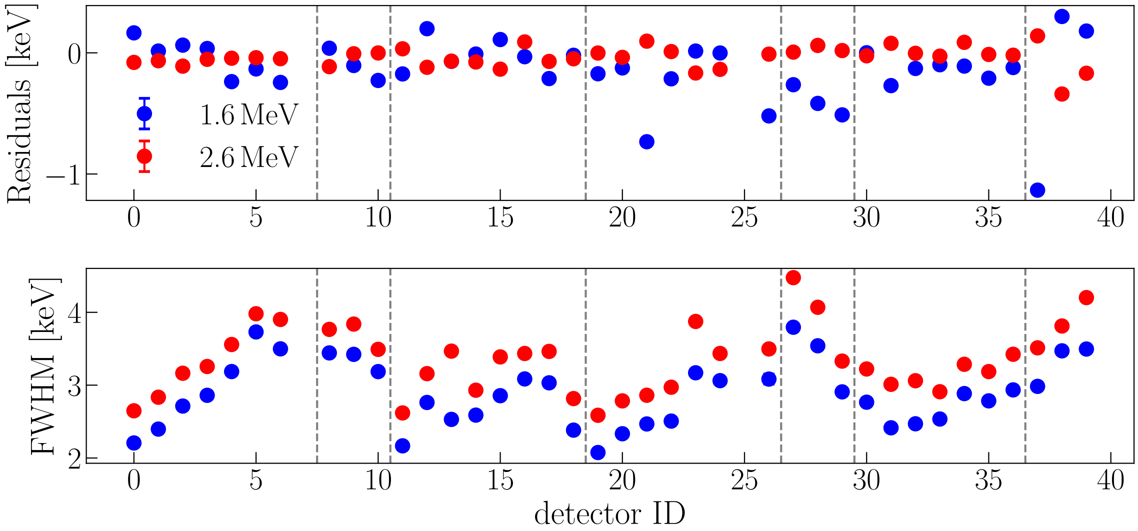

Figure 3.13: Residuals from the literature values (top) and FWHM (bottom) of the 2.6 MeV and 1.6 MeV lines estimated detector-wise from the combined calibration dataset. The vertical dashed lines separate the values for the detectors from the different strings.

of two years, all calibration spectra during that time are added applying the energy calibration, so their energy scales are consistent.

To estimate energy resolution curves and deviation of the γ peaks positions from the literature values in the combined spectrum, the routine calibration analysis was performed on the combined calibration spectrum for each detector separately. Fig. 3.13 presents the estimated values detector-wise for 2615 keV line and 1620 keV lines. The figure clearly illustrates that the detectors with a higher number in one string tend to have worse energy resolution, which can be partially explained by the longer signal cables (see the structure of the detector array in Chapter 2).

To obtain the effective energy resolutions of the γ line at energy E_j for a dataset, the energy resolutions of this line from each detector from the corresponding dataset were weighted with the exposure as follows:

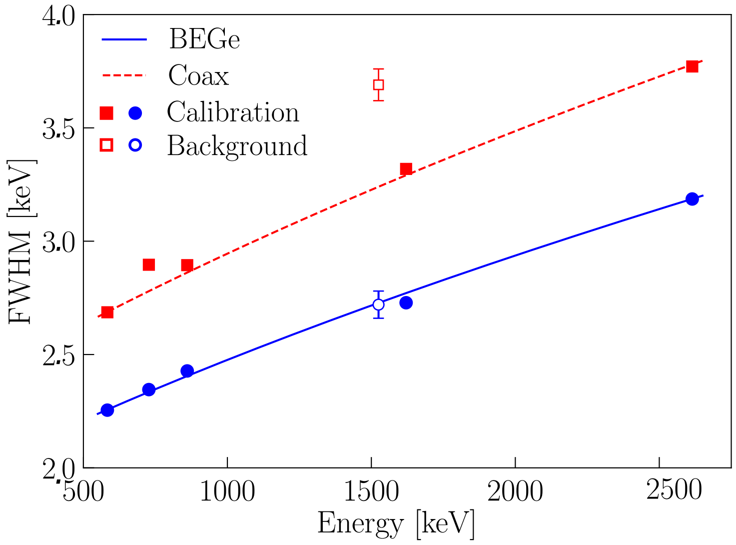

Figure 3.14: Mean energy resolution graph for BEGe (blue) and Coax (red) with the respective best-fit functions, that are used to interpolate the FWHM at $Q_{\beta\beta}$. An additional correction on the FWHM at $Q_{\beta\beta}$ for the Coax is applied according to the FWHM estimated from the fit of background γ line at 1525 keV due to ^{42}K decay (shown with empty markers).

$$FWHM(E_j) = \sum_{i=0}^{N_{\text{det}}} \frac{FWHM(E_j)_i \cdot T_i}{\sum_i T_i} \tag{3.8}$$

$$S_{FWHM(E_j)} = \sqrt{\sum_{i=0} \left(\frac{T_i}{\sum T_i}\right)^2 \cdot S^2_{FWHM(E_j)_i}} \tag{3.9}$$

where i runs over the detectors from one dataset containing in total N_{det}. The exposure of each detector (T_i), collected between December 2015 and April 2017, used for the weighting are summarized in Chapter A.

To estimate the FWHM at $Q_{\beta\beta}$ only the peaks with sufficient statistics were selected, which are 583 keV, 860.53 keV, and 2615 keV from the decay of ^{208}Tl and 727 keV and 1621 keV from the decay of ^{212}Bi. The obtained values on the energy resolution of the gamma peaks for each dataset were then fitted with an energy-dependent function:

$$FWHM(E) = 2.355 \cdot \sqrt{a + b \cdot E}. \tag{3.10}$$

The best fits for BEGe and Coax dataset are provided in Fig. 3.14, and the best parameters of the resolution curve are presented in Table 3.3. From the interpolation of the resolution curves, the estimated FWHM at $Q_{\beta\beta}$ is 2.9 keV and 3.5 keV with negligible uncertainties from the fit function for the BEGe and Coax, respectively.

To account for the effect of the long-term data collection on the detectors' resolutions such as instabilities in the readout channels between the calibrations, additional corrections were applied to the energy resolution. For this correction the background γ line at 1525 keV from the ^{42}K decay, which has the highest intensity in the physics spectrum, was used. The resolution of the γ line was estimated with Bayesian fit. The fit was performed with a Gaussian function for the γ peak and constant background. The uniform priors on the parameters are provided; the

Table 3.3: Summary of the parameters for the mean resolution curve (Eq. (3.10)): best fit values for a and b, their errors S_a and S_b, FWHM at 1525 keV estimated from the fit of the γ line from the ^{42}K decay, and its difference (denoted here as C) with the FWHM evaluated from the resolution curve.

	$FWHM(E) = 2.355 \cdot \sqrt{a + b \cdot E}$					
Dataset	a	b	S_a	S_b	$FWHM_{^{42}K}$	C
BEGe	0.65	$4.4{\cdot}10^{-4}$	$1.9{\cdot}10^{-4}$	$1.2{\cdot}10^{-7}$	2.72±0.06 keV	-0.008
Coax	0.9	$0.6 \cdot 10^{-4}$	$6.8{\cdot}10^{-5}$	$2.8{\cdot}10^{-8}$	3.65±0.08 keV	0.4

prior function on the peak position is defined over the range as (1525±10) keV; on the FWHM, the prior is defined between 0 and 10 keV. The results of the fit are presented in Fig. 3.15. The estimated FWHM is (2.72±0.06) keV and (3.65±0.08) keV for BEGe and Coax, respectively. The correction term, C, on the energy resolution at $Q_{\beta\beta}$ was estimated as the difference of the FWHM at 1525 keV interpolated from the fit function and estimated from the fit of the γ line:

$$C = FWHM^{phy}_{^{42}K} - FWHM^{cal}_{1525}. \tag{3.11}$$

The corrections of -0.008±0.06 and 0.4±0.08 were estimated for BEGe and Coax, respectively; the errors were estimated from the sum of the quadratures of each term in the above equation. Given that estimations of FWHM at 1525 keV from the interpolation of the resolution curve and fit of the background line for BEGe were consistent within the statistical uncertainties, only corrections to the Coax dataset were applied.

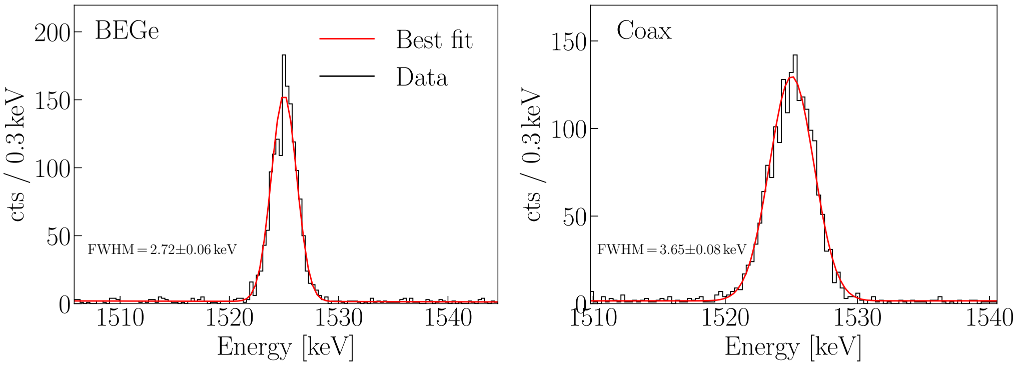

Figure 3.15: The fits of the background γ line at 1525 keV from the decay of ^{42}K. The estimated FWHM values were used to correct the energy resolution at $Q_{\beta\beta}$ estimated from the resolution curves.

The final values for the FWHM at $Q_{\beta\beta}$ and its uncertainty were estimated as follows:

$$FWHM_{Q_{\beta\beta}} = FWHM^{cal}_{Q_{\beta\beta}} + C \tag{3.12}$$

$$S_{FWHM_{Q_{\beta\beta}}} = 2.355 \cdot \sqrt{\frac{1}{4FWHM_{Q_{\beta\beta}}} \cdot (S_a^2 + E^2 \cdot S_b^2) + S_C^2}, \tag{3.13}$$

where S_C^2 is the error on the correction term (applied only for the Coax dataset), and S_a and S_b are the errors on the resolution function estimated from the χ^2 fit. For the Phase II data, the resolution of (2.95±0.06) keV and (3.9±0.1) keV at $Q_{\beta\beta}$ energy was estimated for the enriched BEGe and coaxial detectors.

The resolution curves estimated from the combined dataset were used to obtain and optimize parameters for the PSD algorithms (described in Chapter 2), and for the smearing of the Monte Carlo spectra of the global background model (for more discussion about the background model see Chapter 4). The estimated FWHM at $Q_{\beta\beta}$ was included in the $0\nu\beta\beta$ analysis described in Chapter 2 and in Ref. [87].

3.5 Conclusion

The energy calibration is a crucial part of the data analysis in GERDA. It defines the energy scale of all recorded events and is the basic for the $0\nu\beta\beta$ search. In GERDA, the calibration is performed by exposing the detectors to ^{228}Th sources on a weekly basis. The extracted calibration curves are applied to the collected physics data reconstructed with both, Gauss and ZAC, estimators. The prompt analysis of the calibration data reconstructed with the Gauss estimator provides an immediate probe of the detectors' performance. By monitoring the stability of the 2.6 MeV line between every two consecutive calibrations, the instability of the detector's system was identified, and the corresponding periods of data taking excluded from the physics data analysis.

In the framework of the presented Ph.D. thesis, 47 calibration runs collected between December 2018 and April 2017 were analyzed, and calibration curves were provided to estimate the physics energy values of the collected events. The analysis presented in this chapter contributed to the $0\nu\beta\beta$ analysis with the results presented in Ref. [65] and [87]. The physics dataset for the $0\nu\beta\beta$ analysis was selected according to the observed instabilities between the calibrations. For the analyzed calibration dataset the estimated mean (RMS) of the 2.6 MeV shifts is of -0.01 keV (0.3 keV) and 0.06 keV (0.2 keV) for the BEGe and Coax datasets, respectively. The mean value for the FWHM of the 2.6 MeV line was estimated to be 3.17 keV and 3.76 keV for the BEGe and Coax datasets, respectively.

From the selected datasets, the combined calibration analysis was conducted to provide the energy resolutions for the physics analysis, for the smearing of the background Monte Carlo spectra, and importantly to estimate FWHM at $Q_{\beta\beta}$. For the analyzed dataset, the FWHM at $Q_{\beta\beta}$ is estimated to be (2.95±0.06) keV and (3.9±0.1) keV for the BEGe and Coax datasets, respectively.

Chapter 4

Gamma Background Study

In this chapter, the γ background of the GERDA experiment was studied. The goal was to estimate the count rate (counts normalized by exposure) for the expected γ lines. This study served as a cross-check for the background model of the GERDA experiment for the Phase II dataset, collected between December 2015 and April 2018 (see Chapter 2). The observed activities were compared to the results estimated previously for the Phase I dataset presented in Ref. [88].

The γ background was primarily studied for the enriched BEGe and Coax datasets. Additionally, the dataset collected from the three coaxial-type detectors with the natural abundance of ^{76}Ge was included. To distinguish datasets from the coaxial detectors enriched in ^{76}Ge and those with a natural abundance, they are referred to as Coax and Natural datasets, respectively, throughout this chapter. The count rates of each γ line were estimated with and without LAr veto cuts. Although the LAr veto is not yet included in the background model, it is the subject of future improvements, and this part of the study is a prerequisite for future cross-validation. To gain perspective on the findings for very weak lines, their model expectations were studied as well.

This chapter is organized as follows. Section 4.1 introduces the flow of the GERDA background analysis, and the role of the γ intensities study. In Section 4.2, the background spectra of GERDA are discussed. Section 4.3 describes the analysis procedure developed for the γ intensity study, including the signal and background models, and the flow of the statistical analysis. Section 4.5 presents the estimated contribution for each γ source and compares this contribution with the expectation from the background model. In Section 4.6, the results are summarized and discussed. The spectral contribution from each γ background component is presented in appendix Chapter 6.

4.1 Introduction

The search for $0\nu\beta\beta$ decay requires an excellent understanding of the background components at $Q_{\beta\beta}$. Due to the rarity of $0\nu\beta\beta$ decay, every unknown background component with an energy deposition close to $Q_{\beta\beta}$ can mimic the sought signal. Furthermore, in the statistical analysis, the fit model includes the expected signal signature and the background distribution around it.

To understand the background in GERDA, the background model was built in several stages. Before the experiment assembly, a sample of each material was screened with a high-purity

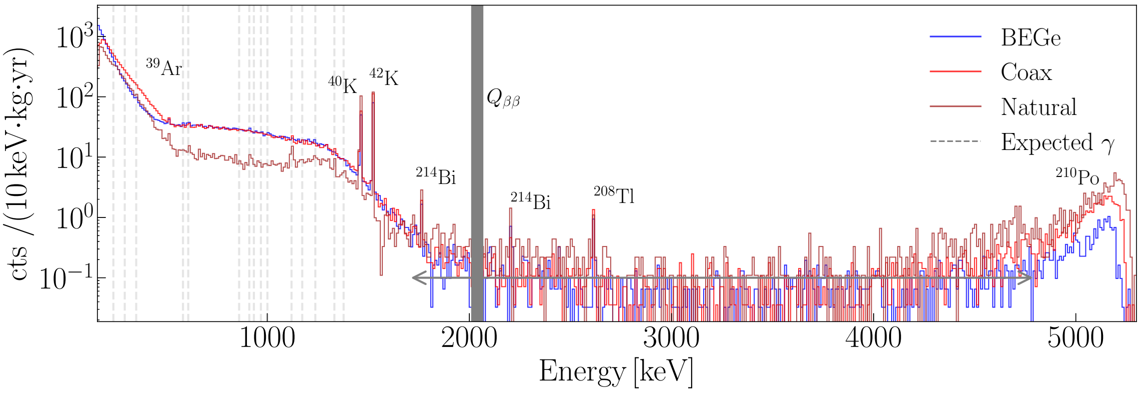

Figure 4.1: Phase II physics spectra (before pulse shape discrimination and LAr veto cuts) normalized by exposure for BEGe, Coax, and Natural datasets. The vertical grey band indicates the blinded region for the $0\nu\beta\beta$ analysis. Vertical dashed lines mark positions of the expected γ lines. The horizontal arrow marks the energies of the low count part of the spectra, i.e., the region with the constant background rate, ~1 cts/keV.

germanium detector (HPGe). Thus, for the Phase II assembly, the activities of the ^{226}Ra, ^{228}Th, and ^{40}K were estimated for signal cables, electronic front-end, detectors holders, and parts of the LAr veto. The screening measurements were used to select sufficiently radio-pure materials and provided prior knowledge for developing the background model.

The background components are simulated with the GEANT4 library, according to the screening measurements and physics data analysis. The simulated model is fit to the collected physics data, and the background components with the maximum probability are selected. As a part of the background modeling campaign, the count rates of α events, and of γ rays due to decays of ^{40}K and ^{42}K are estimated individually for each detector from the single-detector dataset. Additionally, the count rate of the mentioned γ lines is estimated from the two-detector dataset (i.e., occurring coincidentally in two different detectors) with the sum energy equal to γ ray energy. The estimated count rates provide prior knowledge of the location and quantity of background components for future simulations.

For the $0\nu\beta\beta$ search data release described in Chapter 2, the background modeling and γ line analysis were performed. The results of the modeling were cross-checked with the intensities of the γ lines estimated from the physics data. The analysis was based on Bayesian inference using the BAT toolkit [89]. The γ lines' count rates were estimated from marginalized posterior probability density functions (pdf) obtained as a result of the Bayesian fit.

4.2 GERDA Background Spectra

The GERDA spectra from the Phase II datasets are displayed in Fig. 4.1. The exposures of the enriched datasets are summarized in Chapter 2, while the collected exposure for the Natural dataset is 9.1 kg·yr.

At the low energy end, the physics spectra are dominated by electrons due to the β decay of ^{39}Ar and $2\nu\beta\beta$ decay of ^{76}Ge . ^{39}Ar is produced from the interaction of cosmic muons with natural argon in the atmosphere [90] and thus is present in the liquid argon surrounding the detectors. With a half-life of 269 yr, ^{39}Ar decays to a ground state of ^{39}K with an endpoint of

565±5 keV.

From the Q-value of ^{39}Ar to 1.7 MeV, the dominant background component in the spectra is the Compton continuum due to ^{40}K/^{42}K decay and energy distribution of electrons emitted in $2\nu\beta\beta$ decay of ^{76}Ge (for most recent results see Ref. [91]). The $2\nu\beta\beta$ decay spectrum is less dominant for the Natural dataset due to the low concentration of ^{76}Ge in the detector volume; therefore, other background components, in particular, γ peaks, are expected to be more prominent in the spectrum. Around the $Q_{\beta\beta}$, the background is dominated by α, β, and γ rays emitted in the background components' radioactive decays, such as ^{238}U, ^{232}Th, ^{40}K, ^{60}Co, ^{42}K, present in the detector vicinity. The γ background, which densely populates the spectra up to 3 MeV, appears as a Compton continuum or monoenergetic peaks along the energy spectrum and originates from the prompt γ ray emission accompanying α and β decays. The observation of the γ lines in the energy spectra was used as a cross-check for the background model. The estimated intensities from specific background components are discussed in Sec. 4.5.1.

The α background is dominant from the Q-value of the ^{42}K decay at 3.5 MeV toward the high energy end of the spectra, seen as a continuous distribution. The radioisotopes ^{226}Ra and ^{210}Po with Q-values of 4.87 MeV and 5.4 MeV, respectively, constitute a major part of the α background. The detection of the α events is possible only from the surface of p^+ electrode, or the groove separating the p^+ and n^+ electrodes. Given that the p^+ surface of the coaxial detectors is larger than that of BEGe, more α events are observed, as displayed in Fig. 4.1. Because the α particles lose energy when they pass through the detector's dead layer, the detected events have energies below their Q-values (i.e., degraded), contributing to the background around the $Q_{\beta\beta}$.

4.3 Analysis Procedure

In this analysis, the intensities of selected γ lines from known background sources were studied employing Bayesian inference. The model used for the Bayesian fit is described in detail in this section. A sketch of the analysis workflow is presented in Fig. 4.2. The analysis included the count rate estimation from the physics data and the background model expectations for comparison. The count rate was studied on the spectra collected with anti-/coincidence with the LAr veto, referred to as LArAC/LArC.

4.3.1 Bayesian Fit

Here is a short summary of the mathematical basics of the Bayesian fit, performed for the count rate estimation of the background γ lines. The desciption is adapted from [89]. Here $\vec{\lambda}$ stands for parameter of interest, $\vec{\nu}$ are the nuisance parameters, $\vec{D}$ is analyzed dataset, M is a constructed model. The Bayes theorem states that the conditional probability for the $\vec{\lambda}$ and $\vec{\nu}$, given $\vec{D}$ and M, is the ratio of the conditional probabilities of the individual components written in the following way:

$$P(\vec{\lambda}, \vec{\nu}|\vec{D}, M) = \frac{P(\vec{D}|\vec{\lambda}, \vec{\nu}, M)P_0(\vec{\lambda}, \vec{\nu}|M)}{\int P(\vec{D}|\vec{\lambda}, \vec{\nu}, M)P_0(\vec{\lambda}, \vec{\nu}|M)d\vec{\lambda}d\vec{\nu}}. \tag{4.1}$$

The denominator of the equation defines the full posterior pdf for all included parameters

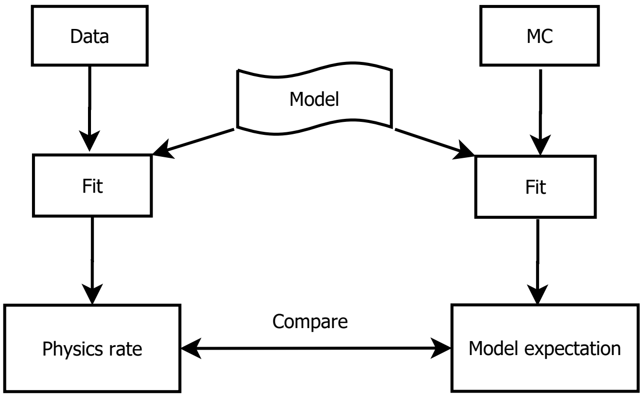

Figure 4.2: The work-flow of statistical analysis for the γ background study. A Bayesian fit is performed on both, physics data and MC simulations, with an identical fit model. From the fit of the MC data, the statistical expectation to the various γ lines is estimated. By comparing the results from the physics data analysis to the model expectations, the presence of background component is inferred.

of the model. $P_0(\vec{\lambda}, \vec{\nu}|M)$ are the prior probabilities on the the parameters $(\vec{\lambda}, \vec{\nu})$, containing all the a priori known information about their values. $P(\vec{D}|\vec{\lambda}, \vec{\nu}, M)$ is the probability density for given model M and parameters $(\vec{\lambda}, \vec{\nu})$, that defines the likelihood of the observed data given assumed model. Given the Poisson nature of the observed counts, the likelihood of the observation in one bin is:

$$P(\vec{D}|\vec{\lambda}, \vec{\nu}, M)_j = \frac{(\nu_b^j + \nu_s^j)^{N_j} \cdot exp(-(\nu_b^j + \nu_s^j))}{N_j!}, \tag{4.2}$$

with the expected number of background and signal events in the jth bin $\vec{\nu_j} = (\nu_b^j, \nu_s^j)$. The overall probability to obtain the data given the model in the spectrum containing N bins is the product of Eq. (4.2) over all bins:

$$P(\vec{D}|\vec{\lambda}, \vec{\nu}, M) = \prod_{j=1}^{N} \frac{(\nu_b^j + \nu_s^j)^{N_j} \cdot exp(-(\nu_b^j + \nu_s^j))}{N_j!} \tag{4.3}$$

For a Gaussian signal and uniformly distributed background, the estimated number of the background and signal events in one bin j from the Eq. (4.3) becomes:

$$\nu_s^j = \int_{E_j}^{E_{j+1}} \frac{\lambda_s}{\sigma\sqrt{2\pi}} \cdot \exp(-\frac{(E-\mu)^2}{2\sigma^2})dE, \tag{4.4}$$

$$\nu_b^j = \int_{E_j}^{E_{j+1}} \frac{\lambda_b}{\Delta E} \cdot dE = \frac{\lambda_b}{\Delta E} \cdot (E_{j+1} - E_j) \tag{4.5}$$

where λ_b and λ_s are the expected total background and signal events, μ and σ are the mean and resolution of the signal's Gaussian distribution, ΔE is the fit range, E_j and E_{j+1} the energy values of the left and right edges of the bin.

The probability for $\overrightarrow{\lambda}$ to have a certain value is defined from marginalization of the full posterior pdf in Eq. (4.1), obtained with Markov Chain Monte Carlo (MCMC) sampling [92]. The mode, or best fit value, is the value which maximizes the marginalized posterior pdf. If the mode of the posterior pdf within its standard deviation is above zero, the count rate is defined by the mode value and 68% central interval. In the opposite case, an 90% CI upper limit on the count rate from the marginalised distribution is given instead.

Fit Model

The signal's count rate at the given energy E_0 (μ in Eq. (4.4)) is estimated from the binned fit to the data in a window around E_0. For γ lines with positions below 1700 keV, the fit was implemented as a linear function to describe the background and a Gaussian function $G(\mathcal{N}, E_0, \sigma)$ to describe the signal:

$$M_0 = B + I \cdot (E - E_0) + G(\mathcal{N}, E_0, \sigma), \tag{4.6}$$

where E_0 is a position of the fitted γ line, and σ is the energy resolution of the dataset. The linear background model was shifted to E_0 to reduce the correlation between the slope and offset values to enhance the Bayesian fit stability.

The spectra above 1700 keV and below 4800 keV range are approximately flat, i.e., have about the same event count in every bin, O(1) cts/keV as illustrated in Fig. 4.1. For the γ lines at this energy range, the background distribution was fit with the constant function (i.e., I = 0 in the Eq. (4.6)) to boost the Bayesian fit convergence. As Section 4.3.2 illustrates, this change of the fit function has not affected the fit results.

At some energies E_γ, the presence of another γ line is expected within the fit window according to the background model. In this cases, a second Gaussian was added to the pdf function to describe the additional background peak:

$$M_\gamma = M_0 + G(\mathcal{N}_\gamma, E_\gamma, \sigma_\gamma) \tag{4.7}$$

One of the examples for such model is the fit of the 514 keV line, expected due to the β decay of the ^{85}Kr, where an additional peak was expected at 511 keV due to e^+e^- annihilation (see Section 4.5.3).

Fit Parameters

The fit was performed over a local fit window. The signal region for the fit was defined as 1.5 times FWHM around the fitted line, as illustrated schematically in Fig. 4.3.

The intensity of the Gaussian signal was the primary parameter of interest $\overrightarrow{\lambda}$ in the analysis, the shape of the background distribution, the position, and energy resolution of the signal were nuisance parameters $\overrightarrow{\nu}$ for the Bayesian estimation. In the Eq. (4.1), the conditional probability of the parameters ($\overrightarrow{\lambda}$, $\overrightarrow{\nu}$) given the data and model depends on their prior probabilities $P_0(\overrightarrow{\lambda}, \overrightarrow{\nu}|M)$. The priors specify the shape of parameters' distribution and the range over which the parameters can vary.

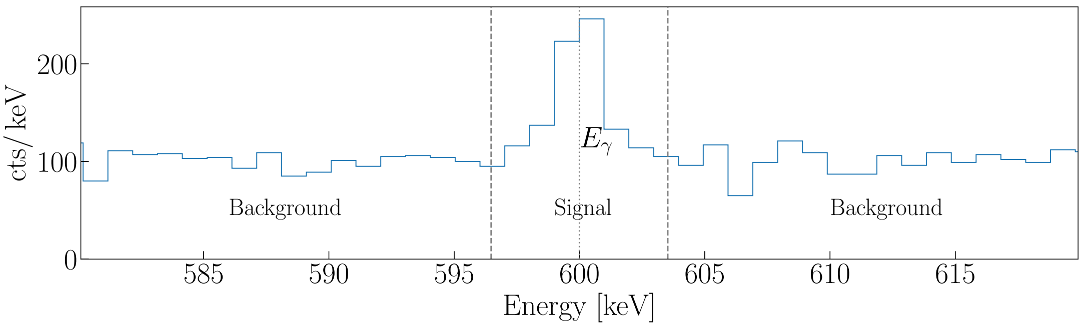

Figure 4.3: Definition of the signal and background regions adapted for this analysis. The signal region is ±1.5 FWHM around the analyzed energy E_0; the area outside is the background region.

The prior on γ peak position (E_0) was chosen to be uniform over the range defined as $E_0 \pm 1$ keV to account for systematic uncertainties on the energy scale. The energy resolution σ in the Gaussian function was fixed to the value estimated from the combined calibration analysis performed for the Phase II dataset following the procedure described in Chapter 3, Section 3.4.

For the signal strength, the maximum allowed value was estimated analytically as follows: First, the average number of background events, B_{avg}, in a single bin was estimated as the ratio of sum of the bins entries, B_i, in the background region to the total number of the background bins (N_{bkg}):

$$B_{avg} = \frac{\sum_{i=1}^{N_{bkg}} B_i}{N_{bkg}}. \tag{4.8}$$

Then, the number of signal events, S, and background events, B_S, in the signal region, containing N_{sig} bins with entries S_i, were estimated as follows:

$$S = \sum_{i=1}^{N_{sig}} (S_i - B_{avg}) \tag{4.9}$$

$$B_S = \sum_{i=1}^{N_{sig}} B_{avg}. \tag{4.10}$$

The chose of the range value for the signal height was defined, such as to provide wide enough range for the parameters variation as:

$$[0;\ MAX((S + 5\sqrt{B_S} + 5\sqrt{S}), 8\sqrt{B_S}, C = 10)] \tag{4.11}$$

The above condition accounts for the particular cases such as of zero counts in the fit range, or background over-fluctuations in the background region, i.e., S < 0.

The Bayesian fit convergence was the most sensitive to the defined range for the parameters of the linear fit components (I, B) in the Eq. (4.6). To ensure priors' accuracy and a reasonable time of MCMC calculation, a preliminary allowed range for those parameters was constructed from the binned fit with the Minuit algorithm using the ROOT package [84]. The parameters were estimated from the linear fit over the entire fit range (±20 keV around the signal) if no peaked background was expected and the signal strength was not significantly higher than expected background fluctuation, i.e.:

$$S < 3 \cdot \sqrt{\sum_{i=1}^{N_{sig}} B_{avg}}.$$

If the above condition was not valid and/or a peaked background was expected, the energy distribution was fitted by a first-order polynomial for the background distribution and a Gaussian for each of the expected peaks. The estimated values from the linear fit were used to set the range for the prior functions of the B and I as the Minuit best fit value ±10 times estimated error.

After the shape and range of the prior functions were defined, the Bayesian fit was performed to obtain posterior pdf distributions. The fit results were accepted if each marginalized posterior pdf was contained at maximum in 60% of the central bins of their histograms. If this criterion was not met, the marginalized posterior pdf quantiles might have been estimated imprecisely (i.e., the posterior might be truncated due to the cut-off in the priors). In these cases, the offset and slope ranges were increased, and the fit was repeated. This inspection was performed automatically as a fit routine procedure; on average, satisfactory results were obtained after three fit iterations.

Histogram Settings

A bin width of 0.3 keV was chosen, which is on the order of the energy scale uncertainties. The fit range was set to 20 keV left and right of E_0 throughout the entire energy range (i.e., the window width was typically 40 keV).

If a background γ line with the energy of E_γ was close to the fit range borders, as demonstrated in Fig. 4.4, the fit range was modified to model this γ line as well. For E_γ outside the fitted window but within one FWHM energy resolution from it, the fit range was decreased by one FWHM, so the counts from the γ background did not affect the fit. For E_γ in the fit window but less than one FWHM away from its edges, the fit range was increased by one FWHM, so the background line was entirely inside the fitted range to be modeled by a Gaussian function. In extreme cases, the minimum and maximum size of the fit window was 34 keV and 46 keV, respectively.

4.3.2 Model Validation

The fit model and procedure were validated on the generated pseudo-dataset by comparing simulated and estimated from the fit signal strength. For each signal strength between 1 and 1000 events, a set of 100 histograms with 10^4 events in each was sampled according to the flat background and Gaussian signal, assuming Poisson fluctuations of the bins' counts. The mean of the Gaussian was set to 600 keV, resolution and background rates were set to values typical for the BEGe spectrum at this energy: 1 keV and 100 cts/1 keV, respectively. Fig. 4.5 provides a selection of the generated histograms.

Fig. 4.6 displays the estimated signal strength compared to the simulated one. The median mode and limit vary due to their definitions; the mode is the value that maximizes the marginalized posterior pdf, while the 90% upper limit is the value of the posterior pdf, below which

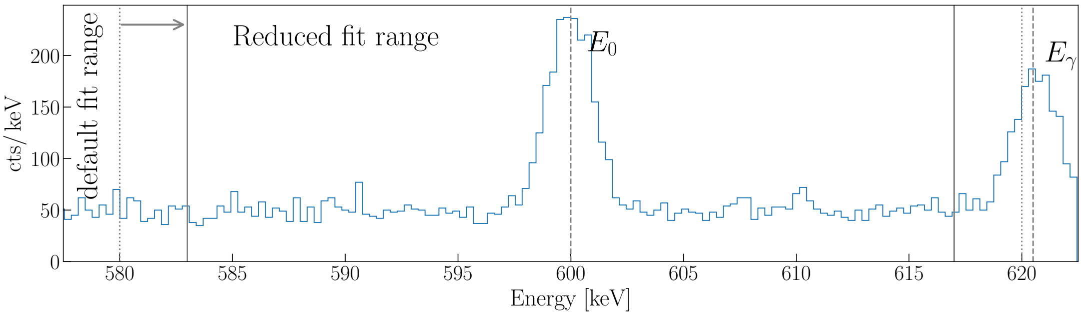

Figure 4.4: The schematic illustration of the reduced fit range in case of the additional background γ line right outside of the fit window. The long dashed lines indicate the position of the peaks, short dashed lines - default fit range, solid lines - the fit range modified accordingly to the position of the second γ line.

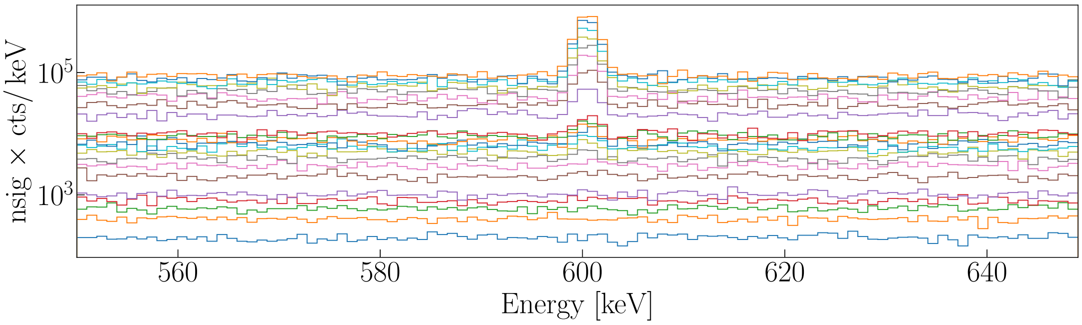

Figure 4.5: Generated histograms according to the fit model in Eq. (4.6), assuming a Poisson nature of the counts. Each histogram is scaled up by the number of simulated signal events for illustration.

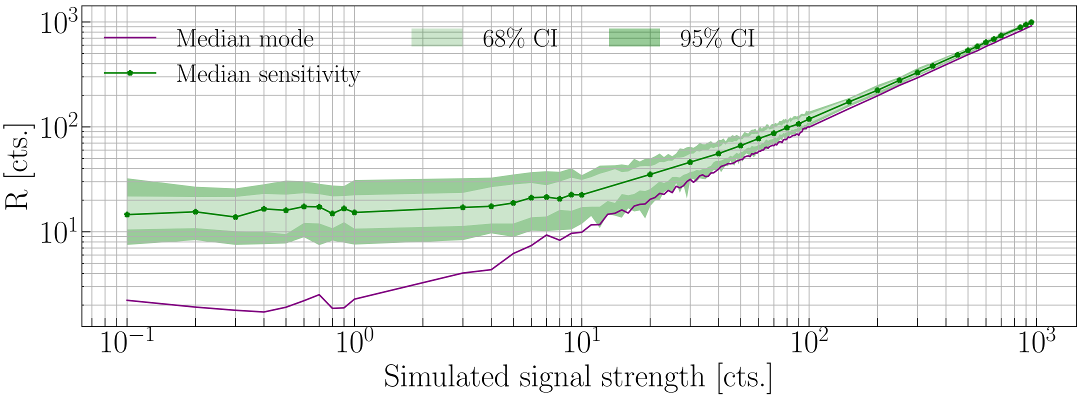

Figure 4.6: Estimated signal strength from the pseudo-data analysis. The solid purple line depicts the median of the best fit values over the analyzed pseudo-dataset. Green bands depict the ranges of the 90% upper limits distribution containing 68% and 90% of generated toy-MC spectra, with the median value indicated with the solid green line.

90% of the posterior pdf is contained. For the weak signal (below 10 cts.), the upper limit is the most representative estimator and is less affected by the statistical fluctuations in the spectra. As Fig. 4.6 indicates, the estimated signal strength within the fluctuations corresponds to the simulated values, thus confirming the constructed analysis procedure's correctness.

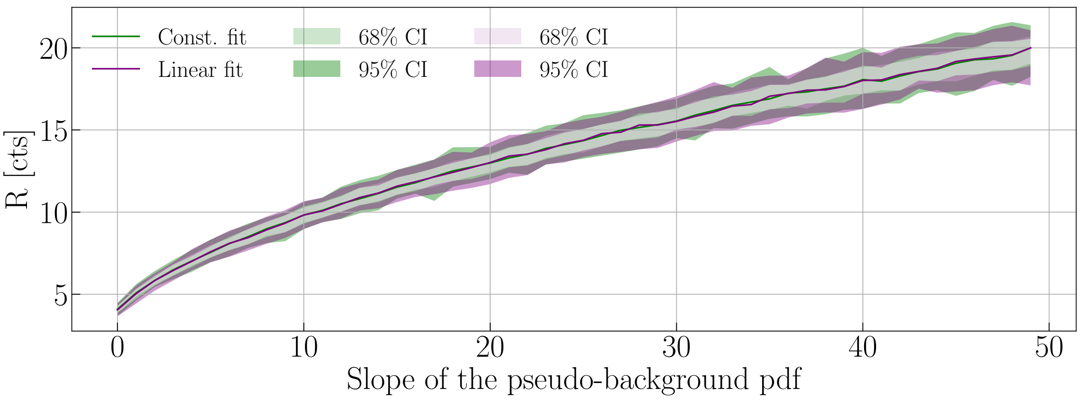

Figure 4.7: 90% upper limit on the signal strength estimated from the fit of pseudo-data assuming linear (purple) and uniform (green) background distribution. The color bands depict the region of the estimated values containing 68% and 90% of generated toy-MC spectra. The agreement of the results obtained with two different fits shows that the estimated count rate of the signal is not biased by switching to the flat background model.

This method was also used to verify the consistency between results obtained from the linear and flat fit functions for the background distribution. For this check, pseudo-data was generated assuming Poisson fluctuations of the counts and sampling from the linear pdf, defined as follows:

$$N(E) = B + I \cdot (E - E_0), \tag{4.12}$$

where B and I are the offset and slope, respectively. One hundred histograms were sampled around the fixed energy value E_0, set to 600 keV, in the 100 keV window, varying the integer slope value from 0 to 50. The histograms were then fit with a Gaussian signal and both, flat and linear, background pdf. The comparison of estimated upper limits using both fit models is provided in Fig. 4.7. The results confirm that a change from the linear to constant fit functions for the background model, as above 1700 keV, does not affect the fit outcome, so the transition between background models can be made without biasing the results.

4.4 Expectation from the Background Model

To evaluate how the determined physics rates compare to background model predictions, the study analogous to the physics data analysis was performed on a set of $O(10^3)$ toy Monte Carlo (MC) spectra. The toy MC dataset was sampled from the background model pdf, assuming Poisson fluctuations of the generated counts in each energy bin. Because the LAr veto is not yet a part of the background model, at this point, only a comparison to the real spectrum prior to the LAr veto could be performed.

The model expectation was estimated for the components with expected energies above 600 keV, for which the background model was constructed and valid. As Fig. 4.8 illustrates, the physics and generated spectrum differ at low energies because two β-decaying isotopes of ^{39}Ar and ^{85}Kr were not included in the background model due to uncertainties in the dead layer modeling, that is needed to simulate the surface events from those β sources.

For each toy MC spectrum, a Bayesian fit with the constructed model was performed as

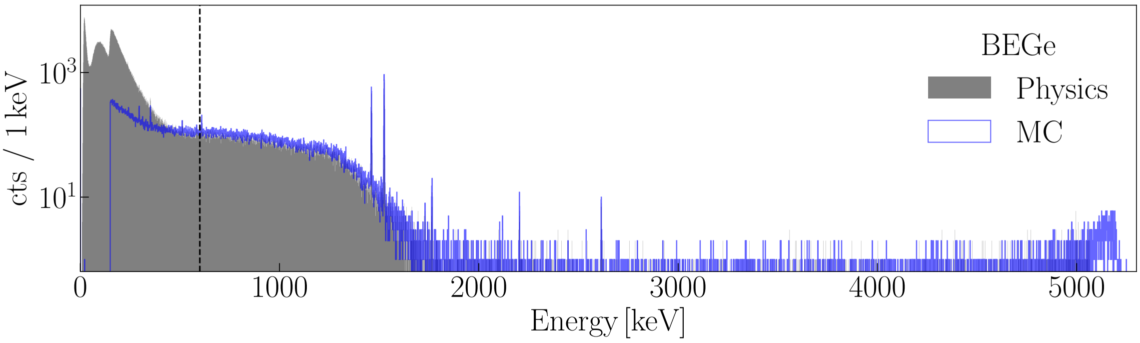

Figure 4.8: Gerda Phase II spectrum of the BEGe dataset (grey) and one of toy-MC spectrum (blue) generated according to the global background model. The background model applies above 600 keV, indicated by the vertical dashed black line, below which additional components not included in the model occur.

described in Section 4.3. The settings on the model parameters were kept identical to the physics analysis, except for the γ lines' positions, which were fixed to the values expected from the literature as there is no uncertainty on the energy scale in the simulation. For each analyzed γ line, a distribution of the upper limits for weakest lines, or the modes for stronger lines, was obtained. The median of this distribution was quoted as the model prediction. The results of each background component are presented in Section 4.5 along with the results from the physics data analysis.

4.5 Background Components

The background sources for the Gerda experiment can be divided into primordial, cosmogenic, and anthropogenic origins. Primordial radionuclides have existed on the Earth since its creation and have half-lives on the order of 10^9 yr. The cosmogenic background is produced in the interactions of the cosmic rays with the detector's material, mostly as a residual from being above ground. The long-lived isotopes are of particular concern for Gerda since they will survive the experiment. The anthropogenic background sources were mostly introduced to the atmosphere during the last century as a result of nuclear weapon tests and nuclear power plants. These sources are contained in atmospheric argon used for the LAr production.

To be detected in the Gerda spectra, a radioisotope must have sufficient abundance, high branching ratio (BR) of the decay, and a Q-value above the data acquisition energy threshold. Here, the search was restricted to the threshold, which was set for most of the Gerda lifetime, around 150 keV; the threshold of around 16 keV, used since October 2017, is of particular interest since it can permit the search for low energy lines. However, the currently collected exposure is not yet sufficient to observe these lines. In summary, the following requirements for the selection of the studied background γ lines were chosen: the BR of the emitted γ rays must be above 0.1%, the Q-value must be above 160 keV, and the presence of the selected background in the detectors' vicinity must be indicated by the screening measurements. The background sources with the Q-value close to, or above, the $Q_{\beta\beta}$are the most critical for the $0\nu\beta\beta$ decay search.

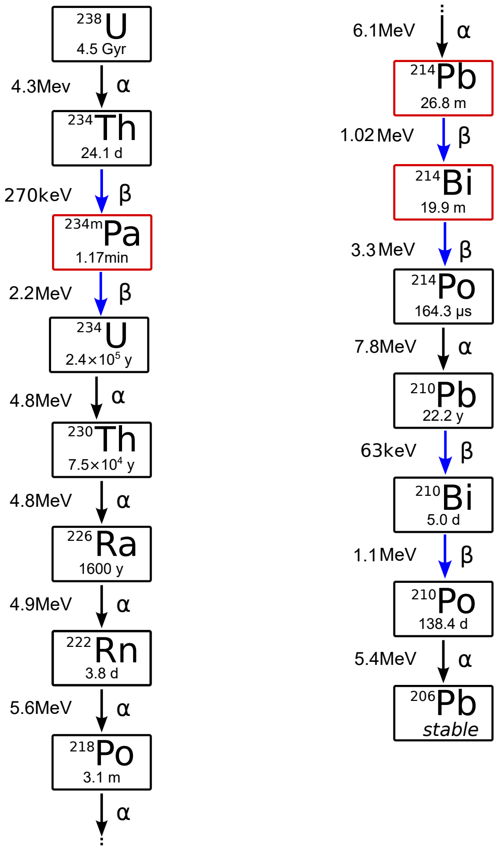

Figure 4.9: Simplified uranium decay chain with the main decay modes depicted. The red rectangles mark the isotopes, the presence of which is expected in the GERDA spectra according to the screening measurements. The indicated parameters are: decay mode (α or β), half-life, and the Q-value (in MeV). The BR of the decays is 100%, unless it is indicated. The decay scheme is adapted from [83].

4.5.1 Primordial Radionuclides

Among the primordial isotopes, ^{238}U , ^{232}Th, and ^{40}K occur naturally in the materials surrounding the GERDA detectors. These isotopes contribute to the energy spectrum through α or β decays, sometimes accompanied by prompt emission of γ rays.

^{238}U Chain

Uranium, a common primordial radionuclide, has the most abundant isotope ^{238}U (99%), the first element in the uranium decay chain (schematically depicted in Fig. 4.9). The decays in the chain are realized with α and β^- emissions until the stable isotope ^{206}Pb is reached. Only a few isotopes in the chain decay directly to the ground state of their daughters; other isotopes decay to excited states, and α or β^- particles are accompanied by the prompt γ rays due to de-excitation. Few isotopes of the chain have sufficient Q-values and BR of the decay modes to be detected in GERDA. The intensities of γ rays emitted in these decays were estimated in this study and are discussed in the current subsection.

The first isotope in the chain observable in GERDA is a metastable isotope of protactinium, ^{234m}Pa , produced due to the β^- decay of ^{234}Th. The screening measurements indicate that ^{234m}Pa

Table 4.1: Count rate estimated for the γ lines from the β decay of $^{234\mathrm{m}}$Pa. The estimated mode of the signal intensity is quoted if its value above zero within the uncertainty, defined as 68% central interval from the posterior marginalized pdf; if this criterion has not been met, 90% C.I. upper limit is established. The units of the count rate are cts/(kg·yr).

$^{234\mathrm{m}}$Pa	BR	BEGe			Coax			Natural		
E_γ [keV]	[%]	prior to LAr	LArAC	LArC	prior to LAr	LArAC	LArC	prior to LAr	LArAC	LArC
1001	0.8	$0.63^{+0.4}_{-0.5}$	$0.64^{+0.5}_{-0.4}$	< 0.44	< 0.96	< 0.86	< 0.50	< 1.67	<1.45	< 0.97
1738	0.1	< 0.15	< 0.16	< 0.10	< 0.16	< 0.11	< 0.19	< 0.51	<0.57	< 0.39
1911	0.1	< 0.13	< 0.10	< 0.12	< 0.14	< 0.11	< 0.17	< 0.54	< 0.40	< 0.45

Table 4.2: As for Table 4.1 for the count rates estimated for the γ lines from the β decay of ^{214}Pb.

^{214}Pb	BR	BEGe			Coax			Natural		
Energy [keV]	[%]	prior to LAr	LArAC	LArC	prior to LAr	LArAC	LArC	prior to LAr	LArAC	LArC
295	18%	$5.9^{+1.6}_{-1.2}$	$4.7^{+0.9}_{-1.2}$	$0.8^{+1.7}_{-0.3}$	$2.1^{+2.4}_{-1.3}$	$1.1^{+2.3}_{-0.9}$	< 2.7	$6.1^{+0.5}_{-5.3}$	$5.7^{+1.8}_{-2.9}$	< 2.2
352	36%	$9.4^{+1.1}_{-1.2}$	$6.9^{+0.9}_{-1.0}$	$2.1^{+1.2}_{-0.3}$	$5.3^{+1.0}_{-2.6}$	$4.4^{+1.9}_{-1.2}$	< 1.4	$10.5^{+1.4}_{-3.0}$	$7.3^{+1.6}_{-2.2}$	$2.2^{+1.5}_{-1.1}$

is contained in mini-shrouds and fibers. ^{234m}Pa ($T_{1/2}$ = 1.17 min) is a possible background source at $Q_{\beta\beta}$ decaying via β-emission to ^{234}U with a Q-value of 2195 keV.

The following energies were selected for the study: 1001 keV (0.8%), 1738 keV (0.1%), and 1911 keV (0.1%). The estimated count rates are presented in the Table 4.1, and the fits are provided in the appendix (Fig. C.1). The slight excess with a significance only of 1.4 σ was observed for the γ line at 1001 keV for BEGe detectors in the spectra prior to LAr cut. For other γ lines, the best-fit value was estimated at zero counts; therefore, only the 90% upper limits are quoted. Comparison with the background predictions displayed in Fig. 4.10 indicates no significant deviations for these lines.

Next in the chain, visible in the GERDA spectra, is ^{214}Pb, product of the ^{218}Po α decay. ^{214}Pb decays ($T_{1/2}$ = 26.8 min, Q = 1023 keV) via β emission to the ground state (6.3%) or to excited states of ^{214}Bi. In this analysis, the following γ lines were studied: 295 keV (18%) and 352 keV (36%). The estimated count rates are presented in Table 4.2, and the fits of the spectral contribution in Fig. C.2. For γ rays with an energy of 295 keV, the estimated count rates are about twice as low as for 352 keV, which corresponds to their BRs. The higher rate for the BEGe dataset compared to the Coax is due to the BEGe detectors' smaller size and larger amount, which leads to an increased amount of material surrounding the detectors per mass. Similarly, the central location of the natural detectors in the array results in a high amount of material around the detectors, and thus in a higher count rate of the γ lines due to the ^{214}Pb decay.

The β decay of ^{214}Bi ($T_{1/2}$ =19.9 min, Q = 3.3 MeV) to the excited states of ^{214}Po has many decay modes. From a possible 295 γ emissions, 11 γ rays with the highest BR were studied in this analysis. The estimated count rates are listed in Table 4.3. The γ rays with the highest BR are 609 keV (46%), 1120 keV (15%), and 1764 keV (15.4%). For the line at 609 keV, the count rate is estimated from 4 to 5 cts/(kg·yr) for the analyzed datasets. The observed line is almost fully in the coincidence with the LAr veto. Intensities for the γ rays with the BR of ~15% are about three times lower than at 609 keV (prior to LAr cut), which corresponds to the decay modes' BR. The γ lines' estimated count rates agree with the expectations from the background model within the uncertainties, except for the line at 1764 keV in the BEGe detectors' energy

Table 4.3: As for Table 4.1 for the count rates estimated for the γ lines from the β decay of ^{214}Bi.

^{214}Bi	BR	BEGe			Coax			Natural		
Energy [keV]	[%]	prior to LAr	LArAC	LArC	prior to LAr	LArAC	LArC	prior to LAr	LArAC	LArC
609	46	$5.0^{+1.1}_{-0.5}$	< 1.4	$4.5^{+0.7}_{-0.4}$	$5.0^{+0.3}_{-1.3}$	$0.8^{+1.1}_{-0.3}$	$3.6^{+0.7}_{-0.5}$	$4.9^{+1.1}_{-1.0}$	< 0.5	$4.9^{+1.7}_{-0.3}$
768	5	$0.8^{+0.6}_{-0.5}$	< 0.8	$1.1^{+0.3}_{-0.4}$	< 1.1	< 0.9	< 0.8	< 1.6	< 0.8	< 1.4
934	3	< 0.7	< 0.7	< 0.4	< 1.1	< 0.9	< 0.6	< 1.3	< 0.8	< 1.1
1120	15	$1.3^{+0.1}_{-0.9}$	< 0.8	$0.6^{+0.7}_{-0.0}$	$1.8^{+1.1}_{-0.4}$	$1.5^{+0.2}_{-0.9}$	$1.0^{+0.4}_{-0.5}$	$2.2^{+0.7}_{-1.2}$	< 1.2	$2.0^{+0.6}_{-0.9}$
1238	6	$1.3^{+0.7}_{-0.4}$	$0.7^{+0.5}_{-0.3}$	$0.8^{+0.3}_{-0.4}$	$0.5^{+0.8}_{-0.4}$	< 0.8	$1.3^{+0.1}_{-0.9}$	< 1.4	< 0.5	< 1.6
1378	4	< 0.6	< 0.5	< 0.4	< 0.8	< 0.4	$0.5^{+0.1}_{-0.4}$	< 0.8	< 0.7	< 0.6
1408	2	$0.7^{+0.4}_{-0.3}$	$0.4^{+0.4}_{-0.2}$	< 0.6	$0.6^{+0.9}_{-0.1}$	$0.3^{+0.5}_{-0.1}$	$0.7^{+0.1}_{-0.5}$	< 0.9	< 0.4	< 0.9
1730	3	$0.5^{+0.2}_{-0.2}$	$0.3^{+0.1}_{-0.1}$	< 0.3	$0.4^{+0.4}_{-0.1}$	< 0.5	$0.2^{+0.2}_{-0.1}$	$0.5^{+0.3}_{-0.3}$	$0.5^{+0.1}_{-0.4}$	< 0.4
1764	15.4	$1.4^{+0.1}_{-0.4}$	$0.5^{+0.1}_{-0.2}$	$0.7^{+0.3}_{-0.0}$	$1.4^{+0.5}_{-0.0}$	$0.8^{+0.2}_{-0.1}$	$0.9^{+0.1}_{-0.3}$	$2.4^{+0.6}_{-0.5}$	$2.0^{+0.2}_{-0.8}$	$0.4^{+0.3}_{-0.2}$
2204	5	$0.5^{+0.2}_{-0.1}$	$0.4^{+0.1}_{-0.1}$	< 0.3	$0.3^{+0.1}_{-0.1}$	< 0.4	< 0.3	$1.2^{+0.5}_{-0.3}$	$0.9^{+0.1}_{-0.6}$	$0.6^{+0.3}_{-0.2}$
2445	1.6	< 0.3	< 0.2	< 0.2	< 0.2	< 0.2	< 0.1	< 0.5	< 0.6	< 0.3

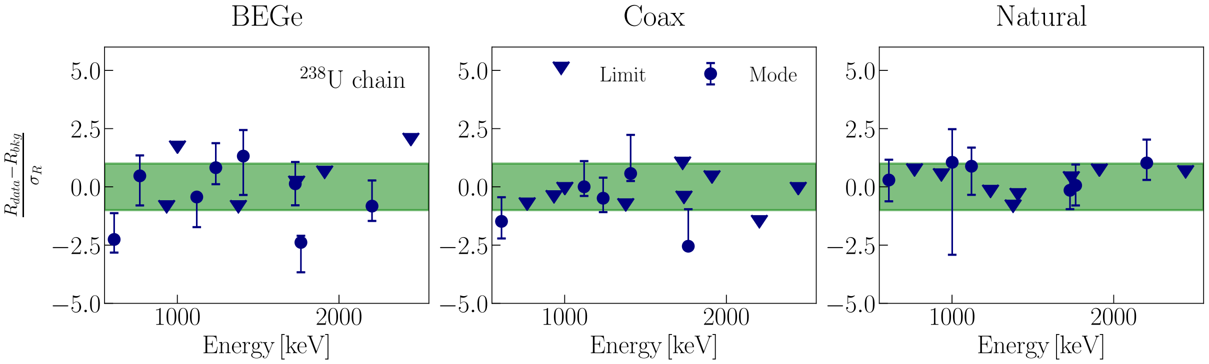

Figure 4.10: Comparison of the background model predictions and estimated physics rates for the γ lines from the ^{238}U decay chain. The figures demonstrate the difference of the limits, or modes for strong lines, normalized over the 68% uncertainty from the background model.

spectrum, as illustrated in Fig. 4.10.

Fig. 4.10 and Table 4.13 present the comparison of the expectations from the background model for the analyzed γ lines from the thorium decay chain. The results agree within the errors, except for two lines from the BEGe dataset: 1001 keV (due to ^{234m}Pa) and 1764 keV (due to ^{214}Bi).

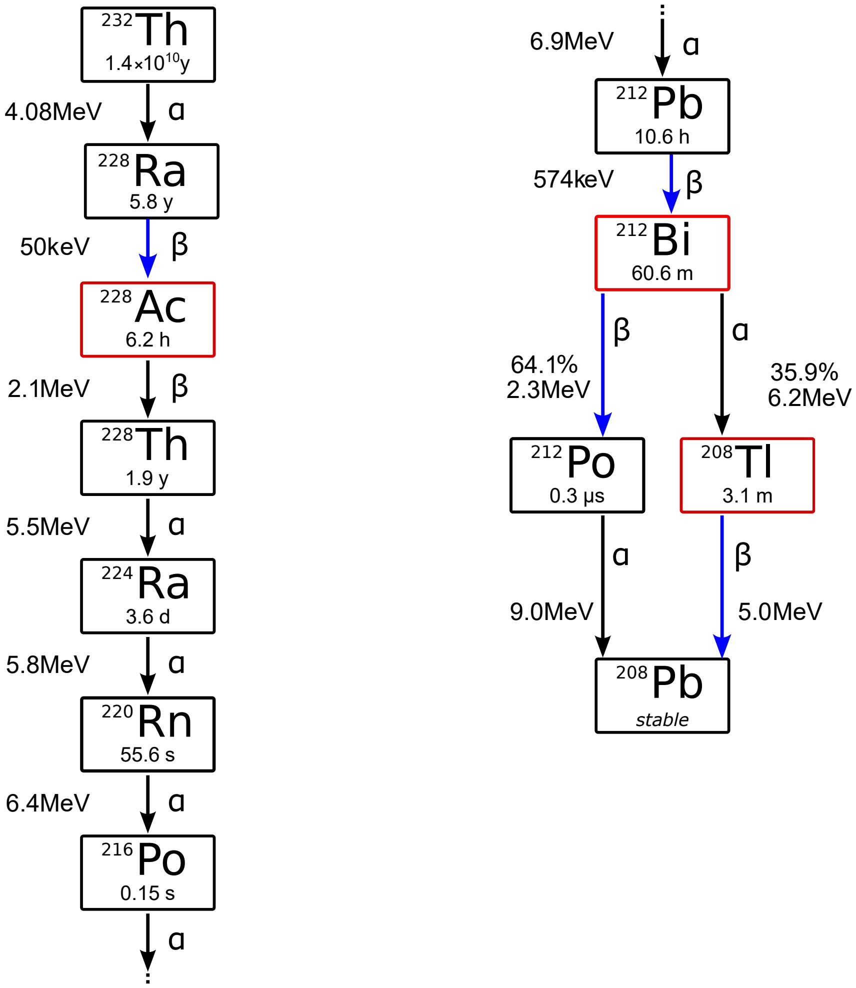

Figure 4.11: As for Fig. 4.9 for the thorium decay chain.

^{232}Th Chain

Thorium's most abundant isotope ^{232}Th (~100%), the first element in the thorium decay chain, is schematically depicted in Fig. 4.11. The decay in the chain occurs via α and β^- emission until the stable isotope ^{208}Pb is reached.

In the GERDA data, the first observable isotope in the chain is ^{228}Ac ($T_{1/2} = 6.15$ h, Q = 2127 keV), produced from the β^- decay of ^{228}Ra. According to the screening measurements, ^{228}Ac is contained in mini-shrouds, holders, fibers, and tetratex. In this analysis, four γ rays from its β decay with the highest BR were studied; the estimated count rates are listed in Table 4.4 and the contribution to the physics spectra are presented in the appendix in Fig. C.4. The estimated count rates coincide with their BRs and agree with the background model predictions but have higher values than previously reported for lower exposure Ref. [93]. The higher intensity of the γ line at 338 keV for the Natural dataset can be explained by the lower count rate of the $2\nu\beta\beta$ decay events.

For ^{212}Bi, the next in the chain radionuclide, the screening measurements indicate the presence in fiber-shroud and mini-shrouds. ^{212}Bi ($T_{1/2}$ =60.55min, Q = 2.25 MeV) decays via β emission (64.6%) to ^{212}Po with emission of the γ rays with energy of 727 keV (6.6%). The estimated count rates for this line are displayed in Table 4.5. The values are in agreement with

Table 4.4: As for Table 4.1 for the count rates estimated for the γ lines from the β decay of ^{228}Ac.

^{228}Ac	BR	BEGe			Coax			Natural		
Energy [keV]	[%]	prior to LAr	LArAC	LArC	prior to LAr	LArAC	LArC	prior to LAr	LArAC	LArC
338	11.3%	< 2.0	< 1.6	< 1.5	< 2.7	< 2.5	< 1.7	$5.7^{+1.3}_{-3.4}$	$3.0^{+2.8}_{-0.9}$	$2.4^{+0.2}_{-1.9}$
795	4.3%	< 1.0	< 0.9	< 0.5	< 0.9	< 1.0	< 0.4	< 0.8	< 0.6	< 0.7
911	26%	$2.8^{+0.6}_{-0.9}$	$1.5^{+0.3}_{-0.8}$	$1.4^{+0.4}_{-0.3}$	$0.5^{+0.9}_{-0.3}$	< 1.2	$0.9^{+0.1}_{-0.6}$	$1.9^{+1.1}_{-0.6}$	$1.3^{+0.1}_{-0.8}$	$0.9^{+1.1}_{-0.2}$
969	16%	$1.6^{+0.5}_{-0.7}$	$0.7^{+0.6}_{-0.3}$	$0.8^{+0.2}_{-0.5}$	$1.0^{+0.5}_{-0.8}$	< 1.1	$0.7^{+0.5}_{-0.3}$	< 1.2	$0.5^{+0.5}_{-0.3}$	< 0.7

Table 4.5: As for Table 4.1 for the count rates estimated for the γ lines from the β-decay of ^{212}Bi.

^{212}Bi	BR	BEGe			Coax			Natural		
Energy [keV]	[%]	prior to LAr	LArAC	LArC	prior to LAr	LArAC	LArC	prior to LAr	LArAC	LArC
727	6.6	$0.7^{+1.4}_{-0.2}$	$1.3^{+0.4}_{-0.7}$	< 0.9	< 1.8	< 1.2	< 1.0	$0.8^{+0.7}_{-0.6}$	< 0.7	$0.9^{+0.9}_{-0.4}$

the background model's expectation.

^{208}Tl, the α decay product of ^{212}Bi, is expected to be present in fiber-shroud and mini-shrouds, according to the screening measurements. It is one of the background sources at $Q_{\beta\beta}$ decaying via β^- emission ($T_{1/2} = 3.1$ min, Q = 5 MeV) to the excited states of ^{208}Pb. The following lines were considered for the analysis: 583 keV(85%), 861 keV(13%), and 2615 keV (99.8%). The 510.8 keV γ line with the BR of 23% was not included since it cannot be distinguished from the annihilation peak, which is discussed in Section 4.5.3. The results are presented in Fig. C.5 and in Tab. 4.6. The higher count rate for the BEGe dataset may be similar to that described for the ^{214}Bi due to the higher amount of material surrounding the detectors.

Comparison of the count rates with the background model predictions for the analyzed γ lines from the thorium decay chain is presented in Fig. 4.12. The results agree within 68% uncertainty.

Table 4.6: As for Table 4.1 for the count rates estimated for the γ lines from the β-decay of ^{208}Tl.

^{208}Tl	BR	BEGe			Coax			Natural		
Energy [keV]	[%]	prior to LAr	LArAC	LArC	prior to LAr	LArAC	LArC	prior to LAr	LArAC	LArC
583	84.5	$3.5^{+0.1}_{-1.3}$	$1.2^{+0.1}_{-0.9}$	$1.6^{+0.9}_{-0.0}$	$2.2^{+1.1}_{-0.6}$	$0.7^{+0.7}_{-0.6}$	$1.7^{+0.5}_{-0.4}$	$0.5^{+1.3}_{-0.1}$	< 0.5	$1.4^{+1.0}_{-0.5}$
861	12.42	$0.4^{+0.8}_{-0.3}$	< 1.0	$0.2^{+0.6}_{-0.0}$	< 1.3	< 0.9	$0.3^{+0.7}_{-0.0}$	$1.4^{+0.6}_{-0.8}$	< 1.0	$1.1^{+0.8}_{-0.5}$
2615	99.16	$0.8^{+0.2}_{-0.1}$	< 0.3	$0.8^{+0.1}_{-0.2}$	$1.0^{+0.3}_{-0.2}$	< 0.2	$1.1^{+0.3}_{-0.2}$	$1.0^{+0.2}_{-0.5}$	< 0.2	$1.3^{+0.2}_{-0.5}$

Table 4.7: As for Table 4.1 for the count rates estimated for the γ line at 1461 keV due to ^{40}K disintegration. The estimated count rates for the spectra prior to LAr veto and with the anti-coincidence are almost equal, due to the topology of the EC.

^{40}K	BR	BEGe			Coax			Natural		
Energy [keV]	[%]	prior to LAr	LArAC	LArC	prior to LAr	LArAC	LArC	prior to LAr	LArAC	LArC
1461	10.6%	$48.3^{+1.6}_{-0.9}$	$47.4^{+1.0}_{-1.3}$	$1.3^{+0.3}_{-0.2}$	$59.6^{+2.0}_{-1.2}$	$59.6^{+1.2}_{-2.2}$	$1.2^{+0.2}_{-0.5}$	$106.5^{+6.2}_{-1.0}$	$107.9^{+2.0}_{-4.9}$	$2.6^{+0.8}_{-0.5}$

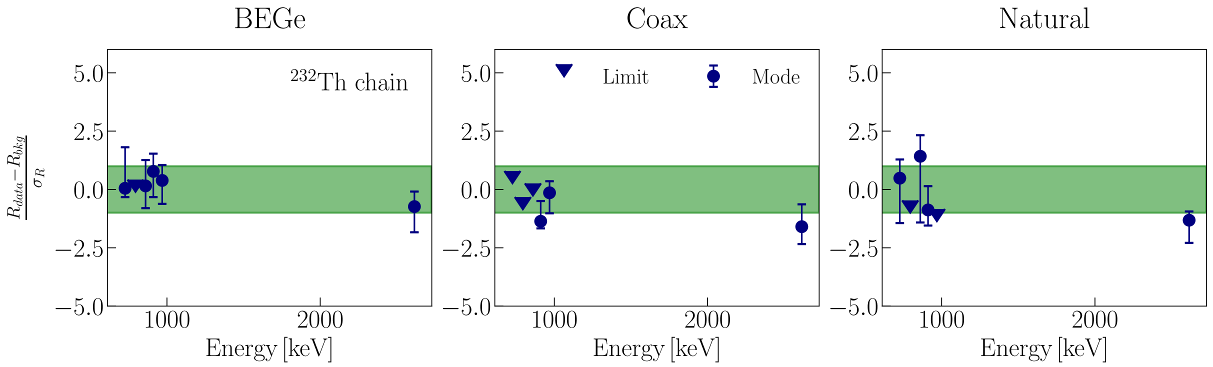

Figure 4.12: As for Fig. 4.10 for intensities of the γ lines expected from the ^{232}Th in comparison to the background model expectations.

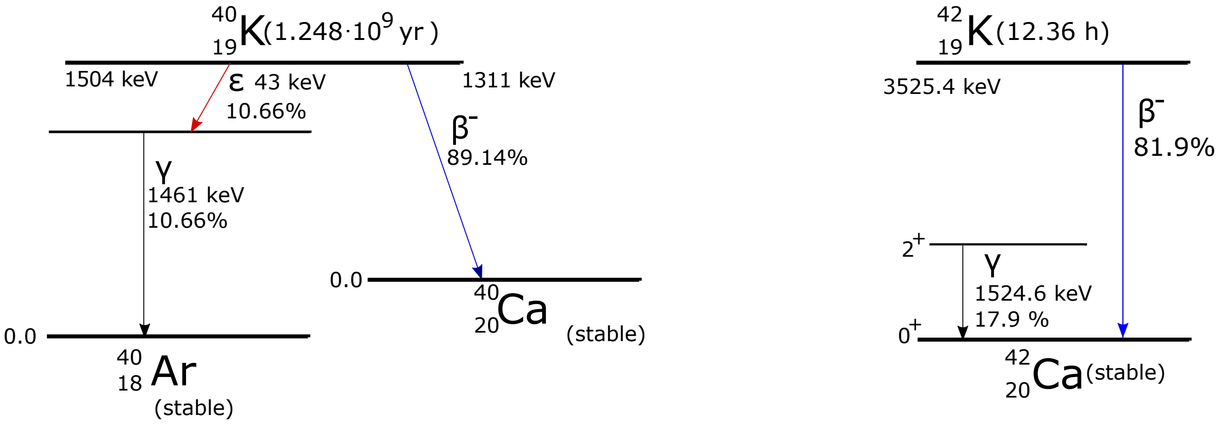

Figure 4.13: Simplified decay scheme of ^{40}K (left) and ^{42}K (right). The intensities of the γ-rays emitted following the EC (for ^{40}K) and β-decay (for ^{42}K) were studied in the analysis.

^{40}K Decay

The third significant contributor to natural radioactivity is ^{40}K with a half-life of $1.248{\cdot}10^9$ yr. ^{40}K is contained in all organic matter, and natural argon is mostly formed from its decay.

In GERDA the exact location of ^{40}K can be easily identified, as there is a strong correlation between contributions from different locations. The background model features a contribution from its presence on the n$^+$-electrodes, in the ring hosting the SiPM, and in the nylon mini-shroud, optical fibers, detector holders, preamplifiers, and cables.

In 10.7% of cases, ^{40}K decays (Q = 1504.9 keV) to an excited state (99.53%) of ^{40}Ar by electron capture (EC) followed by emission of a prompt γ with the energy of 1461 keV due to de-excitation (see Fig. 4.13). This emitted γ forms a high-intensity line in the energy spectra, the study of which plays a unique role in constructing the background model. The count rate of the 1461 keV line separately estimated for each detector is fit in the background model to consider the spatial distributions of ^{40}K around the array.

Because the γ ray with 1461 keV follows the electron capture, no simultaneous energy deposition in the LAr is expected, and the observed γ line is almost entirely in anti-coincidence with the LAr veto. The estimated count rate on the spectra prior to the LAr cut is $48.3^{+1.6}_{-0.9}$, $59.6^{+2.0}_{-1.2}$, and $106.5^{+6.2}_{-1.0}$, cts/kg·yr for BEGe, Coax, and Natural datasets, respectively. Median values from the analysis of the pseudo-data estimate 53, 60.9, and 106.3 cts/kg·yr for the BEGe,

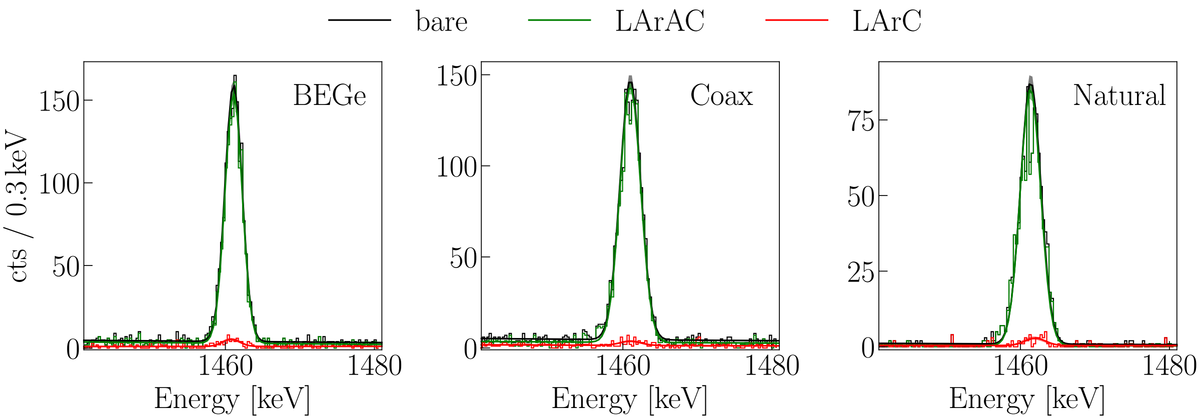

Figure 4.14: Energy spectra of the analyzed dataset around the expected γ line from ^{40}K decay. Given the topology of the EC, the observed γ lines are almost fully in the anti-coincidence with the LAr veto, except of the random coincidences.

Coax, and Natural datasets, respectively. The central location of the Natural detectors in the array can explain a higher estimated count rate. The results are summarized in Table 4.7, and the spectra are presented in Fig. 4.14.

4.5.2 Cosmogenic Background

Cosmogenic radionuclides are formed as a result of nuclear reactions of the neutrons and protons from the cosmic ray air showers with the target material. In this analysis, the count rate for cosmogenic isotope ^{42}K, a result of cosmogenic activation of argon, and ^{60}Co ($T_{1/2}$= 5.27 yr, Q-value = 2.82 MeV), from cosmogenic activation of the germanium crystals, were estimated. Another expected cosmogenic background is ^{68}Ge ($T_{1/2}$= 270.8 d, Q-value = 2.92 MeV). However, due to its low half-life, it vanished from the coaxial detectors during their long period underground, while for the BEGe detectors, the expectation is rather low: 24 events for the entire dataset [63]. Therefore, it was not considered in the analysis.

^{42}K Decay

^{42}K is one of the most highly contributing background components in GERDA at $Q_{\beta\beta}$, decaying with $T_{1/2}$=12.36 h via a β emission with an endpoint of 3525 keV. Charged ^{42}K ions are produced by the β decay of ^{42}Ar, a cosmogenically activated isotope of argon. ^{42}Ar ($T_{1/2}$ =32.9 yr, Q = 599 keV) is produced in the upper atmosphere via ^{40}Ar(α, 2p)^{42}Ar reaction [94]. The ions of ^{42}K drift under the detectors' electric field toward their surface. To mechanically protect each detector string from the ^{42}K accumulation without shielding the scintillation light, transparent nylon mini-shrouds were produced for GERDA Phase II (see Chapter 2 and Ref. [95]). These mini-shrouds, however, do not screen the detectors' electric field, and therefore, the accumulation of the ^{42}K ions is expected on both the mini-shrouds' and the detectors' surface. However, the β particles traversing the detectors' surface can be tagged by PSD techniques due to their slow charge accumulation (see Chapter 2).

The decay of ^{42}K to ^{42}Ca is illustrated schematically in Fig. 4.13. ^{42}K decays to an excited state (17.64%) of the ^{42}Ca, emitting a γ ray with an energy of 1525 keV, resulting in the γ

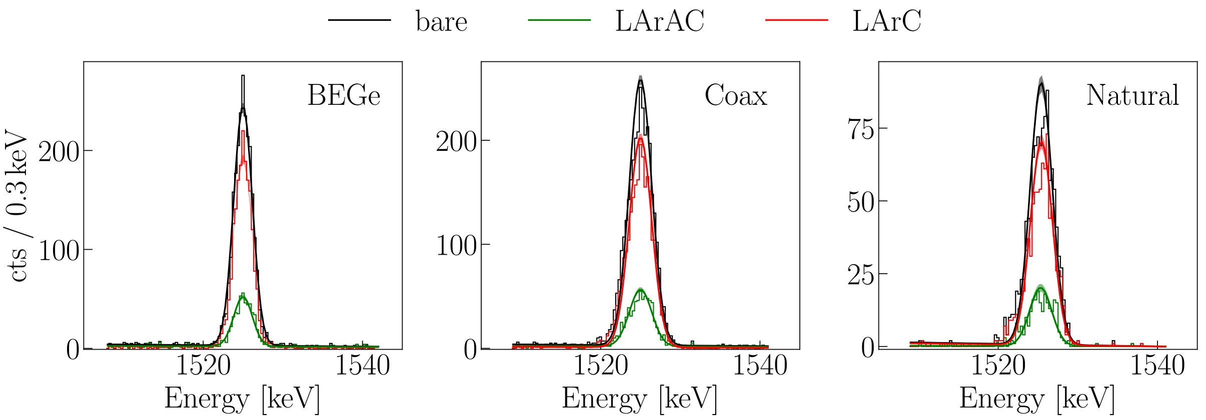

Figure 4.15: Energy spectra of the analyzed datasets around the expected γ line due to ^{42}K β-decay. The observed γ rays follow the emission of the β-particle with an energy of about 2 MeV in the volume of the LAr, therefore most of the observed γ-events are in the coincidence with the LAr veto.

Table 4.8: As for Table 4.1 for the count rates estimated for the γ line with energy of 1525 keV emitted due to ^{42}K β-decay.

^{42}K	BR	BEGe			Coax			Natural		
Energy [keV]	[%]	prior to LAr ¹	LArAC	LArC	prior to LAr	LArAC	LArC	prior to LAr	LArAC	LArC
1525	17.6	$76.2^{+2.1}_{-1.0}$	$16.0^{+0.6}_{-0.8}$	$60.4^{+1.7}_{-1.1}$	$107.8^{+0.9}_{-3.2}$	$24.0^{+1.2}_{-0.9}$	$82.7^{+1.6}_{-2.1}$	$115.4^{+3.8}_{-3.0}$	$26.4^{+0.8}_{-2.5}$	$90.5^{+2.3}_{-3.8}$

peak with the highest intensity in the GERDA physics spectra. The estimated count rate from the 1525 keV line is 76.2 cts/(kg·yr), 107.8 cts/(kg·yr), and 115.4 cts/(kg·yr) for enriched BEGe, Coax, and Natural datasets, respectively. The lower rate for the BEGe detectors compared to the coaxial detectors could be caused by their smaller volume and thus lower probability of full energy absorption of the γ rays. The median count rate estimated from the generated pseudo-data is 85.6, 117.7, and 106 cts/(kg·yr) for enriched BEGe, Coax, and Natural datasets, respectively.

The spectral contribution and count rates for the ^{42}K γ line are provided in Fig. 4.15 and in Table 4.8. Since the γ rays follow the emission of e^- with the energy of 2 MeV, the observed line is almost entirely in the coincidence with the LAr veto. This property is used to monitor the LAr veto suppression, which was estimated between four and five (see Table 4.8).

^{60}Co Decay

^{60}Co is generated by cosmogenic activation of germanium crystals when enriched germanium is processed and transported until it is stored underground. In addition to the cosmogenic

Table 4.9: As for Table 4.1 for the count rates estimated for the γ lines from the β-decay of ^{60}Co.

^{60}Co	BR	BEGe			Coax			Natural		
Energy [keV]	[%]	prior to LAr	LArAC	LArC	prior to LAr	LArAC	LArC	prior to LAr	LArAC	LArC
1173	99.86	$0.9^{+1.0}_{-0.2}$	$0.7^{+0.4}_{-0.4}$	$0.7^{+0.1}_{-0.5}$	$2.1^{+0.7}_{-0.6}$	< 1.1	$1.8^{+0.4}_{-0.6}$	< 1.7	< 0.9	< 1.4
1332	99.98	$0.7^{+0.4}_{-0.4}$	< 0.7	< 1.0	$1.7^{+0.8}_{-0.4}$	< 1.1	$1.6^{+0.2}_{-0.6}$	$2.7^{+0.8}_{-0.9}$	< 0.8	$2.8^{+0.8}_{-0.7}$
2506	sum.	< 0.1	< 0.1	< 0.1	< 0.2	< 0.2	< 0.1	< 0.6	< 0.5	< 0.4

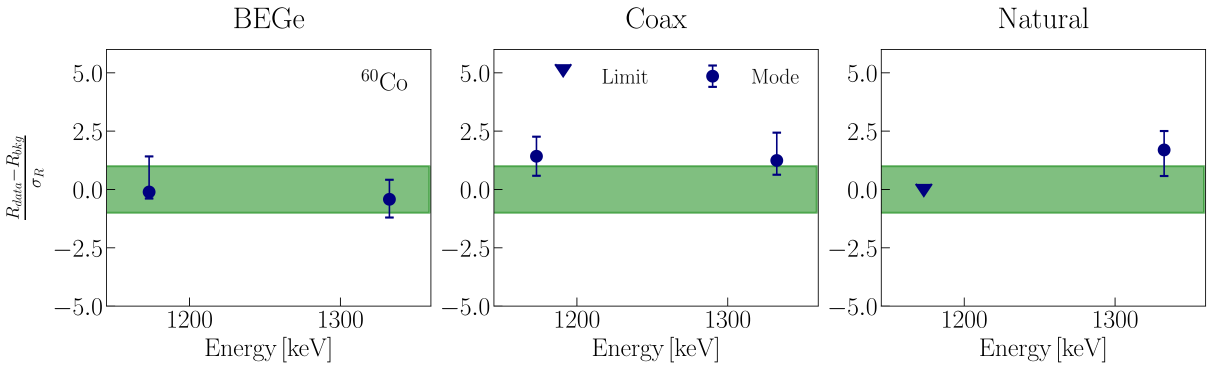

Figure 4.16: As for Fig. 4.10 for intensities of the γ lines expected due to ^{60}Co decay. For the analyzed lines the intensities from the physics analysis are well within the errors from the model expectations.

activation, screening measurements indicate the presence of ^{60}Co in the signal cables containing copper. ^{60}Co ($T_{1/2} = 5.25$ yr, Q = 2824 keV) with 99.88% decays via emission of one β and two γ rays in cascade with the energies of 1173 keV and 1332 keV. The emission probabilities of these rays are about 100%. Since the two γ rays are emitted almost simultaneously, a summation peak may occur at 2505.7 keV. This peak was also analyzed, and the 90% upper limit on its count rate was quoted.

For the γ line at 1132 keV, an excess of the low significance was observed for the analyzed datasets; the estimated count rate is $0.7^{+0.4}_{-0.4}$, $1.7^{+0.8}_{-0.4}$, and $2.7^{+0.8}_{-0.9}$ cts/(kg·yr) for the BEGe, Coax, and Natural datasets, respectively. The count rate estimated for the line at 1173 keV is in accordance with its BR, except for the Natural dataset, where the 90% upper limit is set. The estimated count rates are presented in Table 4.9, while the energy distribution and the fits are in Fig. C.9.

Comparison with the count rates expected from the background model is provided in Fig. 4.16. The estimated values are in agreement with the background model predictions within the uncertainties. The median count rates of the 1332 keV γ line from the background model are $0.9^{+0.5}_{-0.5}$, $0.9^{+0.7}_{-0.6}$, and $1.1^{+0.9}_{-0.8}$ for the BEGe, Coax, and Natural datasets, respectively.

4.5.3 Anthropogenic Radionuclides

Anthropogenic radionuclides originate in the atmosphere from human activities, such as the operation of nuclear power plants or nuclear bomb tests. Some of the isotopes penetrate to the GERDA vicinity through the LAr extracted from the atmosphere, for example, ^{85}Kr and ^{137}Cs, and ^{108m}Ag, which have a high enough Q-value to be detected in the GERDA.

^{108m}Ag decay

^{108m}Ag is typically present in the nuclear power plants' pipe casings and can be released into the atmosphere if an accident occurs. The screening measurements indicate ^{108m}Ag near the detectors [63].

^{108m}Ag ($T_{1/2} = 438$ yr., Q = 2027 keV) decays to the excited states of ^{108}Pd via electron capture (EC)+β^+, followed by the prompt emission of three γ rays in cascade with the energies

Table 4.10: As for Table 4.1 for the count rates estimated for the γ lines from the β-decay of $^{108\mathrm{m}}$Ag. The observed excess of the energies of the γ lines is rather weak, therefore no conclusive statement regarding the presence of the $^{108\mathrm{m}}$Ag in the GERDA data can be made.

$^{108\mathrm{m}}$Ag	BR	BEGe			Coax			Natural		
Energy [keV]	[%]	prior to LAr	LArAC	LArC	prior to LAr	LArAC	LArC	prior to LAr	LArAC	LArC
434	90.5	< 1.4	< 0.9	< 1.1	$0.7^{+1.8}_{-0.3}$	$0.9^{+0.7}_{-0.8}$	$0.4^{+0.8}_{-0.2}$	< 2.3	< 1.5	1.42
614	90	< 1.4	< 0.9	<1.0	$0.9^{+0.8}_{-0.6}$	< 0.9	$1.4^{+0.3}_{-0.6}$	< 1.8	< 1.2	< 1.4
723	90.1	< 1.1	< 1.0	< 0.5	< 1.9	< 1.5	<1.4	< 1.1	< 0.5	< 1.0

Table 4.11: As for Table 4.1 for the count rates estimated for the γ line due to ^{137}Cs β-decay.

^{137}Cs	BR	BEGe			Coax			Natural		
Energy [keV]	[%]	prior to LAr ²	LArAC	LArC	prior to LAr	LArAC	LArC	prior to LAr	LArAC	LArC
662	85.1	$1.1^{+0.9}_{-0.4}$	$1.7^{+0.6}_{-0.6}$	< 0.4	< 1.8	< 1.4	< 1.0	$2.0^{+0.6}_{-1.1}$	$1.2^{+0.5}_{-0.5}$	< 1.5

of 722.9 keV (90.1%), 614.3 keV (90%) and 434 keV (90.5%). The count rate for the γ line at 614 keV is estimated from the simultaneous fit with the line at 609 keV due to ^{214}Bi decay. For the Coax dataset, weak excesses at energies of 434 keV and 614 keV were observed with the significance of 2.3 σ and 1.5 σ, respectively, while for the BEGe and Natural datasets only upper limits were quoted (see Table 4.10). The contribution to the physics spectra is displayed in Fig. C.7. Given the low significance of the estimated count rate, no conclusive statement regarding the presence of ^{108m}Ag in the GERDA can be made. Moreover, the indication from the screening measurements is rather low; therefore, there are no strong reasons for this isotope to be included in the background model.

^{137}Cs Decay

A weak indication of the presence of ^{137}Cs in the Phase II signal readout hardware was found in the screening measurements [63]. ^{137}Cs ($T_{1/2} = 30.1$ yr., Q = 1176 keV) decays mainly (94.7%) via the β^- emission to the metastable $^{137\mathrm{m}}$Ba, which in turn ($T_{1/2} = 2.55$ min) decays to ^{137}Ba, emitting a γ ray with an energy of 662 keV. In the spectra prior to LAr cut, a weak excess was observed for BEGe and Natural datasets with the significance of 2.8σ and 1.8σ respectively. For the Coax dataset, the best fit value was estimated at zero counts within its uncertainty; therefore, only a 90% upper was quoted. The results are summarized in Table 4.11, and the spectral contribution is displayed in Fig. 4.16. As for ^{108m}Ag, the indications for the presence of ^{137}Cs are not sufficient to include this isotope in the background model.

^{85}Kr Decay

Most of ^{85}Kr in the atmosphere is formed from fission of ^{235}U in nuclear reactors. In GERDA ^{85}Kr occurs while extracting argon from the air for the liquid argon (LAr) production; this impacts into the ^{85}Kr being homogeneously distributed in the LAr around the detector array. ^{85}Kr ($T_{1/2} = 10.7$ yr., Q = 687 keV) decays via β^- emission to the metastable ^{85m}Rb, which in turn with the half-life of 1.01 μs decays to its ground state with a γ ray emission of energy 514 keV [96]. The emitted β-particle has an energy which is not enough to be efficiently detected by the LAr veto; therefore most of γ-rays are detected in anti-coincidence with the LAr veto.

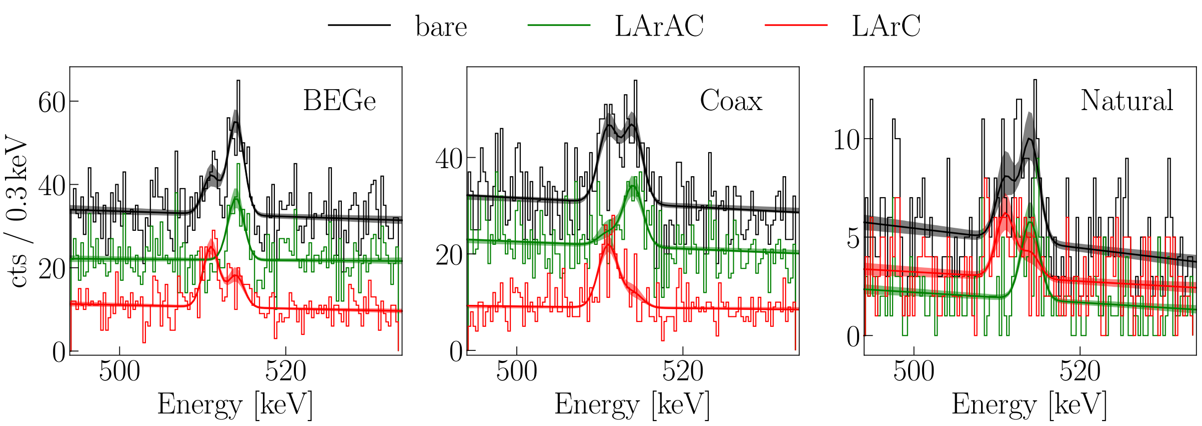

Figure 4.17: Energy spectra of the analyzed dataset around the expected γ lines from ^{85}Kr β-decay and e^+e^- annihilation. The observed γ line at 514 keV is almost entirely in anti-coincidence with LAr veto. In contrast, the line at 511 keV is in the coincidence with the LAr veto due to the annihilation process topology. The count rates were estimated from the simultaneous fit of both peaks.

Table 4.12: As for Table 4.1 for the count rates estimated for the γ line at 514 keV due to ^{85}Kr β-decay, and for the γ line at 511 keV due to e^+e^- annihilation. The values are estimated from the simultaneous fit of both lines.

^{85}Kr	BR	BEGe			Coax			Natural		
Energy [keV]	[%]	prior to LAr [3]	LArAC	LArC	prior to LAr	LArAC	LArC	prior to LAr	LArAC	LArC
514	0.4	$5.9^{+1.0}_{-0.5}$	$4.0^{+0.6}_{-0.7}$	$1.9^{+0.6}_{-0.3}$	$4.6^{+1.6}_{-0.4}$	$4.2^{+0.6}_{-1.0}$	<1.7	$4.6^{+1.9}_{-0.6}$	$4.3^{+0.6}_{-1.2}$	<2.6
annih e^+e^- 511		$2.8^{+0.2}_{-1.3}$	< 0.4	$3.4^{+0.8}_{-0.2}$	$5.5^{+1.1}_{-0.8}$	< 2.1	$4.0^{+1.2}_{-0.2}$	$3.2^{+1.1}_{-1.3}$	< 1.1	$3.5^{+0.9}_{-1.2}$

Fig. 4.17 shows the energy distribution around the 514 keV from the ^{85}Kr decay. The count rate is estimated from the simultaneous fit of both, 514 keV and 511 keV peaks. The latter is a result of the e^+e^- annihilation into two photons, one of which reaches the detector and another one deposits energy in the LAr. Therefore, this line is visible in almost 100% coincidence with the LAr veto.

The results for the 514 keV and 511 keV lines are presented in Table 4.12. The obtained values tend to have asymmetrical errors for both lines, that can be explained by the shape of the posterior marginalized pdfs, see for instance Fig. C.10 for the peak at 511 keV.

This isotope is a subject of ongoing developments to extend the background model to the lower energies, for which the specific activity of ^{85}Kr is a crucial component. The literature [96] suggests (0.16±0.13) Bq/liter, while one of the recent estimations in the GERDA collaboration establishes 0.45±0.16 mBq/l and 0.72±0.23 mBq/l for BEGe and Coax datasets, respectively [97]. The difference in the values is caused by the sensitivities of the experiments to distinguish ^{39}Ar and ^{85}Kr spectral components.

4.6 Conclusion

The count rates of the γ lines were estimated with the Phase II dataset for BEGe, Coax, and Natural datasets. The crucial role of the analysis is to provide cross-check for the background

Table 4.13: Estimated count rates for analyzed γ lines in the Phase II dataset. The data in the table is organized as follows: for each dataset (BEGe, Coax, Natural) the leftmost column shows the count rate, if it is estimated at zero couns then the middle column shows 90% upper limit; the rightmost column shows the model expectations: limits for the weakest lines, or the count rates for the stronger lines. The last two columns show values estimated in Ref. [88] with the Phase I dataset.

			Phase II [mode and 68% cent.int. | 90% C.I upper limit | Expectation from the model]									Phase I	
Isotope	Energy [keV]	BR[%]	BEGe			Coax			Natural			BEGe	Coax
^{228}Ac	911.2	26.2	$2.8^{+0.6}_{-0.9}$	< 3.8	$3.1^{+3.8}_{-2.4}$	$0.5^{+0.9}_{-0.3}$	< 1.8	$3.1^{+4.0}_{-2.2}$	$1.9^{+1.1}_{-0.6}$	< 3.3	$4.0^{+5.0}_{-3.1}$	<8.0	$3.1^{+1.8}_{-2.0}$
	969.0	15.9	$1.6^{+0.5}_{-0.7}$	< 2.4	$2.2^{+2.8}_{-1.5}$	$1.0^{+0.5}_{-0.8}$	< 1.8	$2.3^{+3.1}_{-1.6}$	-	< 1.2	$2.8^{+3.7}_{-2.0}$	<8.2	$6.7^{+1.8}_{-2.1}$
^{208}Tl	583.2	85.0	$3.5^{+0.1}_{-1.3}$	< 3.9	$3.3^{+4.1}_{-2.6}$	$2.2^{+1.1}_{-0.6}$	< 3.7	$3.3^{+4.3}_{-2.5}$	$0.5^{+1.3}_{-0.1}$	< 2.2	$3.5^{+4.4}_{-2.6}$	<11.0	$4.0^{+2.2}_{-2.1}$
	2614.5	99.8	$0.8^{+0.2}_{-0.1}$	< 1.2	$1.4^{+1.6}_{-1.2}$	$1.0^{+0.3}_{-0.2}$	< 1.4	$1.8^{+2.1}_{-1.6}$	$1.0^{+0.2}_{-0.5}$	< 1.5	$2.4^{+2.9}_{-1.9}$	$0.6^{+0.7}_{-0.5}$	$1.5^{+0.4}_{-0.4}$
^{212}Bi	727.0		$0.7^{+1.4}_{-0.2}$	< 2.3	$1.7^{+2.3}_{-1.2}$		< 1.8	$1.9^{+2.8}_{-1.3}$	$0.8^{+0.7}_{-0.6}$	< 2.2	$1.7^{+2.4}_{-1.1}$	-	-
^{214}Pb	352	38	$9.4^{+1.1}_{-1.17}$	-	-	$5.3^{+1.0}_{-2.5}$	-	-	$10.5^{+1.4}_{-3.0}$	-	-	$13.5^{+9.2}_{-7.9}$	$9.6^{+4.3}_{-5.3}$
^{234m}Pa	1001.0	0.8	$0.6^{+4}_{-0.5}$	< 1.4	$0.9^{+1.4}_{-0.7}$	-	< 1.0	$1.2^{+1.8}_{-0.9}$	-	< 1.7	$1.1^{+1.7}_{-0.8}$	-	-
^{214}Bi	609.3	45.5	$5.0^{+1.1}_{-0.5}$	< 6.4	$8.2^{+9.0}_{-7.3}$	$5.0^{+0.3}_{-1.3}$	< 5.7	$7.6^{+8.6}_{-6.5}$	$4.9^{+1.1}_{-1.0}$	< 6.6	$6.1^{+7.3}_{-4.9}$	$12.0^{+2.2}_{-2.5}$	$8.1^{+2.2}_{-2.5}$
	1120.3	14.9	$1.3^{+0.1}_{-0.9}$	< 1.7	$2.4^{+3.1}_{-1.8}$	$1.8^{+1.1}_{-0.4}$	< 3.1	$2.8^{+3.7}_{-2.1}$	$2.2^{+0.7}_{-1.2}$	< 3.4	$2.6^{+3.5}_{-1.8}$	$6.7^{+}_{-4.2}$	<2.9
	1764.5	15.3	$1.4^{+0.1}_{-0.4}$	< 1.6	$2.5^{+2.8}_{-2.2}$	$1.4^{+0.5}_{-0.0}$	< 2.0	$2.9^{+3.2}_{-2.5}$	$2.4^{+0.6}_{-0.5}$	< 3.0	$3.2^{+3.9}_{-2.6}$	<2.5	$3.2^{+0.5}_{-0.5}$
	2204.2	4.9	$0.5^{+0.2}_{-0.1}$	< 0.7	$0.8^{+1.0}_{-0.7}$	-	< 0.5	$1.0^{+1.2}_{-0.8}$	$1.2^{+0.5}_{-0.3}$	< 1.8	$1.3^{+1.8}_{-0.9}$	$1.0^{+0.8}_{-0.7}$	$0.9^{+0.3}_{-0.3}$
^{40}K	1461	10.6	$48.3^{+1.6}_{-0.9}$	-	-	$59.6^{+2.0}_{-1.2}$	-	-	$106.5^{+6.2}_{-1.0}$	-	-	$12.7^{+3.2}_{-3.1}$	$14.1^{+1.1}_{-1.2}$
^{42}K	1525	17.6	$76.2^{+2.1}_{-1.0}$	-	-	$107.8^{+0.9}_{-3.2}$	-	-	$115.4^{+3.8}_{-3.0}$	-	-	$46.6^{+4.6}_{-4.9}$	$60.6^{+2.0}_{-1.8}$
^{60}Co	1173.2	100	$0.9^{+1.0}_{-0.2}$	< 1.9	$1.8^{+2.4}_{-1.2}$	$2.1^{+0.7}_{-0.6}$	< 3.1	$2.0^{+2.7}_{-1.4}$		< 1.7	$2.3^{+3.1}_{-1.6}$	<8.6	$2.9^{+2.2}_{-1.4}$
	1332.5	100	$0.7^{+0.4}_{-0.4}$	< 1.4	$1.6^{+2.0}_{-1.1}$	$1.7^{+0.8}_{-0.4}$	< 2.7	$1.8^{+2.4}_{-1.3}$	$2.7^{+0.8}_{-0.9}$	< 3.9	$2.3^{+3.2}_{-1.6}$	<6.3	<1.9
^{108m}Ag	614.3	90.5	-	< 1.4	$0.8^{+1.2}_{-0.6}$	$0.9^{+0.8}_{-0.6}$	< 2.2	$1.2^{+1.8}_{-0.9}$	-	< 1.8	$1.2^{+1.6}_{-0.8}$	-	-
	722.9	90.8	-	< 1.1	$1.1^{+1.6}_{-0.8}$	-	< 1.9	$1.5^{+2.1}_{-1.0}$	-	< 1.1	$1.3^{+1.9}_{-0.9}$	-	-
^{137}Cs	662.0		$1.1^{+0.9}_{-0.4}$	< 2.3	$1.2^{+1.7}_{-0.8}$	-	< 1.8	$1.6^{+2.2}_{-1.1}$	$2.0^{+0.6}_{-1.1}$	< 2.8	$1.3^{+2.0}_{-1.0}$	-	-
^{85}Kr	514	0.4	$5.9^{+1.0}_{-0.5}$	-	-	$4.6^{+1.6}_{-0.4}$	-	-	$4.6^{+1.9}_{-0.6}$	-	-	-	-
annih e^+e^-	511		$2.8^{+0.2}_{-1.3}$	-	-	$5.5^{+1.1}_{-0.8}$	-	-	$3.2^{+1.1}_{-1.3}$	-	-	$16.5^{+6.4}_{-6.1}$	$10.4^{+2.4}_{-2.6}$

model.

In the presented analysis, no significant deviations with the background model were found. The count rate estimated for the data acquired in anti-/coincidence with the LAr veto will serve as cross-validation for future developments of the background model (see tables throughout the chapter for the individual background components).

The estimated intensity of the γ lines is compared to the results for Phase I [88] in Table 4.13. The observed increase in the potassium background might be due to upgrades in the hardware for the Phase II. The increased number of cables along with the new LAr veto could cause a higher intensity of the γ line at 1460 keV due to ^{40}K decay. The increased intensity at 1525 keV due to ^{42}K β decay is understood as a result of replacing a Phase I copper mini shroud with ones made of nylon. Nylon mini-shrouds mitigate the accumulation of ^{42}K on the detectors surface without screening the scintillation light from the LAr veto; however, in contrast to copper, nylon does not screen the electric field of the detectors, and thus more ^{42}K ions are attracted to the detectors and mini-shrouds [63].

The observed γ background rate due to ^{60}Co β decay is below what is expected from the cosmogenic activation. For 30 BEGe detectors, 300 nuclei of ^{60}Co are expected [63], while the observations summarized in Table 4.9 give a hint for at maximum 150 nuclei being present in the detector material. For the Coax dataset, the estimated count rate for the γ lines due to the ^{60}Co decay indicates that the possible activation of the germanium detectors has decayed over the long period being underground. The results of this analysis did not confirm the slight indications of the screening measurements for the presence of the ^{108m}Ag and ^{137}Cs in the data.

The significant decrease in the presence of the ^{214}Bi and ^{208}Tl background is a remarkable result of the Phase II upgrade, given the increased amount of materials in the vicinity of the detectors and the new LAr veto system. That was achieved via careful selection of materials with the lower radioactivity than those used in Phase I for the high voltage cables, electronic front-end, detector holders, and for the LAr veto system [63].

Chapter 5

Search for bosonic Super-WIMPs

The main objective of the GERDA experiment is to detect low-intensity peaks, such as from $0\nu\beta\beta$ decay, as explained in Chapter 2. The analysis techniques developed for this purpose enable rare-event searches over the entire energy range of the collected data. The highest efficiency for the experiment is achieved for the detection of monoenergetic signals with a sharp peak signature. This experimental potential has motivated the analysis presented in the following chapter. The analysis consisted of two parts: a generic peak search analysis performed over the entire energy range of GERDA, and the results expanded and interpreted in the second part – searching for bosonic Super-WIMPs (Super Weakly Interacting Massive Particle), which are a type of dark matter candidates with a keV-MeV mass range.

The chapter is organized as follows. Section 5.1 introduces the analysis. Section 5.2 details the analyzed dataset. Section 5.3 highlights the key ingredients for the analysis. Section 5.4 describes a model expectations study for the detection of the peaks incompatible with the background expectations. Section 5.5 explains the analysis of the collected physics data. The last section, Section 5.6, describes the application of the generic peak search analysis to the dark matter search and presents the limits on the interaction strength of bosonic Super-WIMPs. Section 5.7 establishes a connection between the statistical analysis and efficiencies of the GERDA experiment. The results of the Super-WIMP search are discussed in Section 5.8.

5.1 Introduction

The generic peak search analysis was developed to search for new physics interactions, or spectral features not compatible with the known experimental background. The data used in this study were collected between December 2015 and April 2018 (see Chapter 2), and analyzed separately for BEGe and Coax datasets. The analysis was based on Bayesian inference and constructed in a way that is similar to the analysis described in Chapter 4, wherein it has demonstrated its robustness independent of the intensity and the energy of the studied signals. The study is conducted in the following way: First, the background model expectations for the rare new physics interaction was investigated using toy Monte-Carlo (MC) data generated according to the background model and assuming no new physics signals. Using Bayesian inference, the simulated data were evaluated in terms of estimate rate, or limit, set on the rate of the peak signal. Second, the same analysis was applied to physics data, and the values were compared to

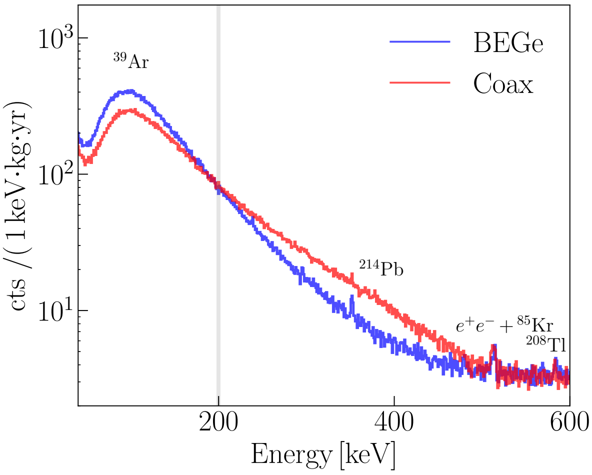

Figure 5.1: Zoom into the low energy range of the analyzed spectra normalized by their respective exposures. The events with energies below 200 keV were collected between October 2017 and April 2018. The vertical grey band indicates the separation point between the low energy data and the rest of Phase II dataset.

the background model to detect the signal not described by the model.

5.2 Dataset and Corresponding Monte-Carlo Simulation

Physics Dataset

The data for the analysis is equivalent the Phase II dataset collected between December 2015 and April 2018 for the enriched detectors, as described in Chapter 2. As in the $0\nu\beta\beta$ decay analysis, the data from BEGe and Coaxial detectors were analyzed as two separate datasets due to their different energy resolution and systematic uncertainties. The Phase II dataset consists of 58.9 kg·yr of collected exposure, shared between BEGe and Coax sub-datasets as 30.8 kg·yr and 28.1 kg·yr, respectively.

The analysis was developed for energies between 120 keV and 5200 keV, where the events below 200 keV were collected after the data acquisition threshold was lowered in October 2017. This low energy dataset will be referred to as a "mini-set", given its low exposure: 7.7 kg·yr and 6.9 kg·yr for the BEGe and Coax datasets, respectively.

In this analysis, the low energy threshold is limited by the shape of the ^{39}Ar β-decay spectrum, with the maximum at around 100 keV. The peak of ^{39}Ar spectrum distorts the linear shape of the background, dominant throughout the energy spectra, thus possibly introduces additional systematic uncertainties. Therefore, for the sake of consistency in the analysis procedure, the energies around the maximum of the ^{39}Ar spectrum were not included. The analyzed datasets and respective energy ranges are summarized in Table 5.1.

For the current analysis, only monoenergetic peaks in the physics spectra were considered. To select those, the following cuts were used. First, the quality cuts were applied; these are fundamental cuts developed to remove events with the non-physical origin, as "pile-up"s, baseline, and test pulses events. Second, muon-induced events tagged simultaneously by the germanium detectors and muon veto were removed, as they do not correspond to the searched-for

Table 5.1: Summary of the analyzed datasets with indicated exposures and corresponding energy ranges.

Dataset	Energy range [keV]	Exposure [kg·yr] BEGe	Coax
"Mini-set"	120-200	7.7	6.9
Phase II	200-5200	30.8	28.1

signal. Finally, events registered simultaneously in more than one detector were removed, as they mainly produced by background originated from the ^{226}Ra decay chain. A more detailed discussion of these cuts can be found in Chapter 2.

Despite the background rejection capabilities of the LAr veto and PSD cuts, they are out of the scope of this analysis for several reasons. The LAr veto is not yet included in the background model that is a pivot ingredient for the study of the toy-MC dataset. The PSD cuts are the most crucial ones for the $0\nu\beta\beta$ analysis; however, the efficiency of this cut below 1000 keV is the subject of ongoing studies and is currently unclear.

Monte-Carlo Data

To study possible systematics, verify the analysis procedure, and estimate the expectations for the count rates of the signals, a set of O(10^3) toy Monte Carlo (MC) spectra was generated, assuming Poisson fluctuations of the counts. Starting from 600 keV, the data were generated with the pdf from the background model, constructed as a superposition of the pdfs for individual background components scaled by their activities.

The background model does not describe physics spectra below 600 keV properly, as it does not include two β-decaying isotopes, ^{39}Ar and ^{85}Kr, with Q-values below 600 keV. Therefore, for each energy below 600 keV, a dedicated set of 10^3 histograms were generated according to the local fit with a linear background model. The parameters of the linear function from which events were sampled were obtained from the Bayesian fit to the physics spectra.

5.3 Analysis Procedure

Count rates for hypothetical peaks were estimated with a Bayesian fit analogous to the analysis described in Chapter 4 with the following modifications of the histograms settings to accelerate MCMC integration and fit convergence. The bin width was chosen to be 1 keV (1 σ energy resolution) throughout the energy range, and the fit window was decreased to 12 keV ($\approx$ 8-10 σ of the energy resolution).

A monoenergetic peak signature smeared by the energy resolution of the germanium detectors can be modeled by a Gaussian peak over a linear background. Thus as for the analysis described in Chapter 4, the total fit model included a Gaussian function to model the signal signature, and background fit function $f_B(E)$:

$$M = G(\mathcal{N}, E_0, \sigma) + f_B(E), \tag{5.1}$$

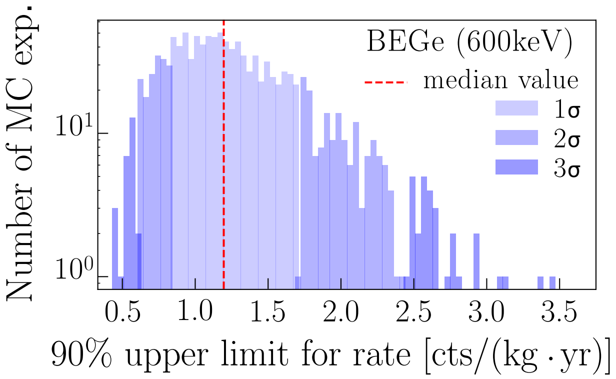

Figure 5.2: Distribution of 90% C.I. upper limits on the signal's count rate for the BEGe dataset from the fit of MC data at 600 keV. Different colors of the histogram show 1σ, 2σ and 3σ quantiles of the distribution. The dashed red line is drawn at the median value.

where $f_B(E)$ was constructed to describe continuous and peak-shape backgrounds, as described in Chapter 4. The selected examples of fits are shown in Fig. 5.4.

The prior pdfs for the Bayesian fit were constructed analogous to the gamma background study, described in Chapter 4, with the exception of the signal's strength, which was fixed to the energy value E_0, around which the fit was performed.

The values of the parameters were extracted from the marginalized posterior pdfs as in Chapter 4. The special treatment of the results from the fits performed at the energy of, or close to, the expected γ background line was introduced. In case of the observed signal at these energies, only upper limits were exacted on the signal, given that the signal is attributed to the presence of the background gamma line or possible uncertainties in modeling those.

5.4 Monte Carlo Study of the Analysis Procedure

To understand fit outputs, systematics, and the interpretation of analysis results, the developed analysis procedure was applied to generated pseudo-data. The study was conducted according to the recipe described in Ref. [98, 99]. For each energy, a toy-MC spectrum was fit with a signal + background model to estimate an upper limit on a hypothetical signal's count rate. From the fit of the entire dataset, a distribution of upper limits was obtained, the median of which indicates which limit is expected in case of no signal. Fig. 5.2 shows, as an example, the upper limits distributions from fit at 600 keV. The dashed red lines mark the position of the median value, and different colors indicate ranges containing 68%, 95%, and 99.7% of toy-MC experiments, corresponding to $1\sigma/2\sigma/3\sigma$ quantiles of the distribution.

Fig. 5.3 illustrates the estimated upper limits distribution versus energy for the BEGe and Coax datasets. Close to the energies of expected γ background lines, the values undershoot the surrounding background. This is an artifact introduced by the uncertainties in modeling signals close to, or at, the background peaks. The distribution for the model predictions around the γ lines is provided in the appendix, Fig. D.3.

The analysis performed on the toy-MC datasets served as a powerful tool for understanding the model behavior while searching for signals not compatible with known background. Fig. 5.3 demonstrates the agreement of the median limit on the count rate with the counts in the energy

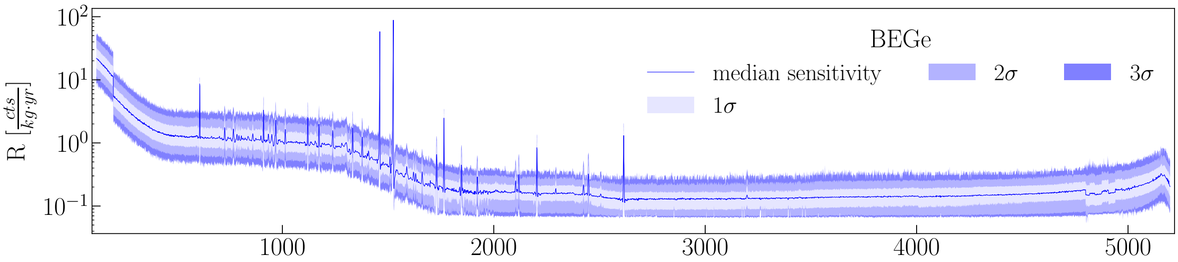

Figure 5.3: Upper limits on the signal's count rate (R) estimated for BEGe (top) and Coax (bottom) datasets from the toy-MC data. Different colors indicate $1\sigma/2\sigma/3\sigma$ expectation bands. The step at 200 keV is caused by different exposures below that energy due to the change in the threshold (see Table 5.1).

.

spectra shown in Fig. 4.1.

5.5 Physics Data Analysis

The analysis of the physics data was performed according to the procedure described in Section 5.3. The fits for several cases with various background models are demonstrated in Fig. 5.4. As for the demonstrated examples, the fit of the signals at 300 keV and 600 keV are performed with steep linear function and with a Gaussian for the background peaks. The background model for the signal at 516 keV consisted of linear function and two Gaussians to fit the gamma lines at 511 keV (due to e^+e^- annihilation) and 514 keV (due to ^{85}Kr decay). The background model for the signal at 1010 keV consisted only of linear distribution.

The conclusion about the signal strength was drawn by comparing its mode to the half width of the 68% quantile of obtained posterior marginalized distribution, σ, defined as:

$$\sigma = \frac{U_{68} - L_{68}}{2}, \tag{5.2}$$

where U_{68} (L_{68}) is upper (lower) 68% quantile's value. As was defined in Section 5.3, if the mode was more than 5σ above zero counts and there was no background γ line in the fit window, signal detection was claimed, and the mode with the error estimated with the 68% quantile were quoted. Otherwise, a 90% C.I. upper limit on the signal strength was set.

The fit procedure was verified with the methods described in Chapter 4 by estimating the limit on the count rate for the signals with known intensity, as well as comparing the fit results obtained with both, linear and flat, background models. Additionally to that, Fig. 5.5 shows the best-fit values for the parameters of the background model, which are consistent with the expectations from the physics spectra shown in Chapter 4.

5.5.1 Results and Discussion

The energies from the fit around which, the mode is estimated to be more than 5σ away from the zero counts, were carefully studied to conclude about the presence of the signal in the energy spectra. As summarized in Table 5.2, all the energies with the observed signal excesses can be

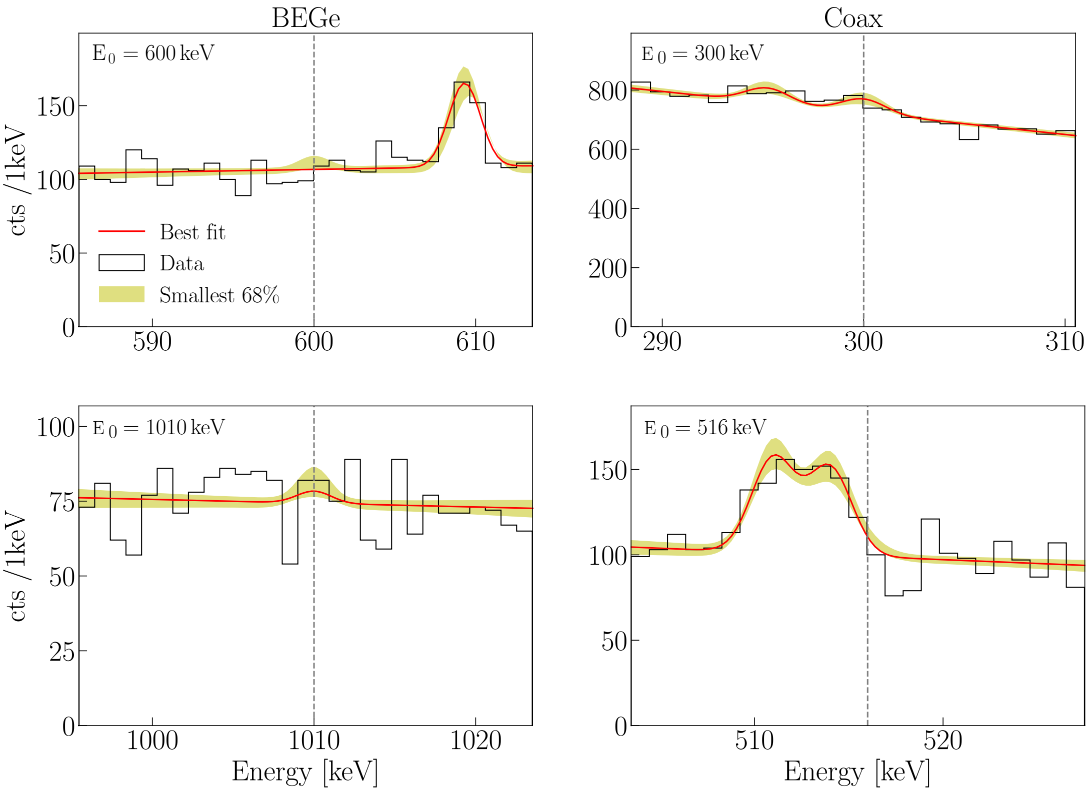

Figure 5.4: Examples of the Bayesian fit at various energies for the BEGe (left) and Coax (right) datasets.

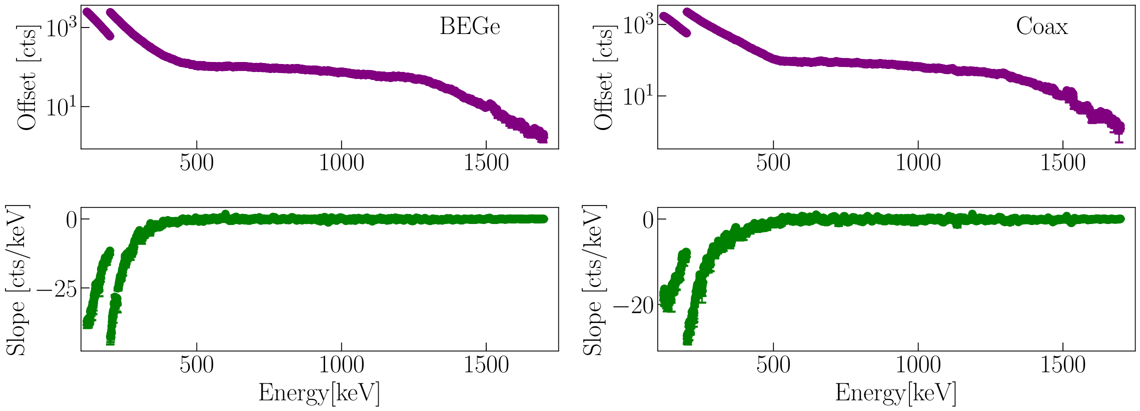

Figure 5.5: Estimated best fit values (mode and 68% central of the posterior pdf) of the parameters for the linear background for the BEGe (left) and Coax (right) datasets. The gap at the energy of 200 keV is caused by the difference in the exposure of the "mini-set" and the Phase II datasets affecting the shape of the energy spectra.

attributed to the known γ lines, the count rates of which were discussed in Chapter 4. The reason for this is likely found in shortcomings of the signal modeling, i.e., deviations of the shapes of the peaks from used models which can become significant for strong peaks.

Thus, no signal incompatible with known backgrounds was observed, and only 90% C.I. upper limits were established. Fig. 5.6 shows the estimated limits in comparison with the expected distribution from the MC study of the analysis. Note, that the energies at $Q_{\beta\beta}\pm 25$ keV

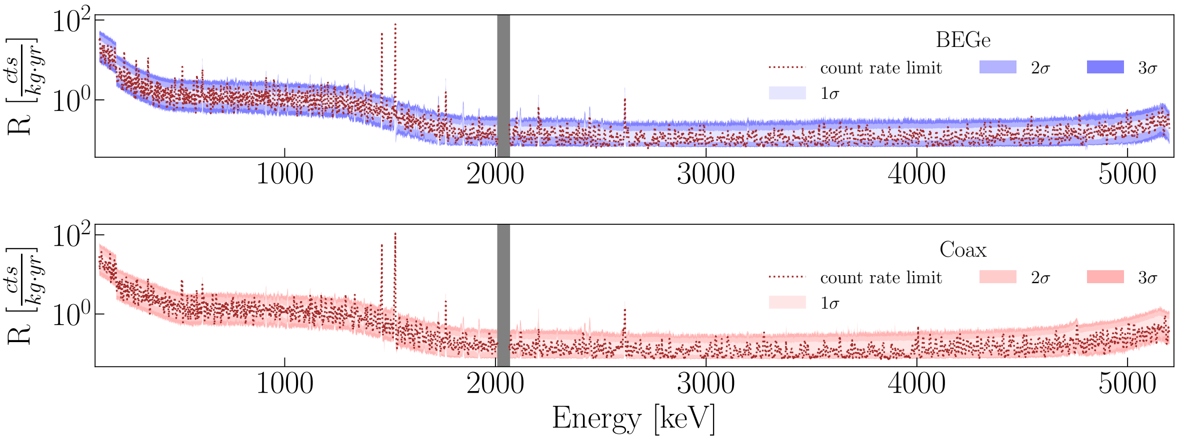

Figure 5.6: The estimated upper limit and expectations from the toy-MC study for the signal's count rate for BEGe (top) and Coax (bottom) datasets. The grey band marks the ROI for the $0\nu\beta\beta$ decay search, which is discussed in detail in Chapter 2.

Table 5.2: The list of energies for which the mode is more than five σ (defined in Eq. (5.2)) away from the zero counts. All the entries can be attributed to the known background γ lines studied in Chapter 4, the entries corresponding to one background line are combined.

Dataset	Energy [keV]	Mode [cts]	Mode/err	Origin
BEGe	238	$14.4^{+1.3}_{-3.7}$	5.8	^{214}Pb
	351	$9.2^{+2.1}_{-0.4}$	7.4	^{214}Pb
	352	$8.2^{+2.3}_{-0.0}$	7.0	
	514	$5.8^{+0.7}_{-1.0}$	7.0	^{85}Kr
	609	$4.9^{+0.4}_{-1.3}$	5.9	^{214}Bi
	610	$4.2^{+1.2}_{-0.3}$	5.4	
	1461	$48.9^{+1.1}_{-1.4}$	39.7	^{40}K
	1524	$12.1^{+1.7}_{-2.6}$	5.6	^{42}K
	1525	$76.1^{+2.1}_{-1.2}$	47.1	
	1765	$1.4^{+0.1}_{-0.3}$	6.4	^{214}Bi
Coax	511	$5.2^{+1.3}_{-0.6}$	5.4	annih.
	514	$5.7^{+0.5}_{-1.4}$	5.9	^{85}Kr
	1457	$2.8^{+0.3}_{-0.8}$	5.5	^{40}K
	1461	$58.4^{+1.7}_{-1.4}$	38.4	
	1520	$4.2^{+0.1}_{-1.0}$	7.5	^{42}K
	1521	$6.7^{+0.7}_{-0.8}$	8.9	
	1522	$11.2^{+0.7}_{-1.4}$	10.9	
	1523	$17.7^{+1.8}_{-1.2}$	11.8	
	1524	$33.4^{+1.8}_{-4.1}$	11.4	
	1525	$105.2^{+3.1}_{-0.8}$	53.6	
	1764	$1.8^{+0.2}_{-0.4}$	6.9	^{214}Bi
	1765	$1.6^{+0.3}_{-0.2}$	6.4	

were not considered in this analysis, given that more detailed study was presented in Ref. [49] and discussed in Chapter 2. Events with energies below 200 keV are from the dataset with the lower exposure, the "mini-set," and hence this region exhibits generally higher limits.

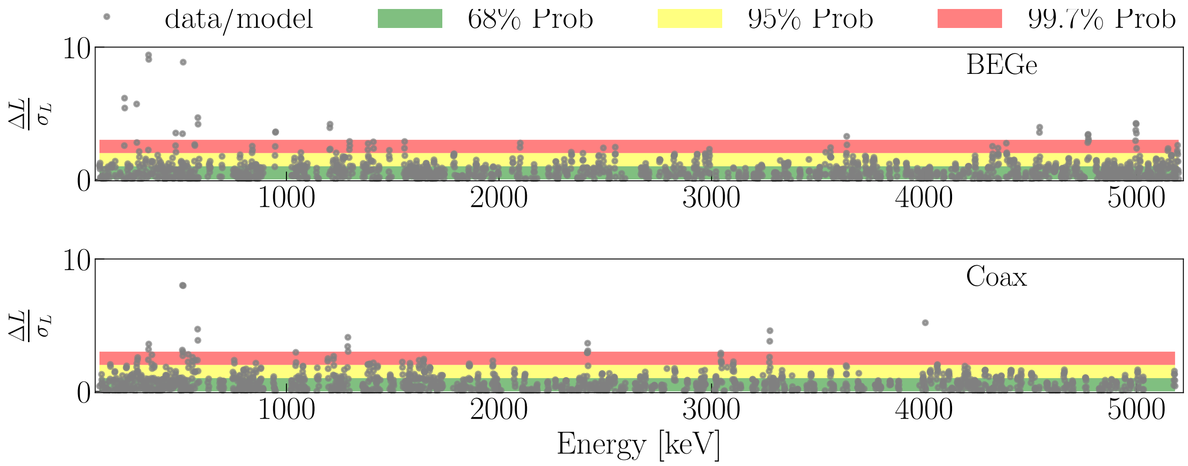

Figure 5.7: Data to model ratio, defined by Eq. (5.3). The top and bottom panel show the results for the BEGe and Coax datasets, respectively. The cases where the limit is above the 3σ expectation band, indicated by the red band, are listed in Table D.1.

The estimated number of events, the limits of which are above the expectations bands throughout the physics energy spectra, is illustrated as data to the model ratio, similar to the concept of residuals defined as:

$$\frac{\Delta L}{\sigma_L} = \frac{L - M}{B - M} \cdot x, \tag{5.3}$$

where L and M are the upper limit estimated from the physics analysis and the median expected limit, x stands for the expectation band containing the limit (e.g., x=1 if the limit lies within 1σ band) and B - is the upper value of this band. Only cases in which L≥M were considered in the calculation.

To investigate the impact of the possible data artifacts not accounted for by the fit model, such as the correlation of the limits from fits of neighboring bins, similar calculations were performed for the toy-MC dataset. For each MC spectrum generated for energies above 600 keV (see Section 5.2), the number of events with limits above the expectation bands (1σ, 2σ, 3σ) was estimated, excluding 20 keV window around the expected background γ lines. This quantity for the entire toy-MC set is presented in Fig. 5.8. The observed value in physics data is in the bulk of distribution from the MC study, giving no indications of a global systematic mismatch between the pseudo-data generated with the background model and physics data.

The physics rates, in the energy range between 120 keV and 5200 keV, excluding 20 keV around the known γ lines, about 23.4%, 4.6%, and 2% of the established upper limits are above 1σ, 2σ and 3σ bands, respectively, for the BEGe dataset. For the Coax dataset, those values are 22.6%, 4.7%, 1.1%. The expectation from toy-MC study shown in Fig. 5.8 yields to the median expected values 26%, 4.2%, and 0.7% for both, BEGe and Coax, datasets.

The energies at which the estimated upper is above the 3σ expectation band are listed in Table D.1. Taking into account correlation from the fits of neighboring bins, the effective number of events with the limits above 3σ band would be reduced from 22 to 12 and from 24 to 13 for BEGe and Coax datasets, respectively. For the following energies, the limits above the expectations are understood to be due to expected γ background lines: 238 keV and 239 keV is from ^{212}Pb decay, 295–300 keV, 351 keV, and 352 keV is from the ^{214}Pb decay, 510–514 keV

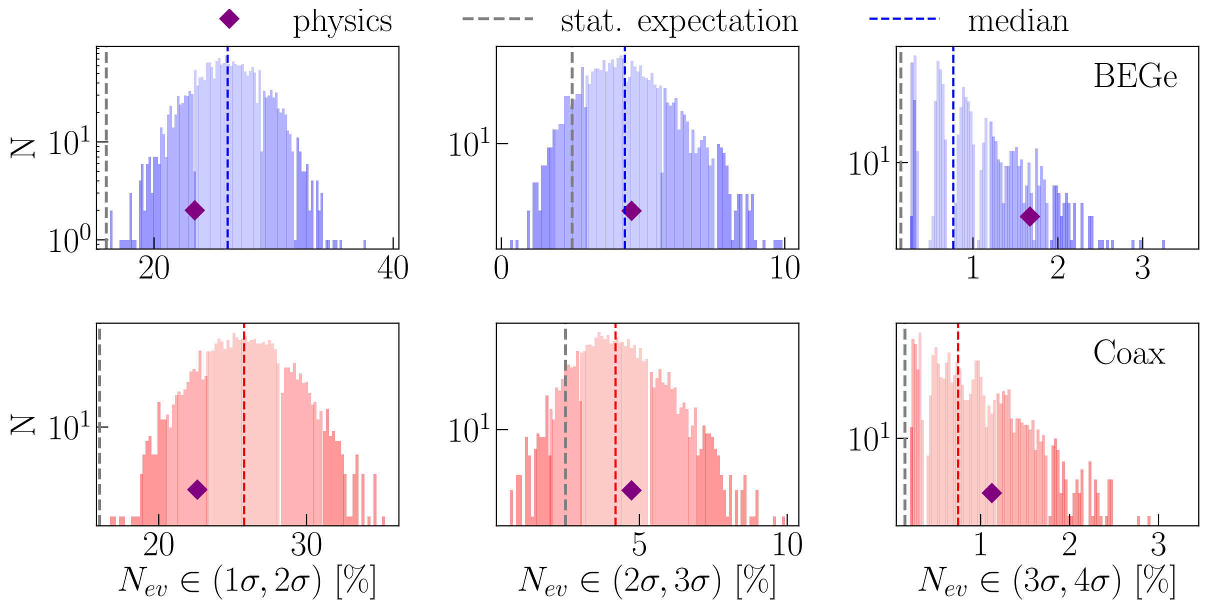

Figure 5.8: Distribution of the number of the limit values above 1σ (left), 2σ (mid.), and 3σ (right) expectation bands estimated from toy-MC data for BEGe (top) and Coax (bottom) datasets. The purple diamonds indicate the values estimated from the physics data analysis.

are due to γ ray form e^+e^- annihilation and ^{85}Kr decay, and 581–856 keV are from the decay of ^{208}Tl. Other cases of the limits being above the 3σ band are understood to be due to statistical fluctuations, and given that the mode is within 5σ at zero counts, no signal can be detected. The fits for those cases are presented in appendix in Fig. D.1 and Fig. D.2 for BEGe and Coax respectively.

5.6 Search for Bosonic Super-WIMPs

The generic peak search analysis described in Section 5.5 enables the search for various exotic physics channels with a peak-like signature. One possibility is to look for a rare interaction of certain dark matter (DM) candidates. A recently postulated example of such candidates is the bosonic Super-WIMP [100]. This type of candidates has weaker coupling to the Standard Model (SM) particles than WIMP candidates [101, 102] and can be cold or warm dark matter, depending on their mass. The theory suggests three types of candidates: vector, scalar, and pseudo-scalar particles. As mentioned in Ref. [100] the phenomenology of scalar SuperWIMP in the case of coupling to photons, which is considered in direct search experiments, is complicated by required fine-tuning of the UV physics; therefore this type of the particle is left out of the scope of the presented analysis.

Super-WIMPs as Axion-like Particles and Dark Photons

Pseudo-scalar Super-WIMPs belong to the class of Axion-Like Particles (ALPs). Axions are hypothetical, ultralight pseudo-scalar bosons, introduced as a possible solution of the violation of P (parity) and CP (charge conjuction-parity) symmetry in the strong interactions [103, 104]. Unlike QCD axions, ALPs are not associated with the strong CP-problem, and can also couple electromagnetically. The Lagrangian for interaction of the ALP field a with photons is [105]:

$$\mathcal{L}_{\mathrm{ALP}} = \frac{1}{2}\partial_\mu a \partial^\mu a - \frac{1}{2}m_a^2 a^2 - \frac{1}{4}g_{ae} a F_{\mu\nu}\tilde{F}^{\mu\nu}, \tag{5.4}$$

where $\tilde{F}^{\mu\nu}$ is the electromagnetic field-strength tensor, and m_a is the ALP's mass, and g_{ae} is the coupling of ALPs to SM photons. The coupling of pseudo-scalars to SM occurs via decay, emission, and absorption. The latter can be detected due to its peak signature. The ALP can be absorbed by one of the electrons in an atom's outer shell, which as a result leaves its shell and deposits energy in the detector volume. The topology of this absorption is identical to the well known photo-electric effect [106], and analogously, this interaction is called the axio-electric effect.

The vector Super-WIMP, also known as a dark photon, belongs to the hidden sector [107]. The weak coupling of the hidden sector particles to SM photon occurs via kinetic mixing, described by the low energy Lagrangian's term as [108]:

$$\mathcal{L}_V = -\frac{\kappa}{2} \cdot V^{\mu\nu} X_{\mu\nu}, \tag{5.5}$$

where $V^{\mu\nu}$ and $X_{\mu\nu}$ are respectively the field strengths of the visible and the hidden sectors, and κ is the kinetic mixing parameter. The photon is then absorbed by the atom's electron, due to photo-electric effect.

In both interactions, the energy of the released electron corresponds to the rest mass of the absorbed particle corrected by the binding energy of an electron to its shell. In germanium detectors, the electron and X-rays from the characteristic cascade in the atom's shells are absorbed within ~1 mm^3 and cannot be resolved in time. Therefore, the signature of these interactions is a peak at an energy corresponding to the mass of the absorbed particle. Given this signature, the count rates obtained in the generic peak search can be interpreted as the interaction rate of the Super-WIMPs with germanium.

Super-WIMP's Interaction Rates

For the vector and pseudo-scalar Super-WIMP absorption with respective masses m_v and m_a, the absorption cross section (σ_{abs}) is expressed via the photo-electric effect cross section (σ_{pe}) for the energy equal to the mass of the absorbed particle as follows:

$$\frac{\sigma_{abs} v}{\sigma_{pe} c} \approx \frac{\alpha'}{\alpha} \quad (5.6) \qquad \frac{\sigma_{abs} v}{\sigma_{pe} c} \approx \frac{3 m_a^2}{4\pi\alpha f_a^2}, \quad (5.7)$$

where v is the incoming velocity of the boson, and c is the velocity of light. The ratio of the fine structure constant and its vector boson analogue defines the kinetic mixing strength, $\kappa^2 \approx \frac{\alpha}{\alpha'}$. The coupling constant of a pseudo-scalar particle to a SM's electron is defined by the dimensional parameter f_a, and for future simplification will be referred to as the dimensionless coupling constant, g_{ae}, as $g_{ae} = 2 m_a f_a^{-1}$.

Assuming that Super-WIMPs are non-relativistic particles constituting the local DM density of 0.3 GeV/cm^3, their interaction rate with a terrestrial detector with atomic number A, can be expressed for the vector and pseudo-scalar Super-WIMPs respectively as [100]:

$$R \approx \frac{4 \cdot 10^{23}}{A} \frac{\alpha'}{\alpha} \left(\frac{keV}{m_v}\right) \left(\frac{\sigma_{pe}}{b}\right) kg^{-1} d^{-1} \quad (5.8)$$

$$R \approx \frac{1.29 \cdot 10^{19}}{A} g_{ae}^2 \left(\frac{m_a}{keV}\right) \left(\frac{\sigma_{pe}}{b}\right) kg^{-1} d^{-1}. \quad (5.9)$$

Given the dependency on the photo-electric effect cross-section, the energy dependent number of events exhibits the characteristic sawtooth edges, corresponding to the absorption edges in the cross-section for photoelectric effect due to the energy threshold for electrons in the L or K shells.

Experimental Search for bosonic Super-WIMP

In the reference postulating the SuperWIMP [100], different constraints on the coupling constants of Super-WIMPs were derived from the observation of the galactic γ ray background, He-burning stars, and the cooling of the supernova SN1987A are discussed. This section provides a brief overview of the experiments contributing to the direct search for the Super-WIMPs. The strongest limits, i.e., excluding bigger parameter space for the coupling constants, were set by the PandaX-II, LUX, and XMASS experiments.

The XMASS experiment [109] utilizes liquid xenon (LXe) detector located at the Kamioka Observatory, Japan. The collaboration presented the results on the pseudo-scalar and vector Super-WIMPs for the mass range of 40 to 120 keV from 800 live-days × 327 kg data collection.

The PandaX-II experiment [110] utilizes LXe dual-phase time-projection chamber (TPC), located at China Jinping Underground Laboratory. The collaboration has set their limits on the

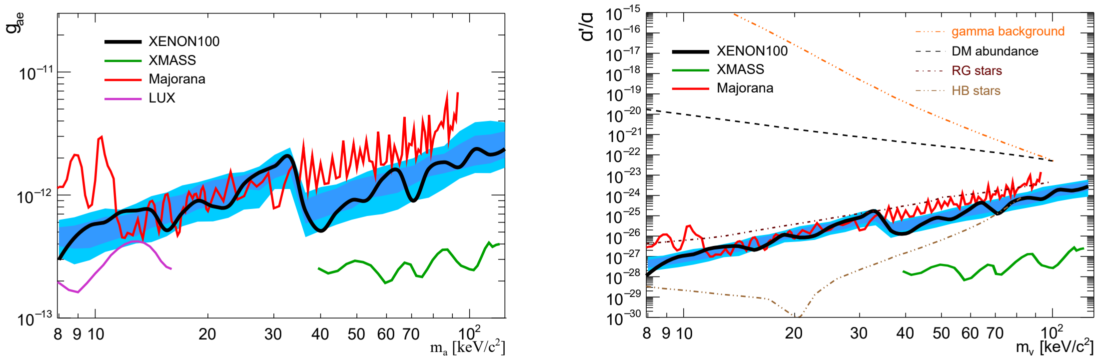

Figure 5.9: The established limits on the coupling constant for pseudo-scalar (left) and vector Super-WIMP (right), presented in [109, 111, 112, 113] and discussed in the current section.

pseudo-scalar Super-WIMPs from $2.7{\cdot}10^4$ kg·day, covering the mass range of 1-10 keV.

The LUX experiment [111] utilizes a LXe dual-phase TPC, located in South Dakota, United States. The collaboration has set their limits on the pseudo-scalar Super-WIMPs from 95 live-days × 118 kg, covering the mass range of 1-16 keV.

Next strongest limit, covering a wider mass range than PandaX, LUX, and XMASS, was set by the XENON100 collaboration [112]. The experiment utilizes a LXe dual-phase TPC, located at the LNGS laboratory, Italy. The collaboration has set their limits from the collected exposure of 224.6 live-days × 34 kg on the Super-WIMP's mass range of 8-125 keV.

The MAJORANA collaboration has set competitive limits to those achieved by the xenon experiments [113]. The Majorana Demonstrator experiment, similarly to GERDA, searches for the $0\nu\beta\beta$ decay of ^{76}Ge (see Section 1.6 in Chapter 1). The significant difference is in the cooling techniques for the germanium crystals. While GERDA deploys LAr, MAJORANA cools the detectors down to their operating temperature using liquid nitrogen. This coolant does not introduce as much background at low energies (below 600 keV) as LAr, and therefore, permits the physics data analysis down ~5 keV. The collected exposure of MAJORANA used for the SuperWIMP search is 478 kg·days, about 50 times lower than what was collected in GERDA.

Fig. 5.9 shows the selected results achieved in the search for the pseudo-scalar and vector Super-WIMPs. While comparing the results from the Majorana collaboration to other experiments, one finds the larger frequency of the fluctuations in the limit, as a result of the width of the expected signal, which is determined by the energy resolution. The typical energy resolution of the xenon detectors is on the order of a few percent, while for the germanium detectors this is at maximum one percent at 100 keV energy.

5.7 Detection Efficiency

The energy from electrons released in the interaction can be partly deposited in the dead layer, thus, not fully absorbed. To account for possible losses, the efficiency to detect a Super-WIMP with a certain mass m_a, corresponding to energy E_0, was estimated for BEGe and Coax dataset as follows:

$$\epsilon_{tot} = \sum_{i}^{N_{det}} \frac{(M \cdot t)_i}{(M \cdot t)} \cdot \frac{M_{av,i}}{M_{tot,i}} \cdot \epsilon_{fep,i}(E = E_0) \cdot \epsilon_{phy\_cuts}, \tag{5.10}$$

where the index i runs over the individual detectors of that dataset, containing N$_{det}$ detectors. The components of the above equation are:

- $(M \cdot t)_i$ is detector's exposure; $(M \cdot t)$ is the total dataset's exposure.
- $\frac{M_{av,i}}{M_{tot,i}}$ is the active mass fraction, taken from Ref. [114].
- ϵ_{phy_cuts} is the efficiency of the quality cuts. For the Phase II this efficiency is taken as 100% as in Ref. [115].
- $\epsilon_{fep,i}$ is the efficiency for the full energy absorption of an electron emitted in the interaction. A dedicated study of this efficiency was performed for this analysis and presented in the following subsection.

Table 5.3 presents average full energy absorption and total efficiencies at the start and end energy value for the Super-WIMP search. The detectors, their exposure, respective detector mass and estimated efficiency for the full energy absorption are listed in Table 5.4. The following physics analysis is performed on the count rate corrected according to the efficiencies of the experiment.

Table 5.3: Summary of the estimated efficiencies. The average value among the detectors from one data set is shown for $\epsilon_{fep,i}$ at energies 120 keV and 1000 keV. The $\epsilon_{tot.}$ is the total efficiency estimated according to Eq. (5.10).

Dataset	$\langle\epsilon_{fep}\rangle$|E= 120 keV	$\langle\epsilon_{fep}\rangle$|E= 1000 keV	ϵ_{tot}|E= 120 keV	ϵ_{tot}|E= 1000 keV
BEGe	100.0%	95.1%	87.6%	83.7%
Coax	100.0%	96.2 %	86.2%	83.2%

Table 5.4: Efficiencies for the signal detection. From left to right: detector's mass, mass of the active volume, parameters of the energy-dependent efficiency of the electron full energy absorption, detector's exposure. The horizontal lines throughout the table separate detectors from different strings.

Detector	M_{tot}	M_{active}	$\epsilon_{fep,i}(E) = p_0 + p_1 \cdot E$		$(M \cdot t)_i$
	[g]	[g]	p_0	$p_1 \cdot 10^5$ [1/keV]	[kg·yr]
GD91A	627.00	557(11)	1.00	-5.36	1.10
GD35B	810.00	740(12)	1.00	-4.83	1.40
GD02B	625.00	553(11)	1.00	-5.22	1.20
GD00B	697.00	613(13)	1.00	-5.13	1.20
GD61A	731.00	652(13)	1.00	-4.82	1.30
GD89B	620.00	533(13)	1.00	-5.76	0.60
GD02D	662.00	552(11)	1.00	-5.43	0.00
GD91C	627.00	556(12)	1.00	-5.53	0.20
ANG5	2746.00	2281(132)	1.00	-3.88	5.00
RG1	2110.00	1908(125)	1.00	-3.90	3.80
ANG3	2391.00	2070(136)	1.00	-4.02	4.50
GD02A	545.00	488(9)	1.00	-5.48	1.00
GD32B	716.00	632(11)	1.00	-4.96	1.20
GD32A	458.00	404(11)	1.00	-5.51	0.50
GD32C	743.00	665(11)	1.00	-4.76	1.40
GD89C	595.00	520(13)	1.00	-5.56	1.00
GD61C	634.00	562(11)	1.00	-5.46	1.00
GD76B	384.00	326(8)	1.00	-5.82	0.70
GD00C	815.00	727(15)	1.00	-5.08	1.40
GD35C	634.00	572(10)	1.00	-5.46	1.20
GD76C	824.00	723(13)	1.00	-4.72	1.30
GD89D	526.00	454(10)	1.00	-5.87	0.90
GD00D	813.00	723(14)	1.00	-4.82	1.50
GD79C	812.00	713(12)	1.00	-4.94	1.20
GD35A	768.00	693(13)	1.00	-4.64	1.40
GD91B	650.00	578(11)	1.00	-5.20	0.40
GD61B	751.00	666(13)	1.00	-5.47	1.10
ANG2	2833.00	2468(145)	1.00	-3.81	4.70
RG2	2166.00	1800(115)	1.00	-3.95	3.90
ANG4	2372.00	2136(135)	1.00	-3.91	4.40
GD00A	496.00	439(9)	1.00	-5.78	0.90
GD02C	788.00	700(14)	1.00	-4.80	1.40
GD79B	736.00	648(14)	1.00	-5.08	0.80
GD91D	693.00	615(13)	1.00	-4.92	1.00
GD32D	720.00	657(11)	1.00	-4.87	1.20
GD89A	524.00	462(10)	1.00	-5.41	1.00
ANG1	958.00	795(50)	1.00	-5.24	1.80
GTF112	2965.00	2522(0)	1.00	-3.03	0.00
GTF32	2321.00	2251(116)	1.00	-3.02	0.00
GTF45_2	2312.00	1965(0)	1.00	-3.16	0.00

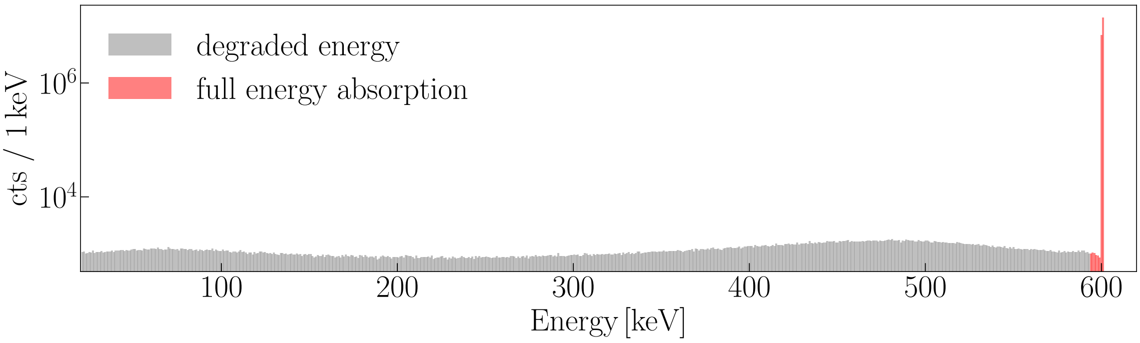

Figure 5.10: Energy distribution of simulated events with initial energy of 600 keV. The efficiency of the full energy absorption is defined as the number of events with negligible energy loss (red) to the total number of simulated events including the ones with the significant energy loss due to ionization or Bremsstrahlung (grey).

Electron Detection Efficiency

Detection of an electron emitted in the interaction depends on its probability to deposit all its energy in the active volume of the detectors. In some cases, the electron can partly deposit energy on the n^+ electrode or lose energy by generating Bremsstrahlung while scattering in the Coulomb field of a nucleus. As the fraction of the energy lost due to Bremsstrahlung increases with energy, the efficiency to fully absorb the electron's energy is an energy-dependent function.

The full-energy absorption efficiency was estimated from the simulation 10^8 electron interactions within the detector for each electron energy in the range between 600 keV and 1000 keV. For energies outside of this range, the efficiency was estimated by extrapolation.

The simulations were performed with the MAGe framework [116], which is the GERDA simulation software based on GEANT 4 [117]. From Monte Carlo data, only events with energy deposition in the active volume of detectors were recorded.

The detected energy for most of the simulated events is close to the energy of generated electrons E_{e^-}, except a tiny fraction, which fills the energy histogram throughout its range until a peak at the energy of E_{e^-}, Fig. 5.10. The efficiency to absorb the full energy of an electron is defined as a fraction of the electrons with effectively zero loss of energy to the number of all electrons sampled in the active volume of the detector ($N_{AV}^{e^-}$):

$$\epsilon_{fep,i}(E = E_{e^-}) = \frac{\int_{0.99E_{e^-}}^{E_{e^-}} N(E)}{N_{AV}^{e^-}},$$

where N(E) is histogram's entries in the bin with the center at energy E. From the evaluated at each energy efficiency, an energy-dependent function was extracted detector-wise.

Fig. 5.11 demonstrates the efficiency estimated detector-wise, where the detectors from the Coax dataset exhibit the higher values. Table 5.4 summarizes the parameters (p_0, p_1) of the efficiency function. At 120 keV, start point of the analysis, the full energy absorption efficiency was estimated at 100.0%, while at 1000 keV at 95.1% and 96.2% on average for BEGe and Coax datasets, respectively.

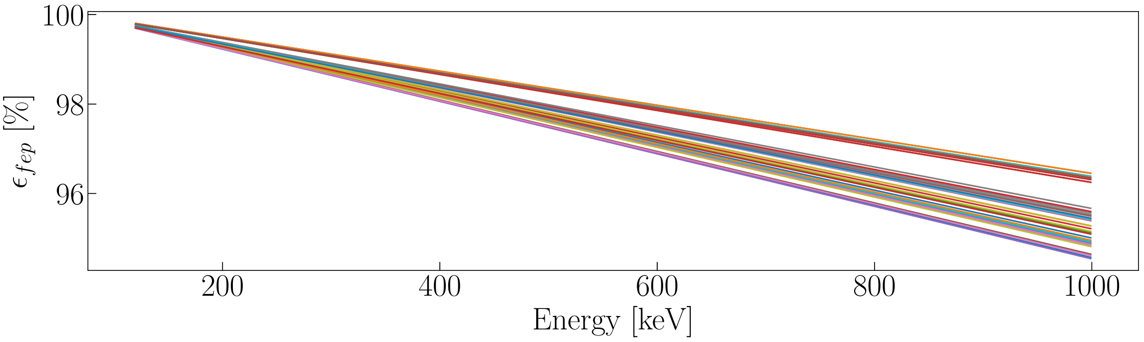

Figure 5.11: Energy-dependent efficiency for the full energy absorption of an electron estimated detector-wise, where the higher values are from the enriched coaxial detectors. Legend for 37 enriched detectors is omitted from the plot for clarity.

5.8 Coupling Constants Constraint

The count rate estimated in Section 5.5 was used to set the constraints on the coupling of the bosonic Super-WIMPs to the SM particles. First, the efficiencies on the electron signal detection were accounted for BEGe and Coax datasets, as described in Section 5.7. Second, the results of the count rate were combined at each energy with the exposure weighting:

$$R = \frac{R_B \cdot \epsilon_B + R_C \cdot \epsilon_C}{\epsilon_B + \epsilon_C}, \tag{5.11}$$

where $R_{B(C)}$ and $\epsilon_{B(C)}$ are respectively the count rate and exposure for BEGe (Coax) dataset. For events with energies below and above 200 keV, different exposure values were used, as summarized in Table 5.1. At the final step, the combined upper limits on the coupling constants for pseudo-scalar and vector Super-WIMPs were estimated from the count rate limits according to Eq. (5.8) and 5.9.

Fig. 5.12 depicts the limits on the coupling constants for the vector and pseudo-scalar Super-WIMPs. The small "bumps" in the Gerda values are due to the presence of the background gamma lines, which weaken the established limit, as discussed in Section 5.3. In the investigated mass range the contribution from 11 γ lines is expected according to the background model as explained in Chapter 4. The energies at which the limit is above the model expectation bands, estimated from the analysis of the MC dataset, are attributed to the background γ lines (see Table D.1 and discussion in Section 5.5). The limits estimated separately for BEGe and Coax datasets are illustrated in the appendix, in Fig. E.1 and Fig. E.2.

The direct detection experiments explored the mass region up to 120 keV, with the best limits quoted by the XMASS collaboration [109]. Gerda is complementary to other experiments in the search for bosonic Super-WIMP since it covers different mass range, from 120 keV to 1000 keV, Fig. 5.12. The limitations to exploring lower energies are discussed in Section 5.1.

5.9 Conclusion

The data collected between December 2015 and April 2018 were analyzed to search for the signature of bosonic Super-WIMPs. In the analyzed energy range, no clear signal was observed,

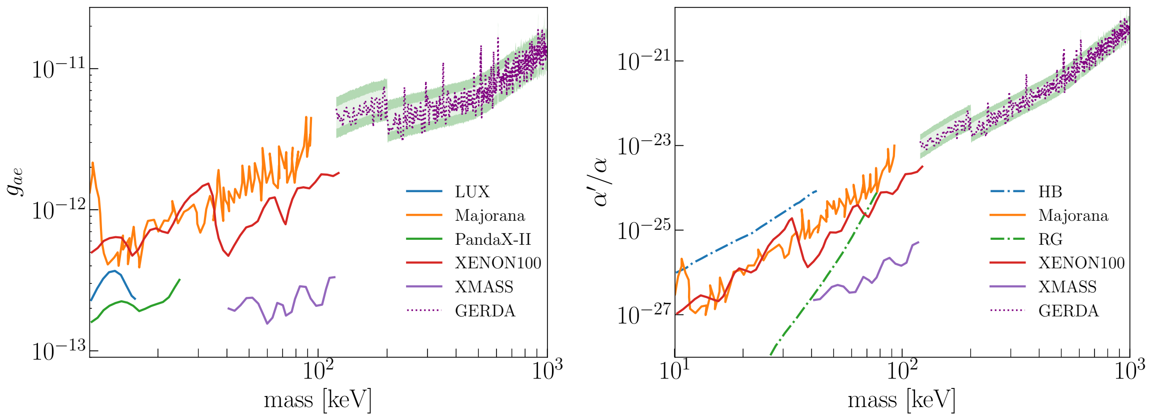

Figure 5.12: Established 90% C.I. upper limits on the pseudo-scalar (left) and vector (right) Super-WIMPs from the analysis of the GERDA data; the physics values are shown with purple dashed, and the model expectation assuming no signal - with the green bands. The comparison with the previously established limits by the direct DM search experiments, and also the Majorana collaboration, are shown accordingly to the legend. The limits on the vector Super-WIMPs from indirect detection (He-burning (HB) and red giant (RG) stars) are marked with the dashed pattern.

and 90% C.I. upper limits were set on their coupling constants. The novelty of the GERDA results is the covered mass range, from 120 keV to 1000 keV, which has not been previously investigated for this type of dark matter candidates.

The count rates on the Super-WIMPs interaction were extracted from a generic peak search analysis. The analysis was performed over the energy range of 120 -5200 keV, by looking for a peak-like signature that can not be described by known background components. In the above-mentioned energy range, no signal was observed, and the upper limits on the count rates were established. The obtained results are well compatible with statistical expectations on the count rate studied with the Monte Carlo simulated data. The results of the generic peak search provide a detailed understanding of the GERDA data and can be interpreted in terms of other searches for new physics.

Chapter 6

Conclusions

This dissertation has been developed in the context of the GERDA experiment, within the Phase II of data collection. The presented work contributed to the experiment with the analysis of weekly calibrations of the germanium detectors during the first two years of the data taking. Within this time, 47 calibration runs were analyzed, and for each of the two main energy estimators (Gauss and ZAC), the parameters to calibrate the physics data were estimated. Parameters extracted with the Gauss estimator were used to monitor the stability of the energy scale over those two years. By identifying instabilities due to known reasons, a dataset for the physics data analysis, in particular for the $0\nu\beta\beta$ decay search, was selected. The energy spectrum based on the ZAC energy estimator is used to search for the $0\nu\beta\beta$ decay. For the combined dataset, the effective energy resolution for both types of enriched detectors (BEGe and coaxial) was evaluated. The FWHM at $Q_{\beta\beta}$ was determined at (2.95±0.06) keV and (3.9±0.1) keV for BEGe and coaxial detectors, respectively.

To contribute to the modeling of the background for the $0\nu\beta\beta$ decay search, the γ background in the collected physics data was studied. The results served as an effective crosscheck for the experimental background model. An extensive comparison with the γ background rates estimated for Phase I of GERDA shows an increase in the background lines due to ^{40}K and ^{42}K decays, which can be explained by the enlarged number of the signal cables and modified system for the mitigation of ^{42}K background. A significant decrease in the rates from the uranium and thorium chains confirms the success of the collaboration in constructing the experimental setup using the most radio-pure materials selected via radioassays.

Finally, the acquired data was thoroughly studied on the presence of peak signals incompatible with the known background. The search was performed over a large energy range between 120 keV and 5200 keV. The results showed no indications for such peak signals, and the 90% upper limits were set. This analysis was used to search for Super-WIMPs, keV-scale dark matter candidates. For the first time, the coupling strength of these elusive particles was limited between 120 keV-1000 keV mass range.

Appendix A

Exposure of the Detectors

Table A.1: The exposure gained for each detector during the period between December 2015 and April 2107. The values were used to estimate the energy resolution at $Q_{\beta\beta}$. The last three detectors in the table are of the coaxial type with a natural abundance of ^{76}Ge and by setting their exposure to zero value, they are excluded from the combined calibration analysis.

Nr.	Detector	exposure (kg·yr)	Nr.	Detector	exposure (kg·yr)
0	GD91A	0.7	20	GD76C	0.8
1	GD35B	0.8	21	GD89D	0.5
2	GD02B	0.7	22	GD00D	0.9
3	GD00B	0.7	23	GD79C	0.6
4	GD61A	0.76	24	GD35A	0.8
5	GD89B	0.6	25	GD91B	0.4
6	GD02D	0.0	26	GD61B	0.6
7	GD91C	0.2	27	ANG2	2.5
8	ANG5	2.9	28	RG2	2.3
9	RG1	2.2	29	ANG4	2.6
10	ANG3	2.6	30	GD00A	0.5
11	GD02A	0.6	31	GD02C	0.8
12	GD32B	0.7	32	GD79B	0.6
13	GD32A	0.5	33	GD91D	0.5
14	GD32C	0.8	34	GD32D	0.7
15	GD89C	0.6	35	GD89A	0.6
16	GD61C	0.6	36	ANG1	1.0
17	GD76B	0.4	37	GTF112	0.0
18	GD00C	0.85	38	GTF32	0.0
19	GD35C	0.7	39	GTF45	0.0

Appendix B

Optimisation of the Calibration Software

The number of germanium detectors in GERDA keeps evolving over its physics program. By the end of the Phase I, only 11 detectors were deployed, but at the beginning of the PhaseII, the number of detectors increased to 40. For the future LEGEND 200 experiment, the number of detector channels is planned to be increased by more than one order of magnitude. This causes an increasing workload of calibration data analysis.

According to the experience, the runtime of calibration software scales linearly with the increase of the number of the detectors. With the 40 detectors deployed for the Phase II the program's runtime reached several hours. Taking in addition, possible tests of the settings or configurations of the cuts, that became not acceptable for fast and robust analysis of the calibration data.

To make the software runtime independent of the data quantity, a campaign regarding the calibration framework optimization was organized. For this, time performance at each algorithmic step was investigated, and the most time-intensive parts were optimized by enabling the parallel processing of the calibration data. The flow chart of the parallelized software version is provided in Fig. B.1. The changes in time performance are presented in Table B.1.

The parallelization was most importantly applied to the part of the quality cuts application. Now instead of the applying the quality cuts on the entire set of the calibration data at once, this is performed in parallel for each calibration data file, that contains only 5 mins of the data taking vs. three hours for the entire dataset. The survived events from each data file are stored as a histogram. In the final steps, those histograms are combined for the later stages of the calibration analysis procedure, such as peak search and following peak fits.The parallelization of the software gave a boost in the performance from initial 5 h to the 30 mins for the parallel version.

Table B.1: Estimated time performance for the series and parallel software versions for certain parts of the algorithms.

	time span	
Algorithm	series version	parallel version (per one job process)
Events selection	2 hours	5 min
Filling the histograms and preliminary peak search	2 hours	5 min
Final peak search and results check	1-2 hours	10 min

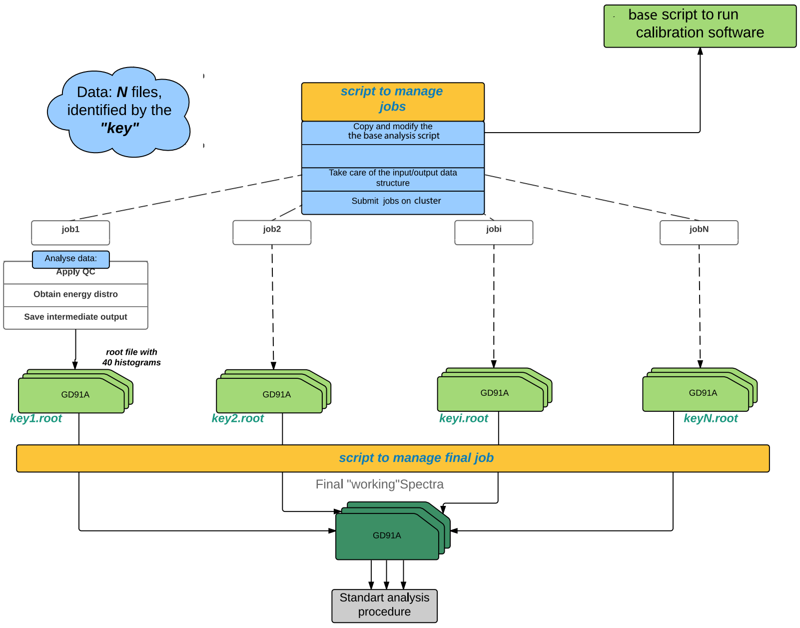

Figure B.1: Flow chart of the parallelized software version.

Appendix C

Spectral Contribution of the Gamma Lines

Uranium Decay Chain

^{234m}Pa

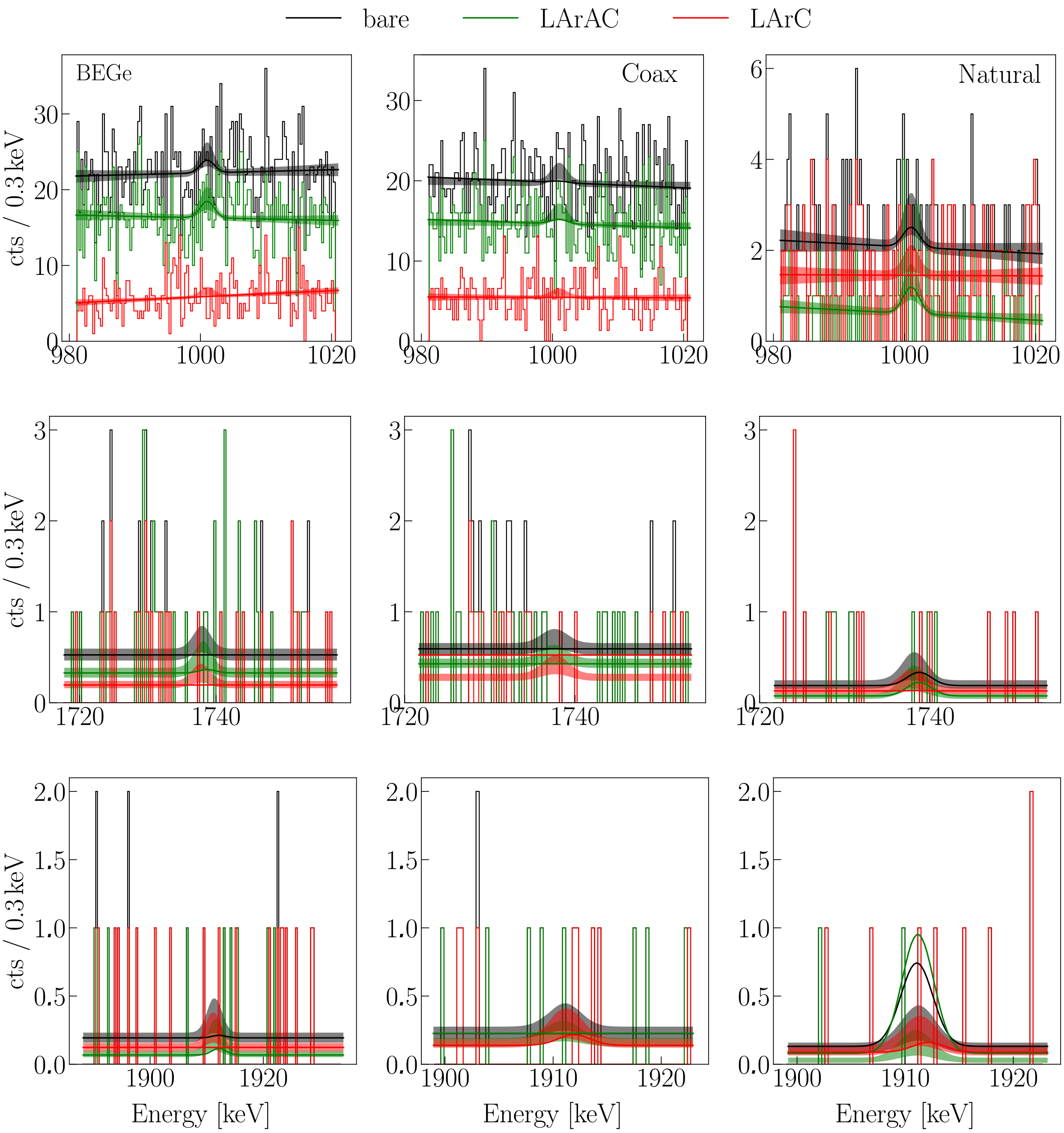

Figure C.1: Fits and energy distributions around the γ lines expected due to ^{234m}Pa for the BEGe (left), Coax (middle), and Natural (right) data sets. The highest intensity of the γ-emission corresponds to the decay with the emission of 1001 keV gamma, which the most present on the spectra.

^{214}Pb

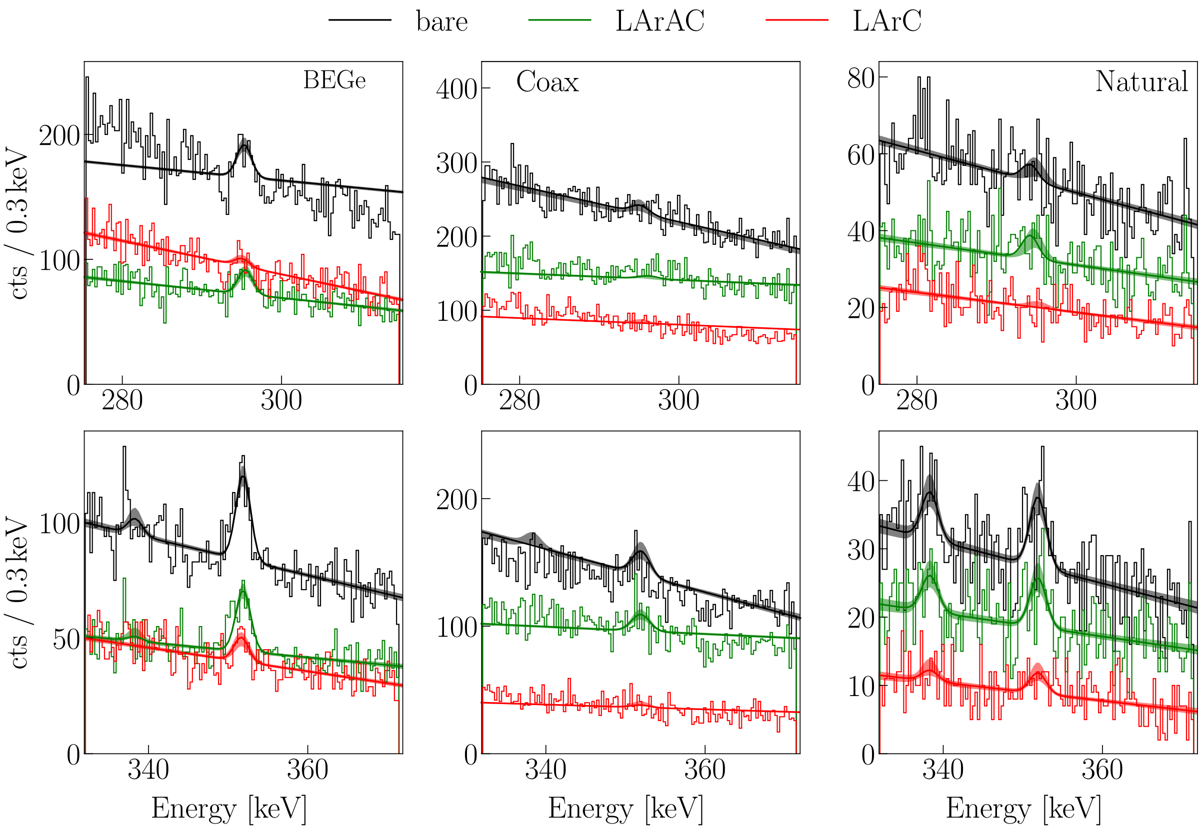

Figure C.2: Fits and energy distributions around the γ lines expected due to ^{212}Pb decay. In case when the counts for another γ line in the fit window are above the background fluctuation, the second Gaussian function is added to the model.

^{214}Bi

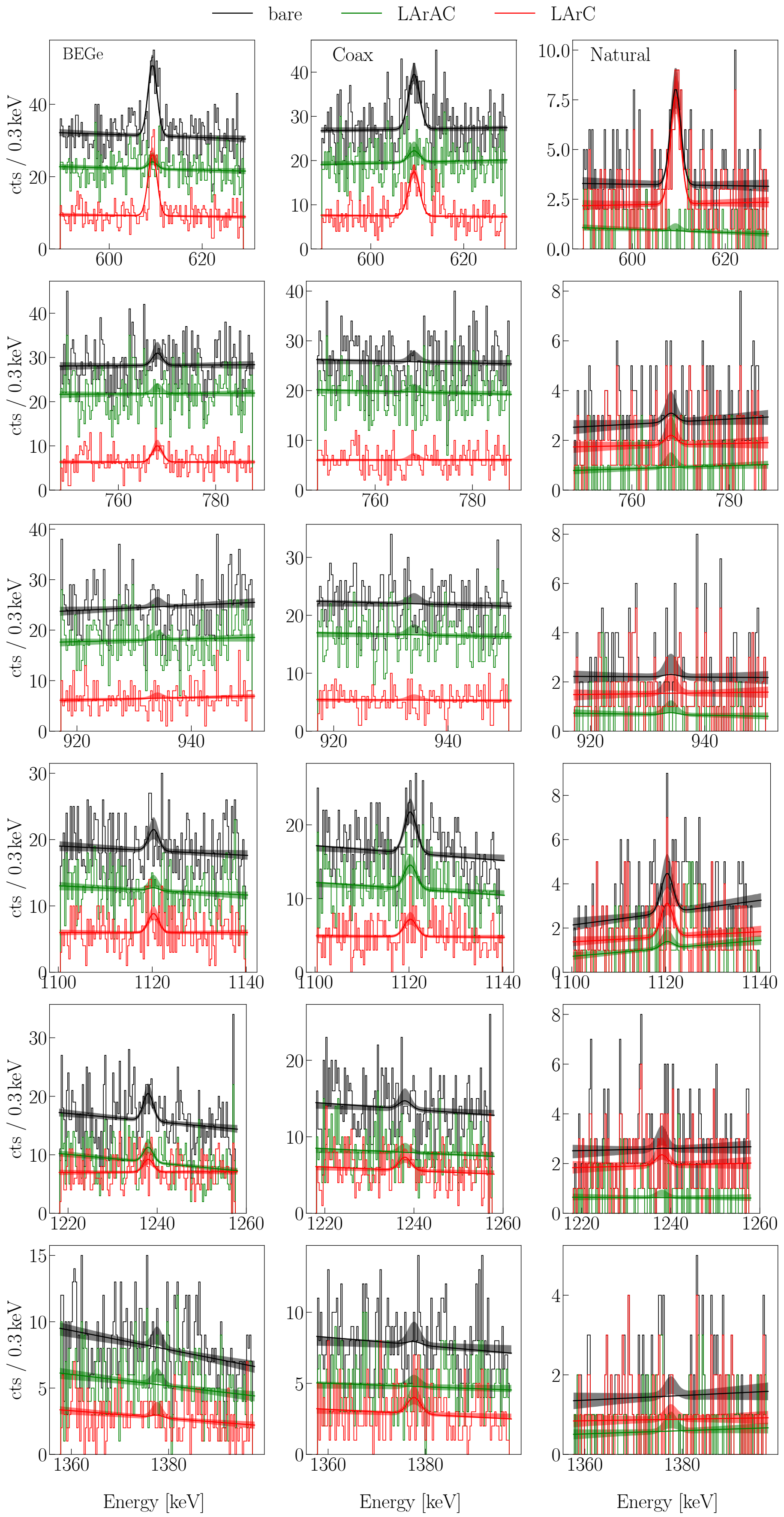
bare
LArAC
LArC
BEGe
Coax
Natural
cts / 0.3 keV
Energy [keV]
600
620
760
780
920
940
1100
1120
1140
1220
1240
1260
1360
1380
0
10
20
30
40
0.0
2.5
5.0
7.5
10.0
2
4
6
8
5
15

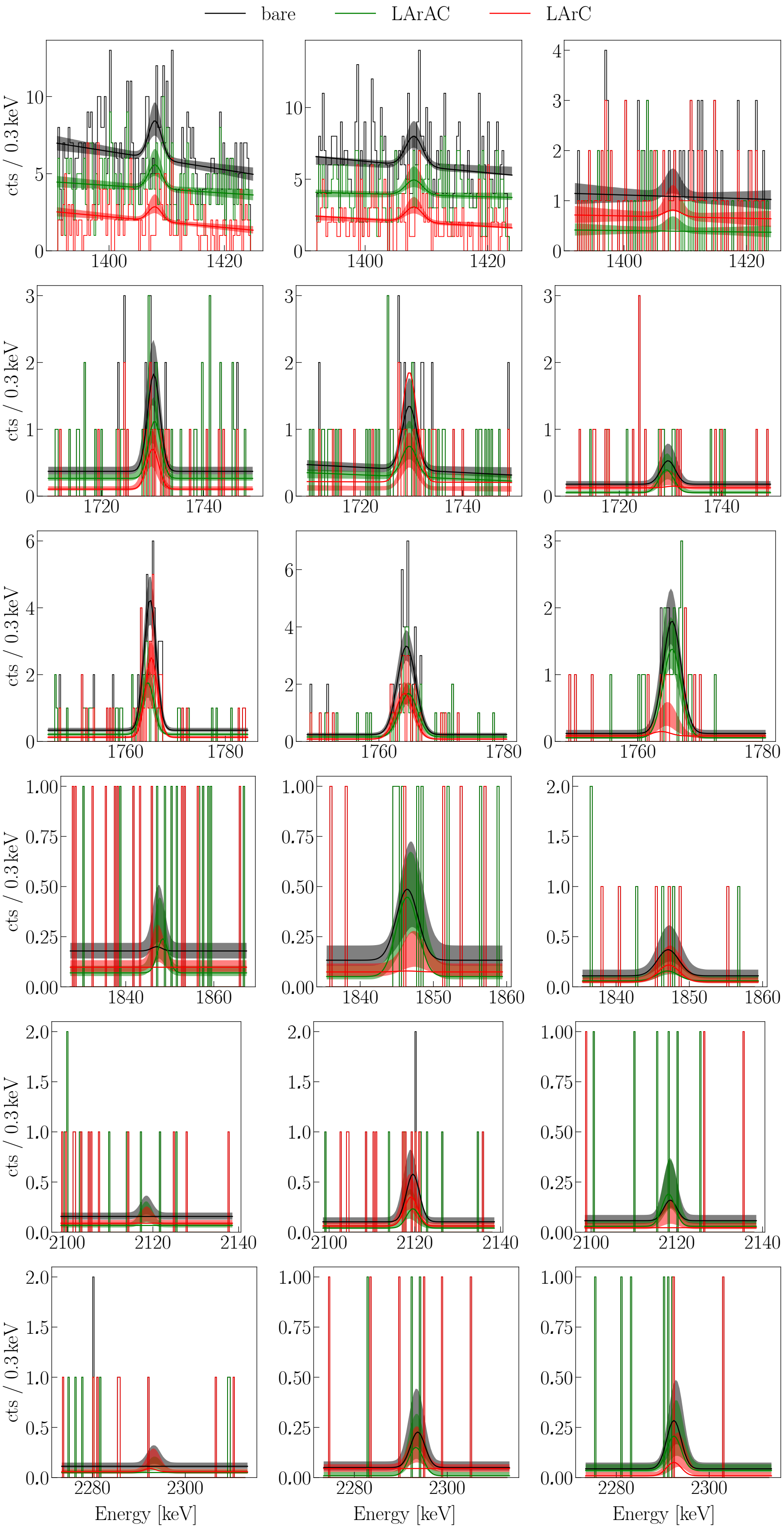
bare
LArAC
LArC
cts / 0.3 keV
1400
1420
1720
1740
1760
1780
1840
1850
1860
2100
2120
2140
2280
2300
Energy [keV]

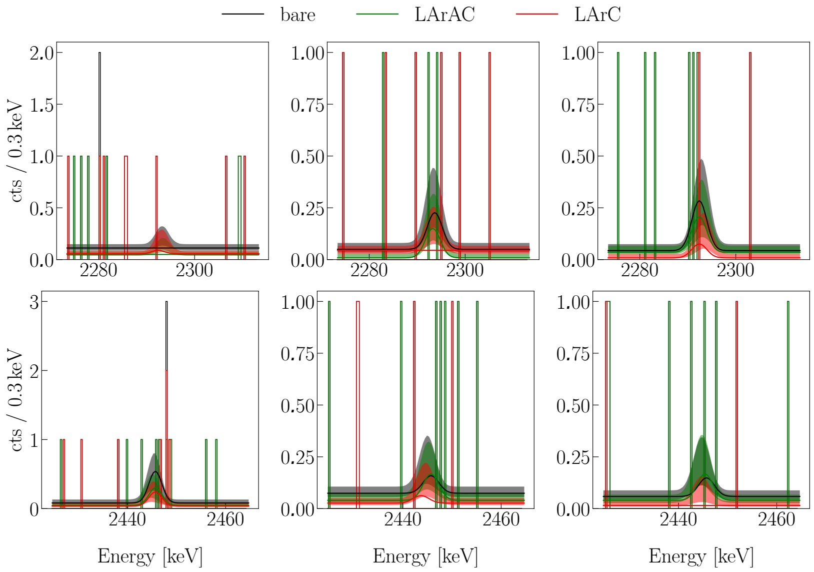

Figure C.3: Fits and energy distributions around the γ lines expected due to ^{214}Bi in the GERDA spectra.

Thorium Decay Chain

^{228}Ac

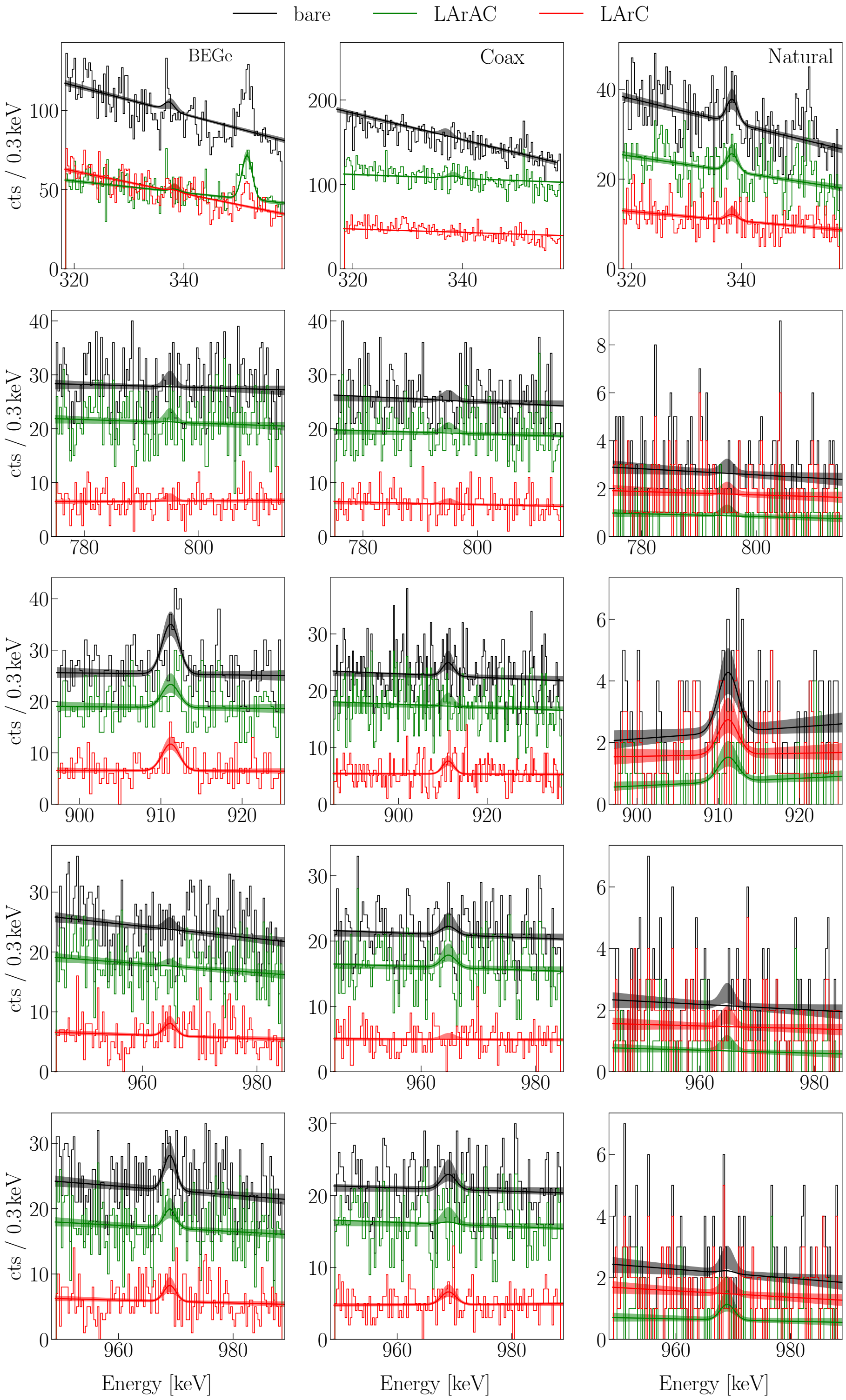

Figure C.4: Fits and energy distributions around the γ lines expected due to ^{228}Ac visible in the GERDA spectra .

^{208}Tl

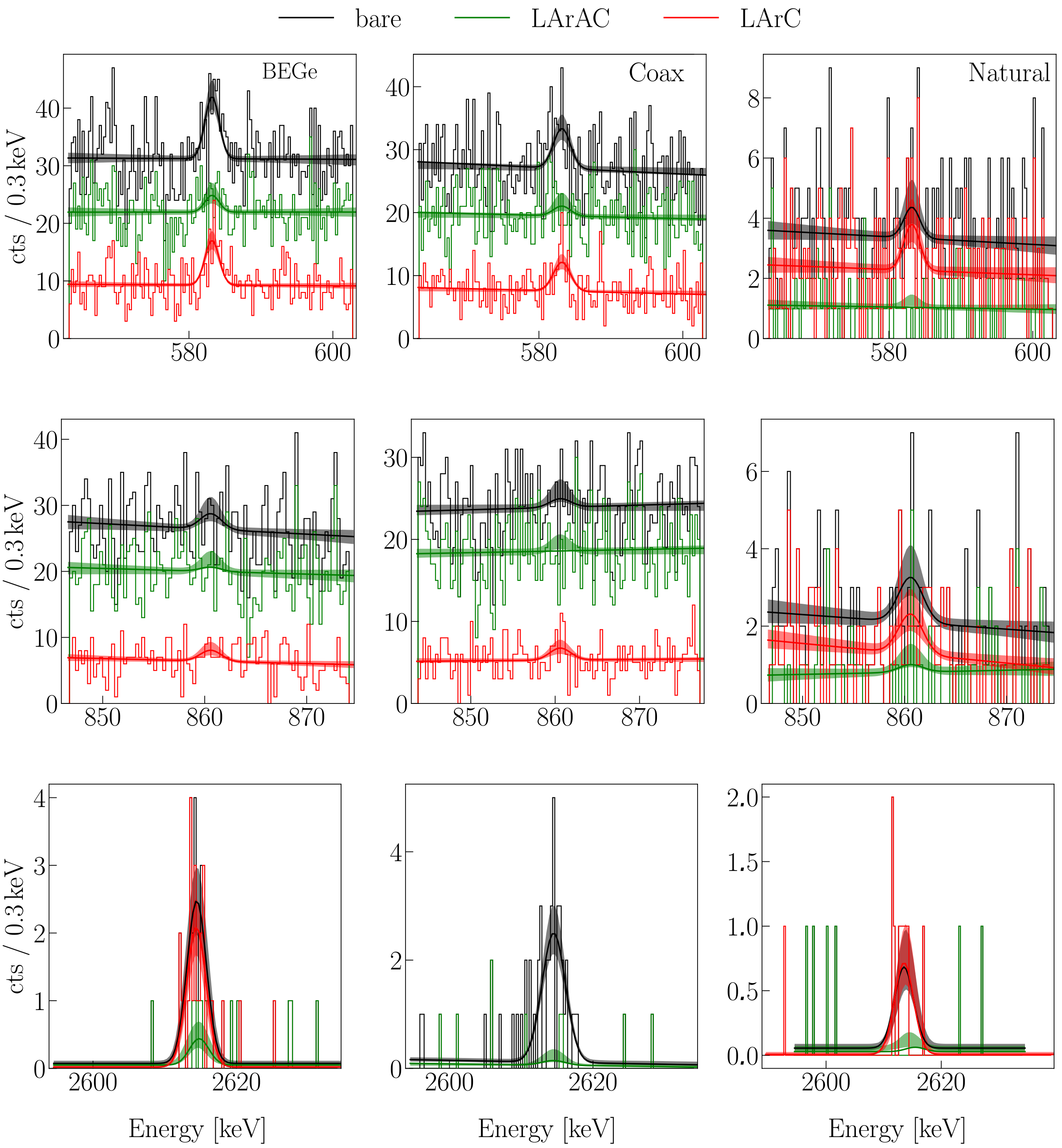

Figure C.5: Fits and energy distributions around the γ lines expected due to ^{208}Tl visible in the GERDA spectra.

^{212}Bi

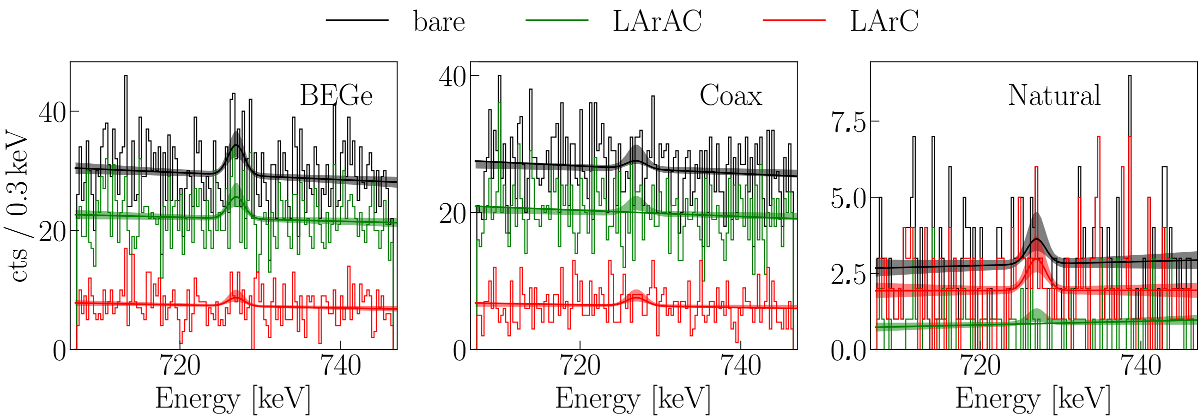

Figure C.6: Fits and energy distributions around the γ lines expected due to ^{212}Bi decay.

Anthropogenic Background Components

^{108m}Ag

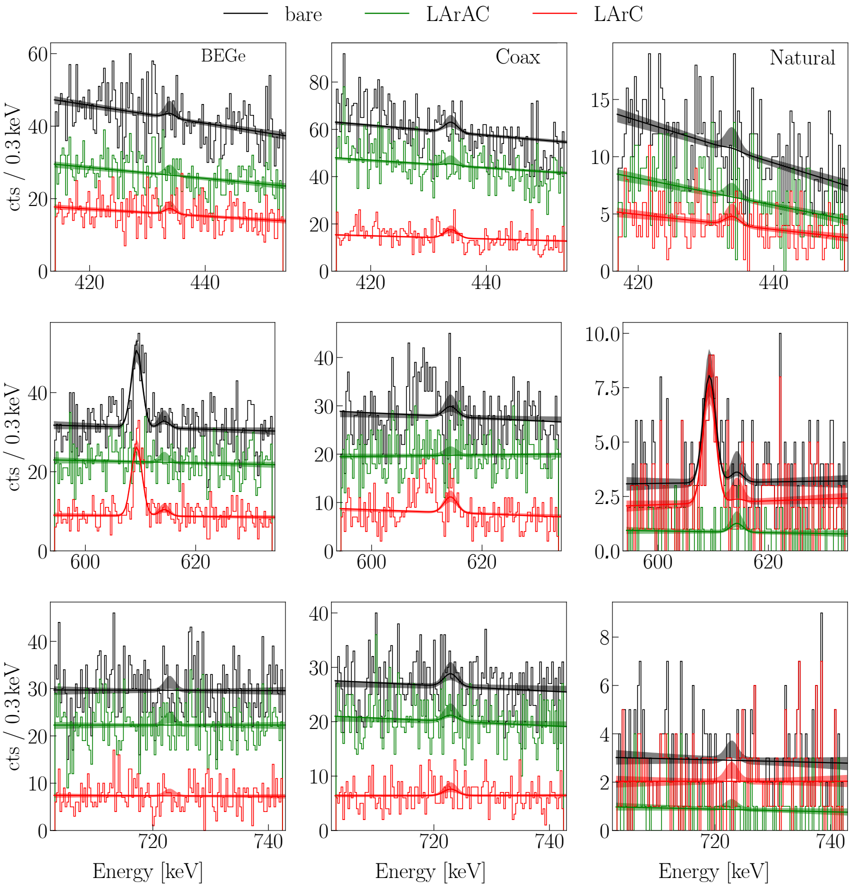

Figure C.7: Fits and energy distributions around the γ lines expected due to ^{108m}Ag visible in the GERDA spectra. For the fit of the line at 614 keV additional contribution from ^{214}Bi was included as a Gaussian function.

^{137}Cs

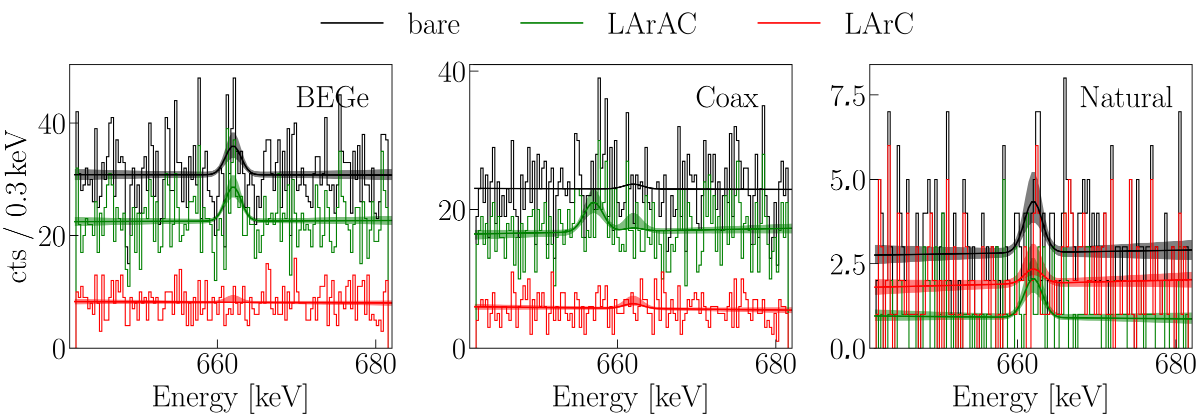

Figure C.8: Fits and energy distributions around the γ lines expected due to ^{137}Cs visible in the GERDA spectra.

^{60}Co

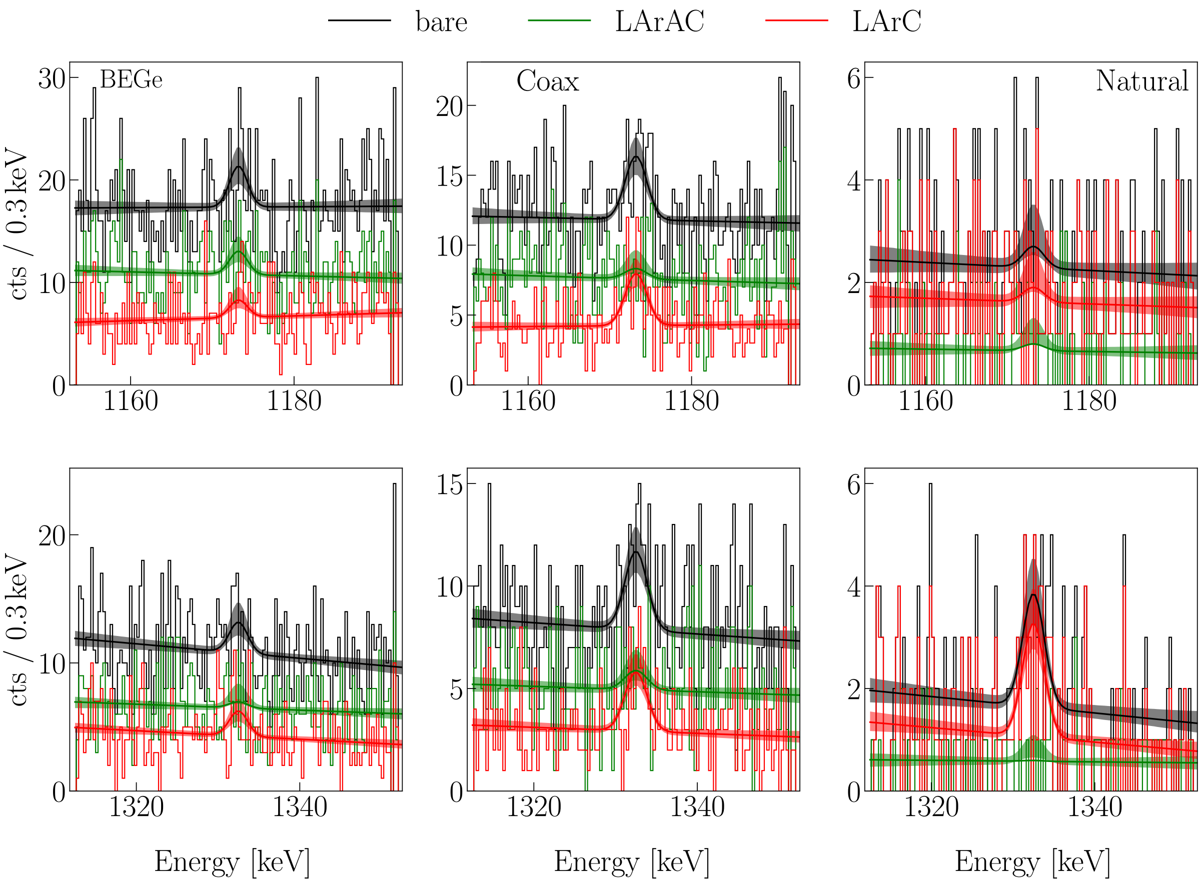

Figure C.9: Fits and energy distributions around the γ lines expected due to ^{60}Co decay visible in the GERDA spectra.

Annihilation Peak

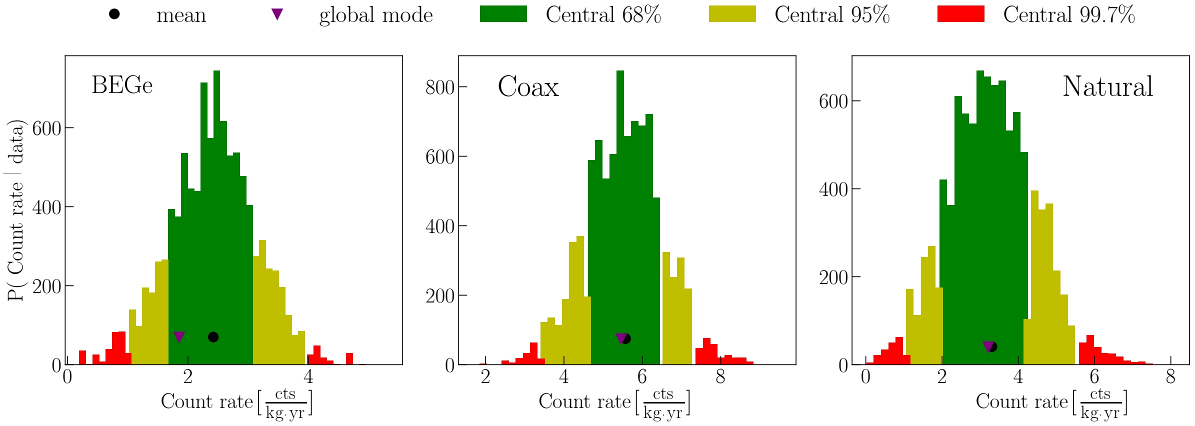

Figure C.10: Marginalised posterior distribution for the count rate of the annihilation peak shown to clarify asymmetric errors on the count rate in Section 4.5.3. The global mode is indicated with the black circle marker, and the mean with the purple triangle marker various colors of the pdfs indicate 68%, 95%, and 99.7% quantiles.

Appendix D

Peak Search Analysis

Table D.1 and Table D.2 summarize the list of the energies where limit exceed 3σ for the BEGe and Coax datasets, respectively. Fig. D.1 and Fig. D.2 illustrate the fits at energies that do not correspond to any background γ lines and not listed in Table 5.2.

Table D.1: Energies and corresponding expectation values, where the established limit exceeds 3σ band for the BEGe dataset.

Dataset	Energy keV	90% C.I limit cts	median expectation value cts	3σ band cts
BEGe	238	16.5	4.1	[1.6 ; 10.1]
	239	13.7	4.1	[1.6 ; 9.5]
	295	9.6	2.8	[1.1 ; 6.4]
	351	11.5	2.0	[0.9 ; 5.0]
	352	11.0	1.9	[0.8 ; 4.9]
	479	3.7	1.3	[0.5 ; 3.3]
	511	3.6	1.3	[0.5 ; 3.3]
	514	6.8	1.3	[0.5 ; 3.1]
	583	4.0	1.3	[0.5 ; 3.0]
	584	4.1	1.2	[0.5 ; 3.3]
	1204	2.9	0.9	[0.3 ; 2.4]
	1205	2.7	0.9	[0.3 ; 2.2]
	3636	0.3	0.1	[0.1 ; 0.3]
	4543	0.3	0.2	[0.1 ; 0.3]
	4544	0.4	0.2	[0.1 ; 0.3]
	4771	0.5	0.2	[0.1 ; 0.4]
	4772	0.4	0.2	[0.1 ; 0.4]
	4773	0.4	0.2	[0.1 ; 0.4]
	4996	0.6	0.2	[0.1 ; 0.5]
	4997	0.6	0.2	[0.1 ; 0.5]
	4998	0.6	0.2	[0.1 ; 0.5]
	4999	0.5	0.2	[0.1 ; 0.5]

Table D.2: Energies and corresponding expectation values, where the established limit exceeds 3σ band for the Coax dataset.

Dataset	Energy keV	90% C.I limit cts	median expectation value cts	3σ band cts
Coax	171	32.9	16.3	[6.2;40.8]
	296	6.8	3.5	[1.3;8.2]
	299	7.5	3.4	[1.3;8.5]
	300	7.6	3.4	[1.3;8.4]
	350	5.8	2.7	[1.2;6.5]
	351	8.0	2.6	[1.1;7.7]
	352	7.2	2.7	[1.0;6.4]
	366	5.1	2.5	[1.0;6.2]
	367	5.6	2.4	[1.0;5.9]
	510	3.7	1.4	[0.5;3.6]
	511	6.9	1.4	[0.6;3.4]
	512	3.0	1.4	[0.6;3.2]
	513	3.5	1.3	[0.5;3.5]
	514	6.6	1.4	[0.6;3.4]
	537	2.7	1.3	[0.6;3.2]
	538	3.0	1.3	[0.6;3.2]
	558	2.9	1.3	[0.5;3.2]
	559	2.7	1.3	[0.5;3.2]
	570	2.7	1.3	[0.6;3.1]
	581	2.9	1.3	[0.5;3.3]
	582	4.0	1.3	[0.5;3.1]
	583	3.9	1.3	[0.5;3.4]
	754	2.8	1.3	[0.6;3.2]
	755	2.7	1.3	[0.5;3.3]
	856	2.6	1.3	[0.5;3.1]

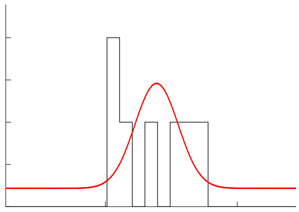

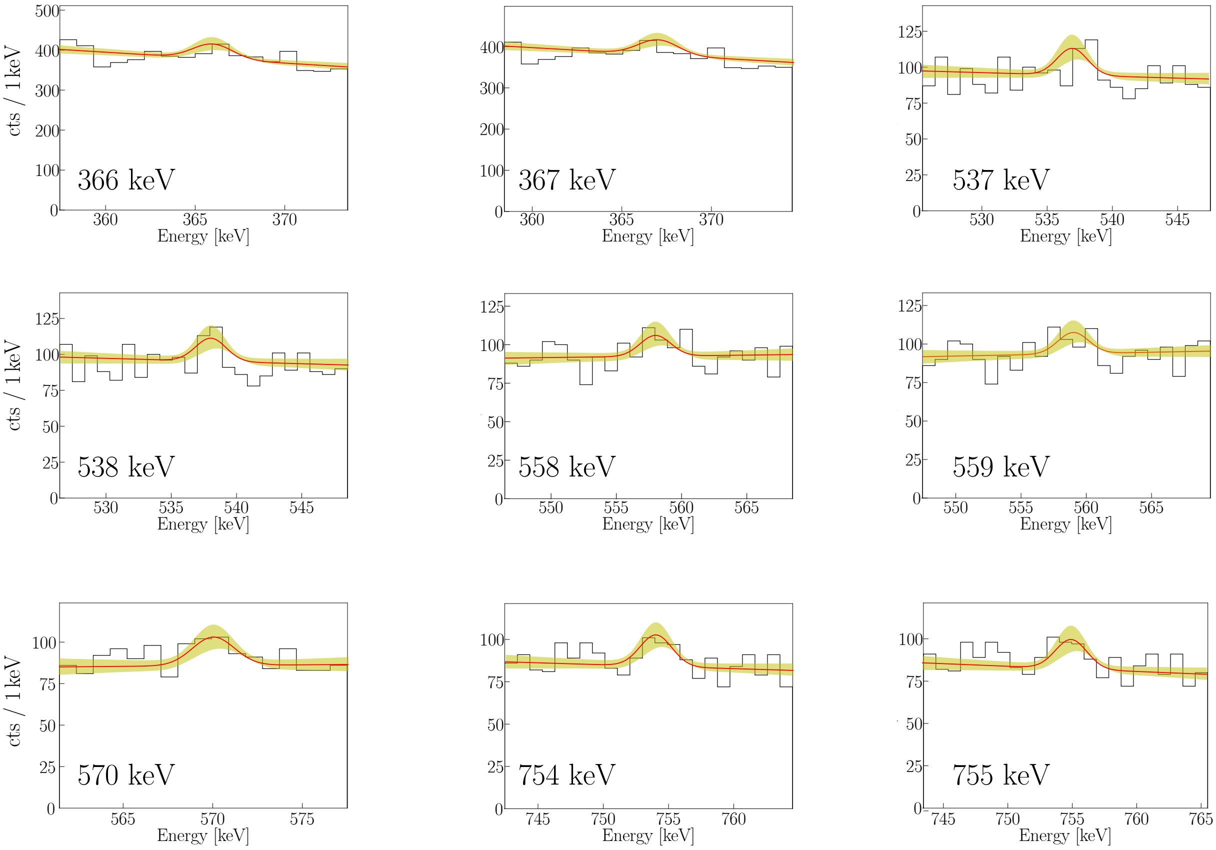

Figure D.2: As for Fig. D.1 for the Coax dataset.

Count rate limit and model expectations in case of no signal around the expected γ lines are shown in Fig. D.3.

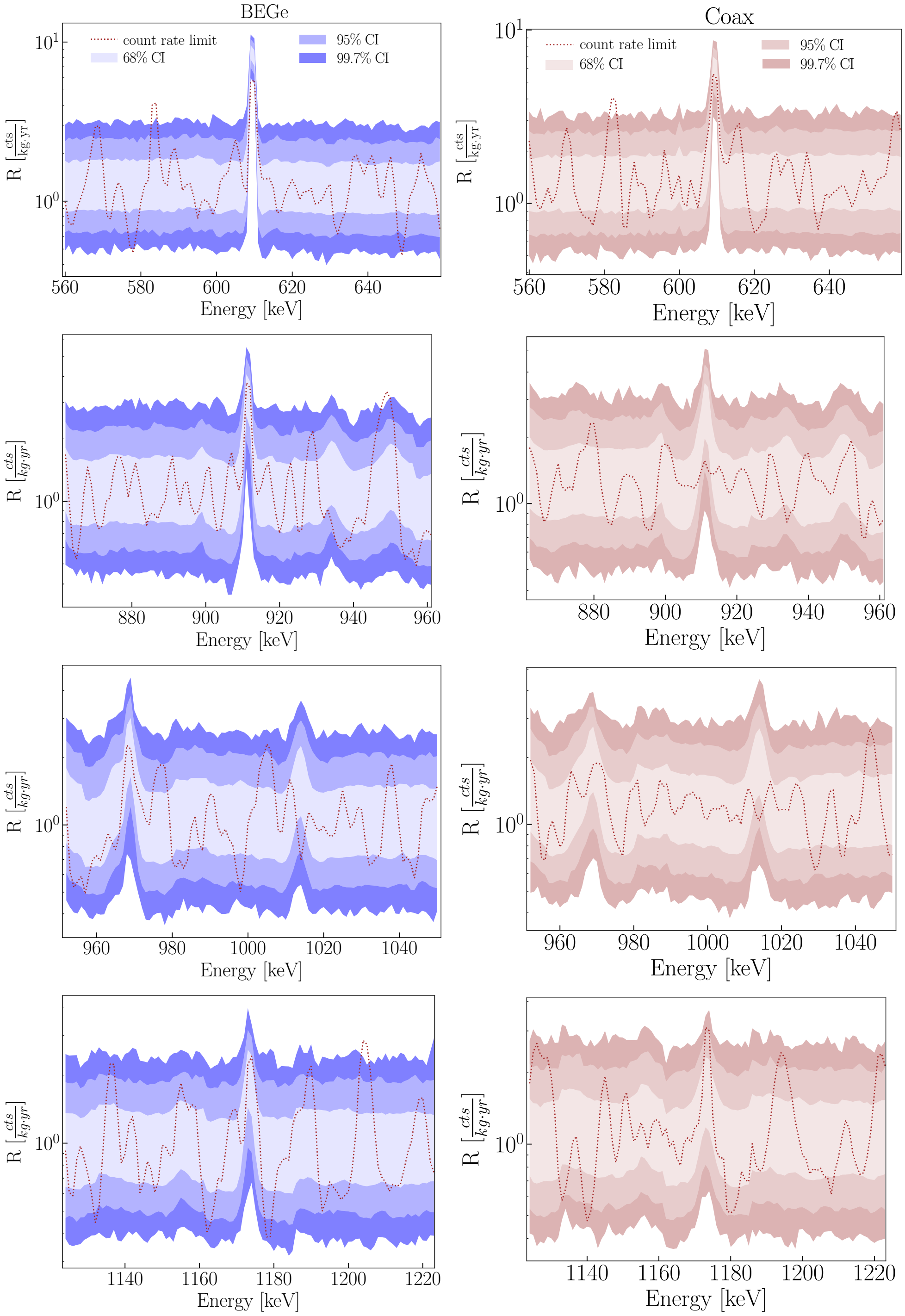

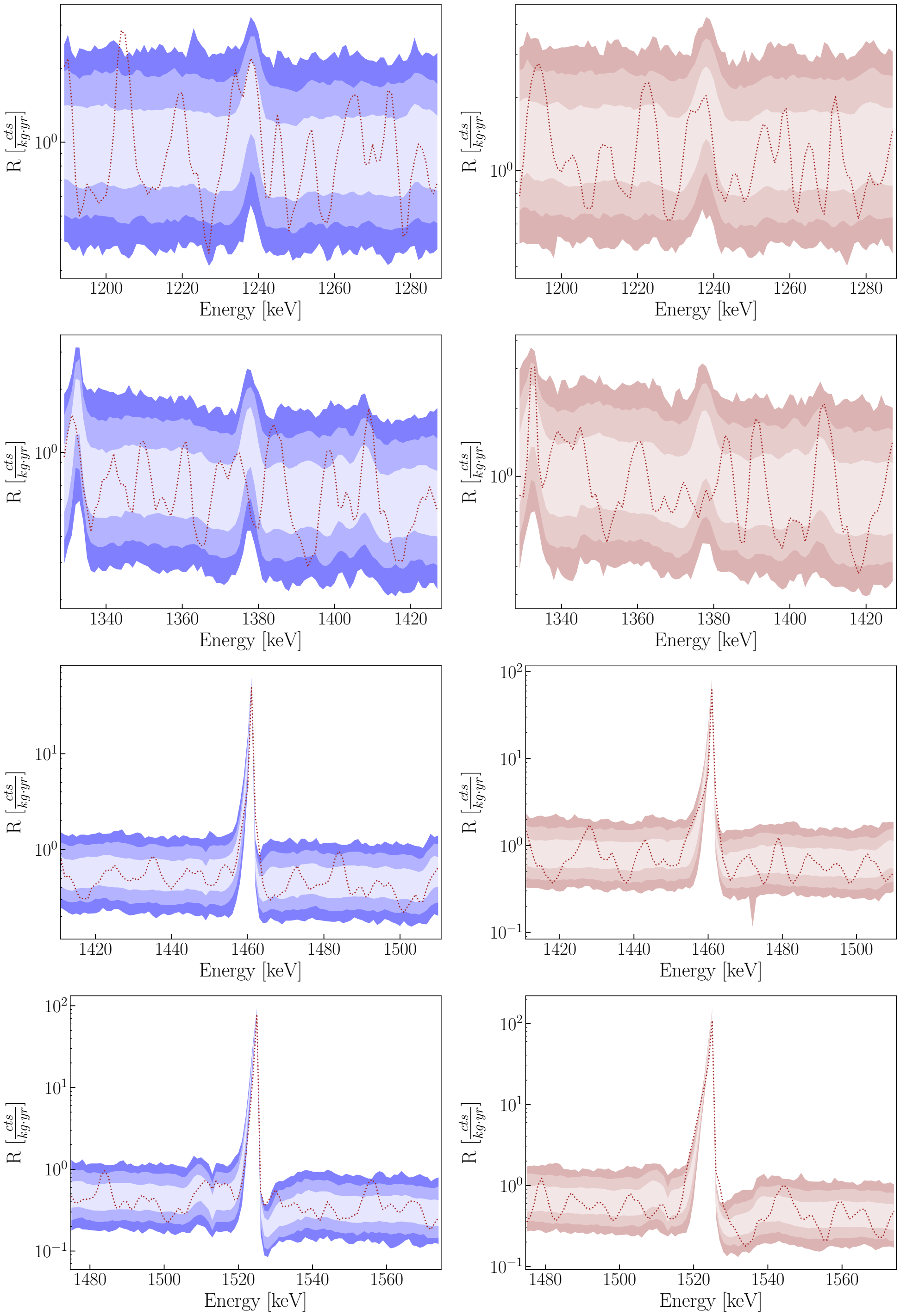
R $\left[\frac{cts}{kg \cdot yr}\right]$
10^0
1200
1220
1240
1260
1280
Energy [keV]
R $\left[\frac{cts}{kg \cdot yr}\right]$
10^0
1200
1220
1240
1260
1280
Energy [keV]
R $\left[\frac{cts}{kg \cdot yr}\right]$
10^0
1340
1360
1380
1400
1420
Energy [keV]
R $\left[\frac{cts}{kg \cdot yr}\right]$
10^0
1340
1360
1380
1400
1420
Energy [keV]
R $\left[\frac{cts}{kg \cdot yr}\right]$
10^1
10^0
1420
1440
1460
1480
1500
Energy [keV]
R $\left[\frac{cts}{kg \cdot yr}\right]$
10^2
10^1
10^0
10^{-1}
1420
1440
1460
1480
1500
Energy [keV]
R $\left[\frac{cts}{kg \cdot yr}\right]$
10^2
10^1
10^0
10^{-1}
1480
1500
1520
1540
1560
Energy [keV]
R $\left[\frac{cts}{kg \cdot yr}\right]$
10^2
10^1
10^0
10^{-1}
1480
1500
1520
1540
1560
Energy [keV]

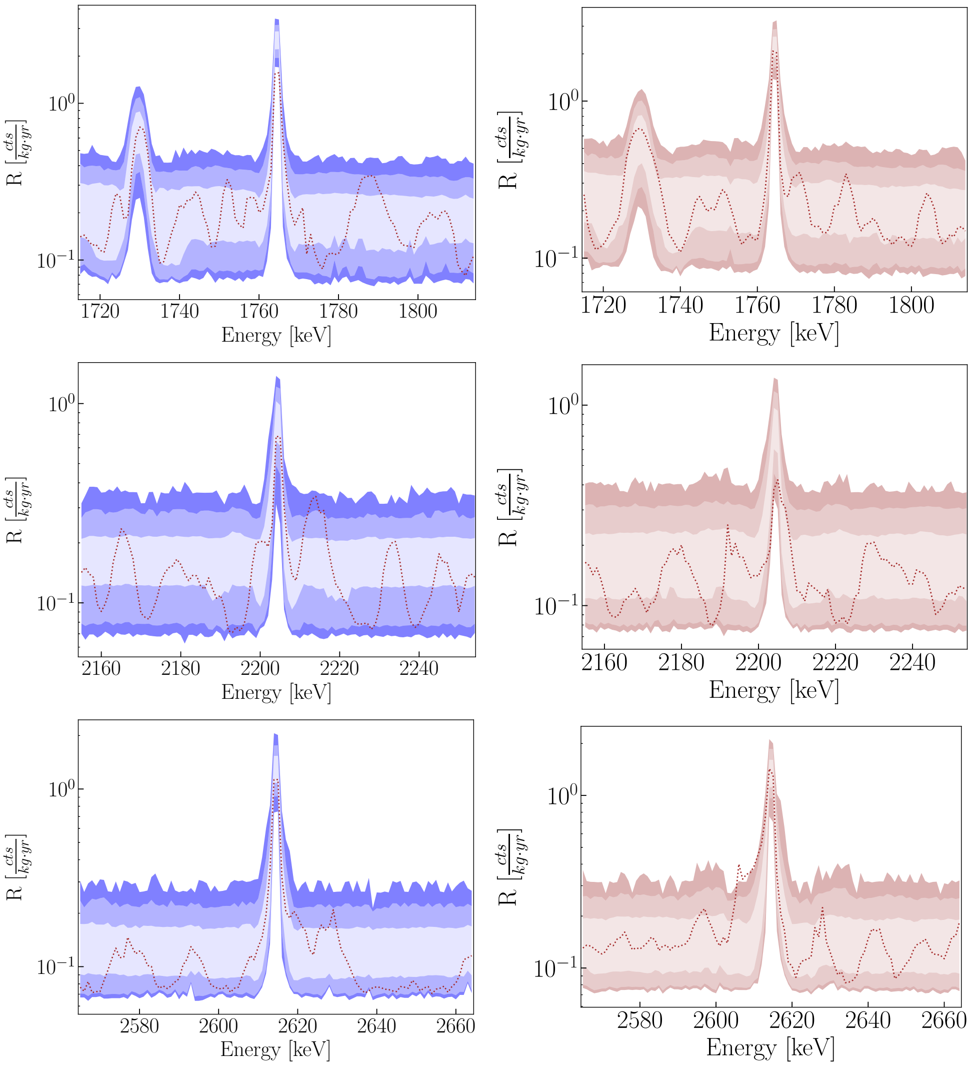

Figure D.3: Median exclusion sensitivity and the count rate of the Gaussian signal around the expected background γ lines.

Appendix E

Limits on the Super-WIMPs Coupling Dataset-wise

Results presented in Fig. 5.12 are obtained from combined count rate from the BEGe and Coax dataset. The limits on the Super-WIMPs estimated individually for each dataset are presented in Fig. E.1 and Fig. E.2.

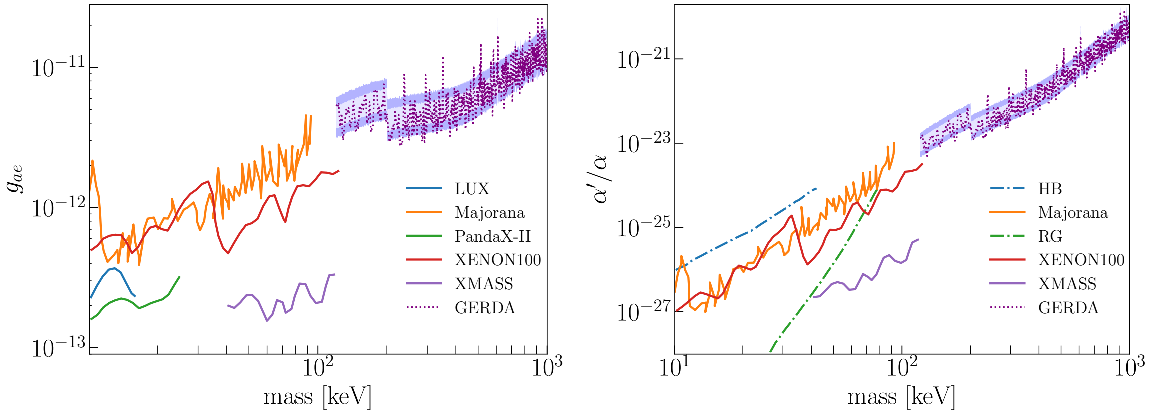

Figure E.1: Comparison of the results on the coupling constants limits between GERDA and various DM experiments for the BEGe dataset.

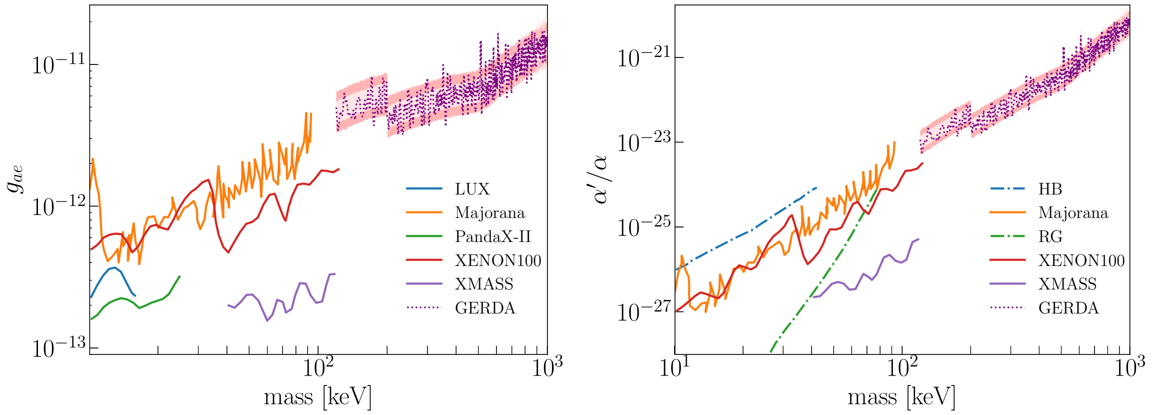

Figure E.2: As for the Fig. E.1 for the Coax dataset.

List of Tables

List of Figures

List of Acronyms

AC	Anti-coincidence
ALP	Axion-like Particle
BAT	Bayesian Anlysis Toolkit
BEGe	Broad Energy Germanium
BI	Background Index
C.I.	Credibility Interval
C.L.	Confidence Level
CMB	Cosmic Microwave Background
CP	Charge, Parity
CPT	Charge, Parity, And Time Reversal Symmetry
DEP	Double Escape Peak
DM	Dark Matter
EC	Electron Capture
FADC	Flash Analog-to-digital Converter
FEP	Full Energy Peak
FWHM	Full Width At Half Maximum
GERDA	Germanium Detector Array
HPGe	High-purity Germanium
HV	High Voltage
IBM-2	Interacting Boson Model
INFN	Istituto Nazionale Di Fisica Nucleare
IO	Inverted Ordering
ISM	Interacting Shell Model
LAr	Liquid Argon
LEGEND	Large Enriched Germanium Experiment For Neutrinoless $\beta\beta$ Decay
LNGS	Laboratori Nazionali Del Gran Sasso
LXe	Liquid Xenon
MC	Monte Carlo
MCMC	Markov Chain Monte Carlo
MSE	Multi-site Events
MWA	Moving Window Average
NME	Nuclear Matrix Element

NO	Normal Ordering
PMNS matrix	Pontecorvo-maki-nakagawa-sakata Matrix
PMT	Photomultiplier
PSD	Pulse Shape Discrimination
PSF	Phase Space Factor
QRPA	Quasiparticle Random Phase Approximation
RMS	Root Mean Square
SEP	Single Escape Peak
SIS	Source Insertion System
SM	Standard Model
SSE	Single-site Event
SiPM	Silicon Photomultiplier
Super-WIMP	Super Weakly Interacting Massive Particle
TPB	Tetraphenyl-butadiene
TPC	Time Projection Chamber
WLS	Wavelength-shifting
ZAC	Zero Area Cusp
pdf	Probability Density Functions
$\|\mathrm{m}_{\beta\beta}\|$	Effective Majorana Mass
$0\nu\beta\beta$	Neutrinoless Double Beta

Bibliography

[1] R. Sime, “Lise Meitner and the discovery of fission,” 1989.

[2] “Pauli’s famous letter.” http://microboone-docdb.fnal.gov/cgi-bin/RetrieveFile?docid=953;filename=pauli

[3] F. Reines and C. L. Cowan, “The neutrino,” *Nature*, vol. 178, pp. 446–449, 1956.

[4] C. L. Cowan, F. Reines, F. B. Harrison, H. W. Kruse, and A. D. McGuire, “Detection of the free neutrino: A Confirmation,” *Science*, vol. 124, pp. 103–104, 1956.

[5] G. Danby, J. M. Gaillard, K. A. Goulianos, L. M. Lederman, N. B. Mistry, M. Schwartz, and J. Steinberger, “Observation of High-Energy Neutrino Reactions and the Existence of Two Kinds of Neutrinos,” *Phys. Rev. Lett.*, vol. 9, pp. 36–44, 1962.

[6] K. Kodama *et al.*, “Final tau-neutrino results from the DONuT experiment,” *Phys. Rev.*, vol. D78, p. 052002, 2008.

[7] U. Dore and L. Zanello, “Bruno Pontecorvo and neutrino physics,” 2009.

[8] B. T. Cleveland, T. Daily, R. Davis, Jr., J. R. Distel, K. Lande, C. K. Lee, P. S. Wildenhain, and J. Ullman, “Measurement of the solar electron neutrino flux with the Homestake chlorine detector,” *Astrophys. J.*, vol. 496, pp. 505–526, 1998.

[9] B. Pontecorvo, “Inverse beta processes and nonconservation of lepton charge,” *Sov. Phys. JETP*, vol. 7, pp. 172–173, 1958. [Zh. Eksp. Teor. Fiz.34,247(1957)].

[10] A. Strumia and F. Vissani, “Neutrino masses and mixings and...,” 2006.

[11] “The nobel prize in physics 2015.,” *NobelPrize.org.*, vol. Nobel Media AB 2019. Sun. 16 Jun 2019.

[12] M. Drewes, “The Phenomenology of Right Handed Neutrinos,” *Int. J. Mod. Phys.*, vol. E22, p. 1330019, 2013.

[13] L. Canetti, M. Drewes, and M. Shaposhnikov, “Matter and Antimatter in the Universe,” *New J. Phys.*, vol. 14, p. 095012, 2012.

[14] M. K. Gaillard, P. D. Grannis, and F. J. Sciulli, “The Standard model of particle physics,” *Rev. Mod. Phys.*, vol. 71, pp. S96–S111, 1999.

[15] M. Tanabashi *et al.*, “Review of Particle Physics,” *Phys. Rev.*, vol. D98, no. 3, p. 030001, 2018.

[16] R. Arnold *et al.*, “Measurement of the double-beta decay half-life and search for the neutrinoless double-beta decay of ^{48}Ca with the NEMO-3 detector,” *Phys. Rev.*, vol. D93, no. 11, p. 112008, 2016.

[17] C. Alduino *et al.*, “Measurement of the two-neutrino double-beta decay half-life of ^{130} Te with the CUORE-0 experiment,” *Eur. Phys. J.*, vol. C77, no. 1, p. 13, 2017.

[18] F. T. Avignone, III, S. R. Elliott, and J. Engel, “Double Beta Decay, Majorana Neutrinos, and Neutrino Mass,” *Rev. Mod. Phys.*, vol. 80, pp. 481–516, 2008.

[19] F. Capozzi, E. Di Valentino, E. Lisi, A. Marrone, A. Melchiorri, and A. Palazzo, “Global constraints on absolute neutrino masses and their ordering,” *Phys. Rev.*, vol. D95, no. 9, p. 096014, 2017.

[20] N. Aghanim *et al.*, “Planck 2018 results. VI. Cosmological parameters,” 2018.

[21] M. Tanabashi *et al.*, “Review of Particle Physics,” *Phys. Rev.*, vol. D98, no. 3, p. 030001, 2018.

[22] B. Aharmim *et al.*, “Electron energy spectra, fluxes, and day-night asymmetries of B-8 solar neutrinos from measurements with NaCl dissolved in the heavy-water detector at the Sudbury Neutrino Observatory,” *Phys. Rev.*, vol. C72, p. 055502, 2005.

[23] S. Abe *et al.*, “Precision Measurement of Neutrino Oscillation Parameters with KamLAND,” *Phys. Rev. Lett.*, vol. 100, p. 221803, 2008.

[24] K. Abe *et al.*, “Measurements of neutrino oscillation in appearance and disappearance channels by the T2K experiment with 6.6×10^{20} protons on target,” *Phys. Rev.*, vol. D91, no. 7, p. 072010, 2015.

[25] M. A. Acero *et al.*, “New constraints on oscillation parameters from ν_e appearance and ν_μ disappearance in the NOvA experiment,” *Phys. Rev.*, vol. D98, p. 032012, 2018.

[26] R. Srivastava, C. A. Ternes, M. Tortola, and J. W. F. Valle, “Testing a lepton quarticity flavor theory of neutrino oscillations with the DUNE experiment,” *Phys. Lett.*, vol. B778, pp. 459–463, 2018.

[27] V. Guiseppe, “New Results from the MAJORANA DEMONSTRATOR Experiment,” June 2018.

[28] O. Azzolini *et al.*, “First Result on the Neutrinoless Double-β Decay of ^{82}Se with CUPID-0,” *Phys. Rev. Lett.*, vol. 120, no. 23, p. 232502, 2018.

[29] C. Alduino *et al.*, “First Results from CUORE: A Search for Lepton Number Violation via $0\nu\beta\beta$ Decay of ^{130}Te,” *Phys. Rev. Lett.*, vol. 120, no. 13, p. 132501, 2018.

[30] J. B. Albert *et al.*, “Search for Neutrinoless Double-Beta Decay with the Upgraded EXO-200 Detector,” *Phys. Rev. Lett.*, vol. 120, no. 7, p. 072701, 2018.

[31] A. Gando *et al.*, “Search for majorana neutrinos near the inverted mass hierarchy region with kamland-zen,” *Phys. Rev. Lett.*, vol. 117, p. 082503, Aug 2016.

[32] M. Agostini *et al.*, “Probing degenerate Majorana neutrino masses,” *Accepted to Science*, 2019.

[33] N. Bohr and J. A. Wheeler, “The Mechanism of Nuclear Fission,” *Phys. Rev.*, vol. 56, pp. 426–450, Sep 1939.

[34] W. Rodejohann, “Neutrino-less Double Beta Decay and Particle Physics,” *Int. J. Mod. Phys.*, vol. E20, pp. 1833–1930, 2011.

[35] M. Doi, T. Kotani, H. Nishiura, K. Okuda, and E. Takasugi, “Neutrino Mass, the Right-handed Interaction and the Double Beta Decay. 1. Formalism,” *Prog. Theor. Phys.*, vol. 66, p. 1739, 1981. [,299(1981)].

[36] J. Kotila and F. Iachello, “Phase space factors for double-β decay,” *Phys. Rev.*, vol. C85, p. 034316, 2012.

[37] H. Primakoff and S. P. Rosen, “Double beta decay,” *Reports on Progress in Physics*, vol. 22, pp. 121–166, jan 1959.

[38] S. Stoica and M. Mirea, “New calculations for phase space factors involved in double-β decay,” *Phys. Rev.*, vol. C88, no. 3, p. 037303, 2013.

[39] D. Stefanik, R. Dvornicky, F. Simkovic, and P. Vogel, “Reexamining the light neutrino exchange mechanism of the $0\nu\beta\beta$ decay with left- and right-handed leptonic and hadronic currents,” *Phys. Rev.*, vol. C92, no. 5, p. 055502, 2015.

[40] J. Menendez, A. Poves, E. Caurier, and F. Nowacki, “Disassembling the Nuclear Matrix Elements of the Neutrinoless beta beta Decay,” *Nucl. Phys.*, vol. A818, pp. 139–151, 2009.

[41] E. Caurier, G. Martinez-Pinedo, F. Nowacki, A. Poves, and A. P. Zuker, “The Shell model as unified view of nuclear structure,” *Rev. Mod. Phys.*, vol. 77, pp. 427–488, 2005.

[42] J. Hyvaerinen and J. Suhonen, “Nuclear matrix elements for $0\nu\beta\beta$ decays with light or heavy Majorana-neutrino exchange,” *Phys. Rev.*, vol. C91, no. 2, p. 024613, 2015.

[43] F. Simkovic, V. Rodin, A. Faessler, and P. Vogel, “$0\nu\beta\beta$ and $2\nu\beta\beta$ nuclear matrix elements, quasiparticle random-phase approximation, and isospin symmetry restoration,” *Phys. Rev.*, vol. C87, no. 4, p. 045501, 2013.

[44] S. Dell'Oro, S. Marcocci, M. Viel, and F. Vissani, "Neutrinoless double beta decay: 2015 review," *Adv. High Energy Phys.*, vol. 2016, p. 2162659, 2016.

[45] J. Engel and J. Menendez, "Status and Future of Nuclear Matrix Elements for Neutrinoless Double-Beta Decay: A Review," *Rept. Prog. Phys.*, vol. 80, no. 4, p. 046301, 2017.

[46] F. Simkovic, V. Rodin, A. Faessler, and P. Vogel, "$0\nu\beta\beta$ and $2\nu\beta\beta$ nuclear matrix elements, quasiparticle random-phase approximation, and isospin symmetry restoration," *Phys. Rev.*, vol. C87, no. 4, p. 045501, 2013.

[47] O. Cremonesi and M. Pavan, "Challenges in Double Beta Decay," *Adv. High Energy Phys.*, vol. 2014, p. 951432, 2014.

[48] S. R. Elliott and P. Vogel, "Double beta decay," *Ann. Rev. Nucl. Part. Sci.*, vol. 52, pp. 115–151, 2002.

[49] A. J. Zsigmond, "New results from GERDA Phase II," June 2018.

[50] J. Argyriades *et al.*, "Measurement of the two neutrino double beta decay half-life of Zr-96 with the NEMO-3 detector," *Nucl. Phys.*, vol. A847, pp. 168–179, 2010.

[51] R. Arnold *et al.*, "Limits on different Majoron decay modes of Mo-100 and Se-82 for neutrinoless double beta decays in the NEMO-3 experiment," *Nucl. Phys.*, vol. A765, pp. 483–494, 2006.

[52] J. Argyriades *et al.*, "Measurement of the Double Beta Decay Half-life of Nd-150 and Search for Neutrinoless Decay Modes with the NEMO-3 Detector," *Phys. Rev.*, vol. C80, p. 032501, 2009.

[53] K. Lou *et al.*, "Recent results of the Gotthard TPC experiment," in *Weak and electromagnetic interactions in nuclei. Proceedings, 44th Yamada Conference, 4th International Symposium, WEIN-95, Osaka, Japan, June 12-16, 1995*, pp. 192–203, 1995.

[54] H. V. Klapdor-Kleingrothaus *et al.*, "Latest results from the Heidelberg-Moscow double beta decay experiment," *Eur. Phys. J.*, vol. A12, pp. 147–154, 2001.

[55] C. E. Aalseth *et al.*, "The IGEX Ge-76 neutrinoless double beta decay experiment: Prospects for next generation experiments," *Phys. Rev.*, vol. D65, p. 092007, 2002.

[56] G. Habbottle, "The half-lives of two long-lived nuclear isomers, 108mag and 192m2ir, and of 137cs and 204tl,"

[57] V. E. Guiseppe *et al.*, "The Status and Initial Results of the MAJORANA DEMONSTRATOR Experiment," *AIP Conf. Proc.*, vol. 1894, no. 1, p. 020010, 2017.

[58] J. B. Albert *et al.*, "Sensitivity and Discovery Potential of nEXO to Neutrinoless Double Beta Decay," *Phys. Rev.*, vol. C97, no. 6, p. 065503, 2018.

[59] S. A. Kharusi *et al.*, "nEXO Pre-Conceptual Design Report," 2018.

[60] J. Aalbers *et al.*, “DARWIN: towards the ultimate dark matter detector,” *JCAP*, vol. 1611, p. 017, 2016.

[61] N. Abgrall *et al.*, “The Large Enriched Germanium Experiment for Neutrinoless Double Beta Decay (LEGEND),” *AIP Conf. Proc.*, vol. 1894, no. 1, p. 020027, 2017.

[62] T. Comellato, “Performance of custom designed inverted coaxial HPGe detectors for Gerda and Legend,” *Nucl. Instrum. Meth.*, vol. A936, pp. 247–248, 2019.

[63] M. Agostini *et al.*, “Upgrade for Phase II of the Gerda experiment,” *Eur. Phys. J.*, vol. C78, no. 5, p. 388, 2018.

[64] “LNGS.” https://www.lngs.infn.it/en/lngs-overview.

[65] M. Agostini *et al.*, “Background-free search for neutrinoless double-β decay of ^{76}Ge with GERDA,” 2017. [Nature544,47(2017)].

[66] K. H. Ackermann *et al.*, “The GERDA experiment for the search of $0\nu\beta\beta$ decay in ^{76}Ge,” *Eur. Phys. J.*, vol. C73, no. 3, p. 2330, 2013.

[67] G. Gilmore, “Practical gamma-ray spectrometry: Second edition,” *ISBN 978-0-470-86196-7. Published by Wiley-VCH Verlag, Wenheim, Germany, 2008.*, 04 2008.

[68] H. R. Bilger, “Fano Factor in Germanium at 77 K,” *Physical Review - PHYS REV X*, vol. 163, pp. 238–253, 11 1967.

[69] N. Strokan, V. Ajdacic, and B. Lalovic, “Measurements of the fano factor in germanium,” *Nuclear Instruments and Methods*, vol. 94, pp. 147–149, 06 1971.

[70] M. Agostini *et al.*, “Characterization of 30 ^{76}Ge enriched Broad Energy Ge detectors for GERDA Phase II,” 2019.

[71] D. Gonzalez *et al.*, “Pulse shape discrimination in the IGEX experiment,” *Nucl. Instrum. Meth.*, vol. A515, pp. 634–643, 2003.

[72] M. Agostini *et al.*, “Production, characterization and operation of ^{76}Ge enriched BEGe detectors in GERDA,” *Eur. Phys. J.*, vol. C75, no. 2, p. 39, 2015.

[73] M. Agostini *et al.*, “Pulse shape discrimination for GERDA Phase I data,” *Eur. Phys. J.*, vol. C73, no. 10, p. 2583, 2013.

[74] S. Ramo, “Currents induced by electron motion,” *Proc. Ire.*, vol. 27, pp. 584–585, 1939.

[75] W. Shockley, “Currents to conductors induced by a moving point charge,” *J. Appl. Phys.*, vol. 9, p. 635, 1938.

[76] M. Agostini, C. A. Ur, D. Budjas, E. Bellotti, R. Brugnera, C. M. Cattadori, A. di Vacri, A. Garfagnini, L. Pandola, and S. Schonert, “Signal modeling of high-purity Ge detectors with a small read-out electrode and application to neutrinoless double beta decay search in Ge-76,” *JINST*, vol. 6, p. P03005, 2011.

[77] G. Benato. PhD thesis.

[78] M. Agostini *et al.*, “Improvement of the energy resolution via an optimized digital signal processing in GERDA Phase I,” *Eur. Phys. J.*, vol. C75, no. 6, p. 255, 2015.

[79] M. Agostini *et al.*, “Results on $\beta\beta$ decay with emission of two neutrinos or Majorons in ^{76} Ge from GERDA Phase I,” *Eur. Phys. J.*, vol. C75, no. 9, p. 416, 2015.

[80] C. Macolino, “Results on neutrinoless double beta decay from GERDA Phase I,” *Mod. Phys. Lett.*, vol. A29, no. 1, p. 1430001, 2014.

[81] L. Baudis, A. D. Ferella, F. Froborg, and M. Tarka, “Monte Carlo studies and optimization for the calibration system of the GERDA experiment,” *Nucl. Instrum. Meth.*, vol. A729, pp. 557–564, 2013.

[82] L. Baudis, G. Benato, P. Carconi, C. M. Cattadori, P. De Felice, K. Eberhardt, R. Eichler, A. Petrucci, M. Tarka, and M. Walter, “Production and characterization of ^{228}Th calibration sources with low neutron emission for GERDA,” *JINST*, vol. 10, no. 12, p. P12005, 2015.

[83] “Gamma rays energy values.” http://www.radiochemistry.org/periodictable.

[84] root.cern.ch.

[85] https://root.cern.ch/doc/v614/classTSpectrum.html.

[86] https://root.cern.ch/doc/v608/Minuit2Page.html.

[87] M. Agostini *et al.*, “Improved Limit on Neutrinoless Double-β Decay of ^{76}Ge from GERDA Phase II,” *Phys. Rev. Lett.*, vol. 120, no. 13, p. 132503, 2018.

[88] M. Agostini *et al.*, “The background in the $0\nu\beta\beta$ experiment GERDA,” *Eur. Phys. J.*, vol. C74, no. 4, p. 2764, 2014.

[89] A. Caldwell, D. Kollar, and K. Kroninger, “BAT: The Bayesian Analysis Toolkit,” *Comput. Phys. Commun.*, vol. 180, pp. 2197–2209, 2009.

[90] J. S. O’Connell and F. J. Schima, “Muon Induced Radioactivity in Underground Detectors,” *Phys. Rev.*, vol. D38, pp. 2277–2279, 1988.

[91] M. Agostini *et al.*, “Measurement of the half-life of the two-neutrino double beta decay of Ge-76 with the Gerda experiment,” *J. Phys.*, vol. G40, p. 035110, 2013.

[92] W. Gilks, S. Richardson, and D. Spiegelhalter, “Markov chain Monte Carlo in practice,” 1995.

[93] V. D’Andrea. PhD thesis.

[94] R. C. A.J. Peurung, T.W. Bowyer and P. Reeder *Nucl. Instrum. Meth.*, vol. A 396, p. 425, 1997.

[95] A. Lubashevskiy *et al.*, “Mitigation of^{42}Ar/^{42}K background for the GERDA Phase II experiment,” *Eur. Phys. J.*, vol. C78, no. 1, p. 15, 2018.

[96] P. Benetti *et al.*, “Measurement of the specific activity of ar-39 in natural argon,” *Nucl. Instrum. Meth.*, vol. A574, pp. 83–88, 2007.

[97] R.Hiller *Presentation on the GERDA Collaboration Meeting*, June 2017.

[98] D. Casadei, “Reference analysis of the signal + background model in counting experiments,” *JINST*, vol. 7, p. P01012, 2012.

[99] F. Beaujean, A. Caldwell, D. Kollar, K. Kroeninger, and S. Pashapour, “Signal discovery in sparse spectra: a Bayesian analysis,” in *Proceedings, PHYSTAT 2011 Workshop on Statistical Issues Related to Discovery Claims in Search Experiments and Unfolding, CERN,Geneva, Switzerland 17-20 January 2011*, (Geneva), pp. 138–142, CERN, CERN, 2011.

[100] M. Pospelov, A. Ritz, and M. B. Voloshin, “Bosonic super-WIMPs as keV-scale dark matter,” *Phys. Rev.*, vol. D78, p. 115012, 2008.

[101] G. Steigman and M. S. Turner, “Cosmological Constraints on the Properties of Weakly Interacting Massive Particles,” *Nucl. Phys.*, vol. B253, pp. 375–386, 1985.

[102] G. Jungman, M. Kamionkowski, and K. Griest, “Supersymmetric dark matter,” *Phys. Rept.*, vol. 267, pp. 195–373, 1996.

[103] R. D. Peccei and H. R. Quinn, “CP Conservation in the Presence of Instantons,” *Phys. Rev. Lett.*, vol. 38, pp. 1440–1443, 1977. [,328(1977)].

[104] S. Weinberg, “A New Light Boson?,” *Phys. Rev. Lett.*, vol. 40, pp. 223–226, 1978.

[105] N. Blinov, M. J. Dolan, P. Draper, and J. Kozaczuk, “Dark Matter Targets for Axion-like Particle Searches,” 2019.

[106] A. Einstein, “Concerning an heuristic point of view toward the emission and transformation of light,” *Annalen Phys.*, vol. 17, pp. 132–148, 1905.

[107] R. Foot and S. Vagnozzi, “Dissipative hidden sector dark matter,” *Phys. Rev.*, vol. D91, p. 023512, 2015.

[108] T. G. Rizzo, “Kinetic Mixing and Portal Matter Phenomenology,” *Phys. Rev.*, vol. D99, no. 11, p. 115024, 2019.

[109] K. Abe *et al.*, “Search for dark matter in the form of hidden photons and axion-like particles in the XMASS detector,” *Phys. Lett.*, vol. B787, pp. 153–158, 2018.

[110] C. Fu *et al.*, “Limits on Axion Couplings from the First 80 Days of Data of the PandaX-II Experiment,” *Phys. Rev. Lett.*, vol. 119, no. 18, p. 181806, 2017.

[111] D. S. Akerib *et al.*, “First Searches for Axions and Axionlike Particles with the LUX Experiment,” *Phys. Rev. Lett.*, vol. 118, no. 26, p. 261301, 2017.

[112] E. Aprile *et al.*, “Search for Bosonic Super-WIMP Interactions with the XENON100 Experiment,” *Phys. Rev.*, vol. D96, no. 12, p. 122002, 2017.

[113] N. Abgrall *et al.*, “New limits on Bosonic Dark Matter, Solar Axions, Pauli Exclusion Principle Violation, and Electron Decay from the Majorana Demonstrator,” *Phys. Rev. Lett.*, vol. 118, no. 16, p. 161801, 2017.

[114] *GSTR-16-002*.

[115] *GSTR-18-011*.

[116] M. Boswell *et al.*, “MaGe-a Geant4-based Monte Carlo Application Framework for Low-background Germanium Experiments,” *IEEE Trans. Nucl. Sci.*, vol. 58, pp. 1212–1220, 2011.

[117] “Geant4.” https://geant4.web.cern.ch/.

Acknowledgements

First of all, I would like to thank my supervisor, Prof. Laura Baudis, for giving me an excellent opportunity to do research in her group and to participate in the exciting phase of the Gerda experiment. Thanks to the professional and personal support of Laura Baudis, it became possible to complete this Ph.D. thesis.

I want to thank Roman Hiller for the productive collaborative work all these years, for always critical view and constructive suggestions. A special acknowledgment for the helpful discussions regarding the statistical issues we have accounted along the Super-WIMPs analysis.

I thank Giovanni Benato for the introduction to the calibration analysis, for valuable suggestions in the first year of Ph.D. in the moments of difficulties. Furthermore, I would like to thank Luciano Pandola and Matteo Agostini for guidance in the calibration analysis along the way, and especially in preparation for the first unblinding. I thank all members of the Gerda collaboration for the fruitful discussions during the meetings and fun during the social dinners.

Special acknowledgment to everyone who helped to complete this thesis. I am grateful to Laura for reading the entire dissertation and valuable comments. Additionally, I want to thank Roman, Michelle, Chloe, and Patricia for giving constructive suggestions on how to improve the content and English writing.

During these years, the work environment played an essential role in Ph.D. life. I want to thank my officemates and the entire group of Laura for professional discussions and for the ever-dynamic environment. Special thanks to Chloe, Michelle, and all girls for being cool friends along the way.

I thank all my friends for the joyful time and support. I thank Paule Dagenais for our chats and great time outside of the university, Alessandro Minotti for the cheerful words and fun time, Matthia for bringing an easy-going attitude to life. I want to thank Alena, Marishka, and Anastasia for staying friends despite the time and distance. Special thanks to Michi for teaching me programming from scratch, for the philosophical and physics discussions, and the great years of the friendship.

I want to thank Ramun for proofreading my thesis and for your always into the point suggestions. Thanks to your encouragement, the hard time writing the Ph.D. thesis became less stressed and happier.

Especially, I thank my mother for endless wisdom, for teaching how to set goals and work hard to achieve those. I thank my sister for the empathy and strength you share with me. Thank you for your endless inspiration and support.